UNIVERSITÉ CATHOLIQUE DE LOUVAIN
FACULTÉ DES SCIENCES, ECOLE DE PHYSIQUE
EARTH AND LIFE INSTITUTE
GEORGES LEMAÎTRE CENTRE FOR EARTH AND CLIMATE RESEARCH

REPRESENTATION OF SUBGRID-SCALE SEA ICE-OCEAN INTERACTIONS IN LARGE-SCALE MODELS

DOCTORAL DISSERTATION PRESENTED BY

ANTOINE BARTHÉLEMY

IN PARTIAL FULFILLMENT OF THE
REQUIREMENTS FOR THE DEGREE OF
DOCTOR IN SCIENCES

THESIS COMMITTEE:

Prof. Thierry Fichefet (Supervisor)	Université catholique de Louvain
Prof. Hugues Goosse (Supervisor)	Université catholique de Louvain
Prof. Marie-Laurence De Keersmaecker (Chair)	Université catholique de Louvain
Prof. Eric Deleersnijder	Université catholique de Louvain
Prof. Gurvan Madec	Institut Pierre-Simon Laplace, Paris
Dr. Martin Vancoppenolle	Institut Pierre-Simon Laplace, Paris
Dr. Julien Le Sommer	Laboratoire de Glaciologie et Géophysique de l'Environnement, Grenoble

LOUVAIN-LA-NEUVE
JANUARY 2016

Le Fonds de la Recherche Scientifique (F.R.S.-FNRS) a financé pendant quatre ans ce projet de recherche. Sans financement, pas de thèse. Et sans thèse, pas de remerciements. Dès lors, pour commencer, merci à eux de m'avoir accordé deux mandats d'aspirant. Le projet européen EMBRACE est également remercié pour son support.

Mes prochains mots vont à mes deux promoteurs, les Professeurs Thierry Fichefet et Hugues Goosse. Merci de m'avoir fait confiance, de m'avoir proposé ce projet et de m'avoir donné les moyens de le mener à bien. Thierry, j'ai beaucoup apprécié travailler sous ta guidance. Merci pour tes remarques avisées, ton souci du détail et ton pragmatisme. Hugues, merci pour la richesse de tes idées, pour ta capacité à toujours voir les résultats sous leur meilleur jour et pour ta bonne humeur. Je vous remercie sincèrement, tous les deux, pour votre infaillible disponibilité et pour l'incomparable ambiance que vous faites régner dans vos équipes. J'ai hâte de continuer à travailler avec vous.

Ce projet a été l'occasion de rencontrer d'autres excellents scientifiques, auprès desquels j'ai énormément appris. Un très grand merci à Gurvan pour le temps que tu m'as consacré, à Paris et lors de ta longue visite à Louvain-la-Neuve. Pouvoir bénéficier de ta connaissance encyclopédique du code a été une aide précieuse pour mes développements. Merci à Martin pour les discussions, toujours intéressantes, que nous avons eues sur la glace de mer et sur le modèle. Merci enfin à Clément pour son travail de fond sur le code.

Je remercie également les autres membres du jury, Eric Deleersnijder et Julien Le Sommer, pour l'intérêt qu'ils ont porté à ma thèse et pour leurs commentaires positifs et constructifs sur le manuscrit. Merci à Marie-Laurence De Keersmaecker d'avoir accepté de présider ce jury.

Je suis extrêmement reconnaissant à l'International Arctic Research Center de l'University of Alaska Fairbanks d'avoir organisé, grâce au financement de la National Science Foundation, l'école d'été à laquelle j'ai participé en septembre 2013. Tenue à bord d'une croisière scientifique dans l'Océan Arctique, cette école m'a permis de toucher du doigt (littéralement) mon sujet de recherche. Elle a été d'une utilité indéniable dans ma formation.

Merci au Centre de Calcul Intensif et de Stockage de Masse (CISM) de l'UCL, pour avoir fourni les ressources informatiques et le support nécessaires à la bonne réalisation des études constituant ce travail.

Je n'oublierai pas de remercier mes collègues. C'est un peu grâce à chacun d'entre vous que règne une si excellente atmosphère à l'intérieur (et à l'extérieur) de ce labo. Et cela compte, quand on décompte les mois avant les échéances fatidiques. Merci aux anciens, qui ont montré la voie : Olivier, François M., Alice, Violette, Aurélien, Elisabeth, Pierre et Svetlana. À Pierre-Yves aussi, notamment pour l'indispensable support technique. Aux autres enfin, à qui je souhaite beaucoup de courage pour en terminer : Isaline, François K., Jérôme, Sylvain T., Jonathan, Mathilde, François C., Sylvain M., Celia, et peut-être même Chloé. (Loin de moi l'idée de vouloir vous mettre la pression, mais l'ordre de cette liste n'a peut-être pas été choisi au hasard. :-p) Merci encore à Dominique et à Monique pour leur travail discret mais toujours efficace.

Hors du labo, je veux surtout remercier Nicolas et Xavier, entre autres d'avoir été là cette année quand j'en avais besoin. Alizée, tu mérites évidemment une mention particulière. Je te remercie chaleureusement pour ton soutien pendant les premières années de ce projet. Et puis, bien que ce fut par la force des événements, merci de m'avoir permis de réaliser que je pouvais aussi m'en sortir seul, en fait.

Finalement, un merci tout particulier à mes parents, pour les valeurs de travail et d'effort que vous m'avez inculquées, et pour m'avoir mis dans les conditions idéales pour arriver jusqu'ici. Si je parviens un jour à amener mes enfants à moitié aussi loin que là où vous nous avez amenés, Claire et moi, je pourrai m'estimer heureux. À Claire, je dirai simplement : hun. Et elle comprendra.

En septembre 2011, je croyais qu'il me suffirait *juste* de travailler pendant quatre ans pour obtenir le titre de docteur. Je n'aurais pas pu me tromper plus lourdement. Préparer une thèse de doctorat est un effort de longue haleine, et

un projet dans lequel on se plonge entièrement. Les obstacles sont nombreux, et les plus sérieux peuvent vite se transformer en moments de doute, voire de panique. Que toutes les personnes mentionnées ci-dessus soient encore une fois remerciées. C'est en partie grâce à elles que j'en suis ici, à rédiger la dernière ligne de mes remerciements.

CONTENTS

Contents **v**

1 Introduction **1**
1.1 Sea ice in the polar oceans 2
1.2 Ocean and sea ice modeling 8
1.3 Objectives of the thesis 12

2 Brine rejection parameterizations **19**
2.1 Introduction 21
2.2 Brine rejection parameterization in NEMO-LIM3 22
2.3 Observational data 26
2.4 Results and discussion 29
2.5 Conclusions 48

3 Ocean surface boundary conditions under sea ice **51**
3.1 Introduction 53
3.2 Model setup 55
3.3 Results: sea ice 60
3.4 Results: ocean surface boundary conditions 68
3.5 Conclusions 80

4 Multi-column ocean **83**
4.1 Introduction 85
4.2 Model description 87
4.3 Multi-column ocean scheme 88
4.4 Results and discussion 94
4.5 Conclusions 116

5 Conclusions **119**
5.1 Contributions of the thesis 119
5.2 Limitations and perspectives 125

A Acronyms **129**

B Publications and communications **131**

References **133**

CHAPTER 1

INTRODUCTION

Besides being of primary importance in the Earth's climate system, the recent sea ice changes in polar oceans raise significant ecological, geopolitical and economic issues. A number of dramatic events occurred during the last four years, as the present work was being pursued. By mid-September 2012, the Arctic sea ice extent retreated to 3.4 million km^2, far below the previous extreme minimum recorded in summer 2007. While it partly recovered in 2013 and 2014, the summer melt was again intense in 2015, ultimately leading to the fourth lowest minimum in the satellite observation era, at 4.4 million km^2 on September 11. On the other side of the planet, Antarctic sea ice behaved quite differently. After three years of successive record-setting extent maxima peaking at 20.2 million km^2 in September 2014, the Antarctic sea ice still tracked at record high daily levels for several weeks in early winter 2015. Its seasonal expansion then abruptly slowed down and this year's maximum was only slightly above the climatological average.

This large year-to-year variability, the uncertainties in the future rate of Arctic sea ice loss, the yet incompletely explained positive trend in Antarctic sea ice in a global warming context and the equally important but less visible changes in the underlying oceans need to be further investigated and better understood in order to inform policymakers and stakeholders. Numerical models provide a useful tool to achieve this goal. Sea ice modules have been

incorporated in ocean models for decades, reaching a high level of complexity and a reasonable agreement with available observations, but improvements remain necessary in a number of aspects.

The primary focus of this thesis is the **representation of heterogeneous sea ice-ocean interactions in large-scale models**. Although the subgrid-scale variability in ice properties has long been included in models, its influence on the ocean underneath has been so far overlooked. In this modeling study, our objectives are to improve our understanding of the physics of the problem, to investigate how small-scale ice-ocean processes can be represented and to quantify their impact on the large-scale simulated oceanography of polar regions. In this first chapter, we describe the subtle interplay between sea ice and ocean, present a quick overview of the current state of sea ice modeling and list the scientific questions that we aim answering in the present work.

1.1 Sea ice in the polar oceans

Sea ice refers to any form of ice found at sea which has originated from the freezing of seawater (WMO, 1970). Nowadays, the global sea ice coverage varies seasonally between 17 and 27 million km^2 (Parkinson, 2014a), corresponding to 3.3 and 5.3 % of the Earth's surface. In winter, the Antarctic sea ice is typically 1 m thick on average, with regional maxima above 2 m (Worby et al., 2008). The mean thickness in the Arctic is larger and locally exceeds 5 m (e.g., Lindsay and Schweiger, 2015).

1.1.1 A complex interface between atmosphere and ocean

At the hemispheric scale, sea ice is often described by a unique number, its extent, which is defined as the total area of regions covered with at least 15 % ice. This suggests the simplistic and erroneous view that ice forms a continuous, uniform blanket at the surface of polar oceans. In reality, deformation processes make the sea ice an extremely complex and heterogeneous medium (Fig. 1.1, Thorndike et al., 1975). In all seasons, divergence or shear motions fracture the ice pack and create leads, i.e. linear openings ranging from several to hundreds of kilometers in length and from a few meters to a few kilometers in width. Strong winds in coastal regions or high oceanic heat fluxes generate wider and more persistent open water areas known as polynyas, with sizes between a few and tens of kilometers. In winter, below freezing air temperatures limit the expanse of open waters, but the latter can occupy a large fraction of the surface during the melting season. Besides, undeformed ice can be as thin as a few centimeters when it has just formed in leads or open waters, and two to three meters thick when it has survived several years. Pressure ridges re-



Figure 1.1: Heterogeneous sea ice cover in the Arctic Ocean (near 80° N, 145° E), on September 2 during the 2013 NABOS cruise (Nansen and Amundsen Basins Observational System). A thick pressure ridge is visible in the foreground, surrounded by thinner undeformed ice and patches of open water. This picture was taken at the transition between the melting and the freezing seasons.

sulting from convergent motions have thicknesses sometimes exceeding 10 m, while they are only a few meters wide.

Ice at the sea surface impacts drastically the interactions between the atmosphere and the ocean. The albedo of sea ice depends on the state of its surface and on the presence of snow or melt ponds (e.g., Perovich and Polashenski, 2012). It is always higher than the water albedo, implying that the absorption of solar radiation is strongly reduced in ice-covered regions. The low thermal conductivity of ice (e.g., Pringle et al., 2007) diminishes the winter heat transfers from the ocean to the atmosphere, an effect that is even larger when the ice is overlaid with insulating snow. In addition, the phase change corresponding to sea ice growth imposes that the water temperature cannot decrease below a minimum equal to the local freezing point. The seawater density in polar regions is therefore highly influenced by its salinity, which has a clear impact on the properties of the deep water bodies that are formed there and that occupy the vast majority of oceanic basins worldwide. Since most of the salt contained in seawater is rejected when it freezes, and because ice is transported by winds and currents, sea ice formation and melt also induce salt and freshwater fluxes that modify the stability of the water column (e.g., Winton, 1999). Moreover, the accumulation of snow on top of sea ice delays the freshening effect of precipitation until snow melts, and evapora-

tion is suppressed when ice is present. In summer, ice again maintains the sea surface temperature close to the freezing point. Finally, the presence of a consolidated sea ice pack alters the input of mechanical energy from the wind, by preventing the formation of waves (e.g., Thomson and Rogers, 2014) and by imposing a surface stress caused by the relative ice-ocean motion. Sea ice plays a major role in global biogeochemical cycles as well, but these aspects are beyond the scope of the present work and the interested reader is referred to the review by Vancoppenolle et al. (2013).

1.1.2 A subtle interplay with the underlying ocean

By modulating the heat and salt budgets and the mechanical energy input at the ocean surface, sea ice strongly influences vertical mixing in the water column. Brine rejections caused by intense ice formation on the continental shelves around Antarctica have particularly far-reaching effects on the World Ocean circulation. The associated convective mixing induces the development of very thick winter mixed layers (e.g., Arthun et al., 2013; Petty et al., 2014) and leads to the formation of deep, salty water masses that take an active part in the global thermohaline circulation (e.g., Stössel et al., 2002). Conversely, the melt of ice with low salinity stabilizes the water column, reduces mixed layer depths and ultimately dampens the exchanges between the atmosphere and the deep ocean (e.g., Goosse and Fichefet, 1999).

At local scales, under-ice vertical mixing directly determines the rate of heat transfer from the ocean interior to the surface, hence impacting the energy balance of the ice itself. In summertime in both hemispheres, most of the oceanic heat is provided by shortwave radiation entering the ocean through open water and thin ice (e.g., Maykut and Perovich, 1987; Maykut and McPhee, 1995; Ohshima and Nihashi, 2005). Between 70 and 90 % of the absorbed solar energy is used to melt sea ice (Steele, 1992; Ohshima and Nihashi, 2005), while the rest warms the surface waters, which potentially delays the autumn freeze-up or reduces the next winter ice thickness (e.g., Hudson et al., 2013; Timmermans, 2015). In the Canada Basin of the Arctic Ocean, Ekman convergence forces a downwelling circulation that pushes the summer warm layer downward. Heat is therefore stored in a near-surface temperature maximum under the mixed layer. It can be released during shear-driven or convective mixing events induced by storms or by strong brine rejections due to sea ice growth (Steele et al., 2011; Jackson et al., 2012; Zhang et al., 2013; Timmermans, 2015).

The vertical transfer of heat from deeper oceanic layers shows clear hemispheric contrasts. In the Arctic Ocean, the intermediate depth range ($\sim$ 150-900 m) is occupied by warm and salty waters of Atlantic origin, which contain

enough energy to melt several times the entire Arctic sea ice cover, if it could be brought to the surface (e.g., Polyakov et al., 2011). The intrusion of Summer Pacific Water constitutes another source of heat at depth (e.g., Bourgain and Gascard, 2012). The existence of a strong halocline at the base of the mixed layer is generally thought to impede effectively the vertical diffusion of heat between the Atlantic and Pacific Waters and the overlying cold, fresh layer (Toole et al., 2010; Linders and Björk, 2013; Lique et al., 2014). Nonetheless, internal mixing caused by bathymetric features (e.g., Shaw and Stanton, 2014; Lei et al., 2014) or mixing caused by a combination of brine-driven convection and vertical velocity shear below the mixed layer (e.g., Polyakov et al., 2013) could enhance the release of heat from the upper pycnocline into the near-surface layer. The Southern Ocean is characterized by a much weaker stratification, which allows heat from deep water masses to be much more easily entrained within the mixed layer (Martinson, 1990; Gordon and Huber, 1984, 1990; Wong and Riser, 2011). Warm subsurface waters also circulate onto the continental shelves, supporting high vertical heat fluxes even in these southernmost regions (e.g., Jacobs and Comiso, 1989).

1.1.3 A changing component of the climate system

Polar regions, especially the Arctic, experience large changes in response to climate warming, but the understanding of physical processes at play in these important parts of the Earth's climate system is limited by the paucity of available observations (Bourassa et al., 2013). Sea ice, which forms an intricate and tightly linked system with the underlying ocean, can be observed by means of remote sensing techniques. Passive microwave satellite products in particular have allowed to measure its areal distribution on a regular basis since the late 1970's.

On average over the period 1979-2013, Arctic sea ice varied seasonally from 6.4×10^6 km^2 in September to 15.2×10^6 km^2 in March. The interannual trend in total extent is negative in each month, with the largest decline in September at more than 13 % per decade (Parkinson, 2014a). The melt of Arctic sea ice in response to the warming of polar regions is visible for a variety of diagnostics, including diminished multiyear ice area (Comiso, 2011), earlier melt onset (Wang et al., 2013) and reduced sea ice season length (Parkinson, 2014b). Ice thickness is less easily monitored at large spatial and long temporal scales. Nevertheless, estimates based on upward-looking sonars mounted on submarines (e.g., Wadhams et al., 2011) or moorings (e.g., Hansen et al., 2013; Krishfield et al., 2014), on satellite altimetry (e.g., Kwok et al., 2012; Laxon et al., 2013; Zygmuntowska et al., 2014) and on airborne remote sensing platforms (e.g., Richter-Menge and Farrell, 2013; Kurtz et al., 2013) all attest to the

shrinking of the Arctic sea ice volume and to the removal of the old, thick ice in favor of younger, thinner ice. A recent synthesis of many of the available observational data yields a trend in annual mean ice thickness over the Arctic basin of -0.58 $\pm$ 0.07 m per decade over the period 2000-2012 (Lindsay and Schweiger, 2015). Positive trends in drift speed are also noted, which are mostly explained by the mechanical weakening of the sea ice cover rather than by changes in the atmospheric forcing by winds (Spreen et al., 2011; Gimbert et al., 2012; Vihma et al., 2012; Zhang et al., 2012; Kwok et al., 2013).

Although internal climate variability must be properly accounted for when considering the dramatic Arctic sea ice loss in the last years or decades (Swart et al., 2015), available observations indicate that a long-term downward trend does exist and that it is virtually certainly the consequence of anthropogenic climate change (Notz and Marotzke, 2012). High spring surface air temperatures and unusual wind patterns explain advances in melt onset and ice thinning (e.g., Rothrock and Zhang, 2005; Wang et al., 2013), but evidence is also building that a warmer ocean has also contributed to the Arctic sea ice decline (Carmack and Melling, 2011). Warm pulses in the Atlantic Water have been known to circulate within the Arctic basin (Polyakov et al., 2011, 2012). The substantial shoaling of this water mass in the central Arctic Ocean and the weakening of the Eurasian Basin upper-ocean stratification may have facilitated greater upward transfer of heat to the surface layer (Polyakov et al., 2010). Nonetheless, no warming trend of the Atlantic Water has been identified over the 1997-2008 time period, in contrast with the Summer Pacific Water of the Canada Basin, whose greater proximity with the surface makes it a likely contributor to the sea ice retreat in that area (Bourgain and Gascard, 2012).

The amplitude of the sea ice extent seasonal cycle is larger in the Antarctic than in the Arctic, with a minimum of 3.1 $\times$ 10^6 km^2 in February and a maximum of 18.5 $\times$ 10^6 km^2 in September, on average. The other noticeable contrast between both hemispheres is a slight increase in sea ice extent observed during all months (Parkinson, 2014a). Whereas its magnitude is subject to uncertainties (Eisenman et al., 2014), the overall expansion is clearly the result of regional opposing trends (e.g., Holland and Kwok, 2012). While in situ observations of ice thickness are even sparser than in the Northern Hemisphere and uncertainties in satellite estimates are larger (Kurtz and Markus, 2012), modeling studies indicate a positive trend in Antarctic sea ice volume close to 5 % per decade over the last few decades (Massonnet et al., 2013; Holland et al., 2014).

The increase in Antarctic sea ice is puzzling in a global warming context and no consensus has been reached yet so as to explain its origin. While the observational record of ice extent is too short to be conclusive on this matter,

indirect evidence supports the existence of multidecadal climate variability over the Southern Ocean, which puts the recent sea ice expansion in a broader context (e.g., Meier et al., 2013; Fan et al., 2014). General circulation models tend to confirm that the recent trends could be the result of internal variability (Polvani and Smith, 2013; Swart and Fyfe, 2013), but whether current models are an adequate tool to address the issue is questioned (Turner et al., 2012; Zunz et al., 2013). Physically, shifts in the atmospheric circulation appear to drive the sea ice changes (e.g., Holland and Kwok, 2012). Feedbacks within the ice-ocean system are then capable of sustaining or amplifying the initial perturbations (Zhang, 2007; Venables and Meredith, 2014; Goosse and Zunz, 2014). An enhanced oceanic stratification resulting from the melt of ice shelves has been proposed as a mechanism to reduce the heat flux at the sea ice base, hence explaining its growth (Bintanja et al., 2013), but the hypothesis validity is debated (Swart and Fyfe, 2013).

1.1.4 An important component of the climate system

Sea ice is a leading player not only in the climate of polar regions, but also in the Earth's climate as a whole. Changes in the ice cover have effects that contribute to amplify climate change (e.g., Caldeira and Cvijanovic, 2014). The most frequently cited mechanism is the ice-albedo feedback (Curry et al., 1995), which arises from the high albedo of ice and snow compared to open water. This feedback has an important role in the seasonal evolution of the sea ice cover (e.g., Maykut and Perovich, 1987; Timmermans, 2015). Since the global sea ice extent currently declines at a rate of -1.47 % per decade (Parkinson, 2014a), it has as well an impact of the radiative budget the planet on interannual time scales. It actually does not require that the ice disappears completely in summer from a region to come into action: in the Arctic, the transition from a multiyear to a thinner, seasonal ice cover with less snow also allows an enhanced transmission of solar radiation into the underlying ocean (Nicolaus et al., 2012; Perovich and Polashenski, 2012; Arndt and Nicolaus, 2014). Sea ice changes can furthermore affect the concentration of greenhouse gases, by influencing the uptake of carbon dioxide in the Southern Ocean (e.g., Delille et al., 2014) or terrestrial methane emissions in Arctic regions (e.g., Parmentier et al., 2015).

Due to the remoteness of Antarctica, changes in the Southern Hemisphere sea ice will have consequences on human activities only indirectly through other components of the climate system. Local ecosystems may nonetheless be directly impacted (e.g., Smith et al., 2014). By contrast, the larger declining sea ice trends in the Arctic Ocean already have practical implications at a number of ecological and economic levels. The reduced summer ice cover opens new

shipping routes and allows an enhanced marine access to the Arctic in general, which provides resource development opportunities (e.g., Rogers et al., 2013). The larger open water areas in summer result in the formation of larger waves (Thomson and Rogers, 2014; Wang et al., 2015). In addition to being a possible mechanism of breaking the remaining ice and accelerating its melt (e.g., Asplin et al., 2014), such waves could increase the vulnerability of Arctic coasts to erosion, inundation and damage to infrastructures (Barnhart et al., 2014). Under sea ice, the greater transmission of light affects the biological activity (Vancoppenolle et al., 2013; Arndt and Nicolaus, 2014). Finally, the sea ice loss has been associated to changes in the atmosphere (e.g., Blüthgen et al., 2012; Overland et al., 2012; Screen et al., 2012), with possible increased linkages with the mid-latitudes weather patterns (e.g., Sedlacek et al., 2011; Francis and Vavrus, 2012; Overland et al., 2015)

1.2 Ocean and sea ice modeling

Numerical models of the ocean and of the sea ice are extremely useful tools to gain insight into the processes that drive the changes observed in polar regions, including the ones that cannot be properly studied from existing measurements. Issuing predictions of the future behavior of the climate system is a second major purpose of coupled models (Goosse, 2015). Much work is presently dedicated to evaluate the importance of initial conditions for Arctic sea ice forecasts at seasonal to interannual time scales (e.g., Chevallier et al., 2013; Msadek et al., 2014; Day et al., 2014; Massonnet et al., 2015). Additionally, improving the physical accuracy of models is needed to refine predictions. This aspect even becomes dominant over the quality of initial conditions in determining the uncertainties of longer-term climate projections (Hawkins and Sutton, 2009).

1.2.1 Sea ice models and ice thickness distributions

The present work is based on the Louvain-la-Neuve sea Ice Model (LIM, Vancoppenolle et al., 2009b; Rousset et al., 2015), used within the Nucleus for European Modelling of the Ocean (NEMO, Madec, 2008), a state-of-the-art modeling framework for oceanographic research, operational oceanography, seasonal forecasts and climate studies. LIM is one of the most widely used large-scale sea ice models in the climate community. The core features of its latest version are mostly shared with other models of the same type, and the most important are listed here.

The sea ice state is determined by a set of prognostic variables, namely ice concentration, ice volume per unit area, ice internal energy, ice salt content,

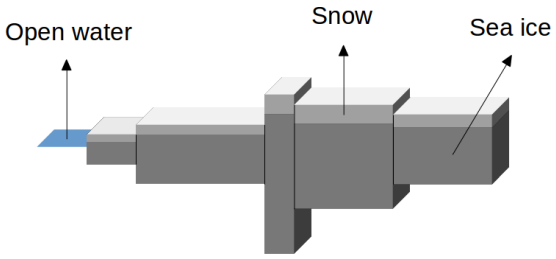

Figure 1.2: Schematic illustration of a grid cell in which sea ice is represented by an ITD with 5 ice thickness categories. Each category is characterized by specific state variables, including for instance the properties of its snow cover.

ice velocity, snow volume per unit area and snow internal energy. Ice thermodynamics are considered as a one-dimensional vertical heat conduction and storage problem, which is treated following Bitz and Lipscomb (1999). A specific feature of LIM is its advanced halodynamics scheme representing brine dynamics and their impact on ice thermal properties (Vancoppenolle et al., 2009a). Sea ice dynamics are governed by a momentum equation taking into account the air-ice and ocean-ice stresses, the Coriolis force, the sea surface tilt and the internal forces arising from deformation. The latter are derived considering an elastic-viscous-plastic rheology (Hunke and Dukowicz, 1997), in a recently revised formulation (Bouillon et al., 2009, 2013). Horizontal advection of ice state variables on the model grid is based on a second-order moment-conserving scheme (Prather, 1986). Most current large-scale sea ice models, including LIM, treat the ice as a biologically and chemically inert layer on top of the ocean, but changes are underway (e.g., Moreau et al., 2015).

The model component that is of central interest to the present work is the so-called ice thickness distribution (ITD, Thorndike et al., 1975). The spatial heterogeneity of ice properties exists at scales as small as a few meters and within single ice floes (Fig. 1.1). In spite of the ever-increasing resolution of models, even regional configurations have grid cell sizes of the order of a few kilometers (e.g., Rousset et al., 2015), meaning that the variability of ice thickness cannot be explicitly represented. Yet, this variability is crucial to the evolution of the sea ice cover, the atmosphere above and, possibly, the underlying ocean. The winter heat losses from the ocean to the atmosphere, and hence the ice growth rates, strongly depend on the ice thickness. Heat exchanges for ice in the 0 to 0.4 m thickness range are for instance one to two orders of magnitude larger than for thick, multiyear ice (Maykut, 1978). In summer, on the other hand, solar radiation is primarily absorbed in open waters, which implies that their contribution dominates the ocean heat budget, and thereby

influences the ice mass balance (Maykut, 1982). The ITD function $g(h)$, first introduced by Thorndike et al. (1975), is defined as:

$$\int_{h_1}^{h_2} g(h)dh = \frac{1}{R}A(h_1, h_2),$$

where R is a control area larger than the typical heterogeneous sea ice features and $A(h_1, h_2)$ the area occupied in R by ice with thickness between h_1 and h_2. Although omitted for clarity, $g(h)$ is also a function of time and position. In models, the ITD is usually discretized into 5 to 20 ice thickness categories. The grid cells are therefore split into an open water fraction and the chosen number of ice categories, each of them having a given area and specific state variables (Fig. 1.2). Transfers between the categories occur following thermodynamics and deformation processes (e.g., Flato and Hibler, 1995). The introduction of this formalism in models has been found to improve the simulation of ice growth and melt (e.g., Hibler, 1980; Holland et al., 1997). The dependence of results on how the ITD is implemented keeps being investigated nowadays (Komuro and Suzuki, 2013; Castro-Morales et al., 2014; Hunke, 2014) and a growing number of modeling groups adopt such a representation of subgrid-scale ice thickness variations.

A recent and comprehensive review of sea ice modeling is provided by Hunke (2010), whereas current challenges in simulating sea ice in Earth system models are addressed in Notz (2012). Active research is dedicated to the identification of processes that modulate the ice variability at seasonal to centennial time scales. Attempts in that direction include the improvement of the representation of snow covering sea ice (Lecomte et al., 2013, 2015), of melt ponds (Hunke et al., 2013; Lecomte et al., 2015) and of atmospheric and oceanic drag coefficients (Lu et al., 2011; McPhee, 2012; Lüpkes et al., 2012, 2013; Tsamados et al., 2014). New methods for describing the ice dynamics are also intensively studied, among which the anisotropic (Tsamados et al., 2013) or elasto-brittle (Girard et al., 2011; Bouillon and Rampal, 2015) rheologies. Finally, the representation of landfast ice in large-scale models is a further ongoing research topic (Itkin et al., 2015; Lemieux et al., 2015).

1.2.2 Model evaluation

If some questions can be investigated using stand-alone sea ice models, others, including the ones addressed in the present work, need a coupling with an interactive ocean model. Relevant details on the coupling in the case of NEMO-LIM are given in the following chapters. The evaluation of the interactions between ice and ocean is however complicated by the paucity of adequate observations. In contrast to sea ice which can be monitored at least

partly from space, under-ice and subsurface ocean measurements can only be made from in situ instruments. The greatest challenge is perhaps the observation of the Southern Ocean under the seasonal Antarctic ice, where the technical difficulties of sampling an ice-covered ocean add up to the extreme remoteness of the region (Rintoul et al., 2014).

Historically, most hydrographic measurements were performed during research cruises. They were therefore scarce in space and in time, in addition to being biased towards the summertime in seasonally ice-covered areas. Although still useful for process studies (e.g., Lane-Serff and Stansfield, 2013), such specific observations have been complemented by others methods offering a larger data coverage. Since 2000, the Argo array of thousands of free-drifting profiling floats has allowed an unprecedented, continuous sampling of the upper 2000 m of the global ocean (e.g., Dong et al., 2008; Sallée et al., 2010; Ren et al., 2011). Since traditional Argo floats need to surface regularly in order to transmit data and to obtain their position, the presence of sea ice is a major obstacle to their functioning. Improvements are underway with the implementation of ice-avoidance techniques (e.g., Wong and Riser, 2011). In the Antarctic, another very promising method consists in equipping seals with conductivity-temperature-depth sensors (e.g., Arthun et al., 2013; Roquet et al., 2013). By foraging south of the Antarctic Circumpolar Current, they provide since 2004 data about the hydrography of the poorly-sampled ice-covered Southern Ocean, even at the core of the freezing season. In the Arctic Ocean, information of similar value is obtained from the ice-tethered profilers, which have also been deployed since 2004 (Krishfield et al., 2008). These automated profiling systems anchored on ice floes measure the properties of the upper few hundreds meters of the ocean, in all seasons and wherever the floes are drifting. Together, these data sources provide new ways to assess the performances of models in polar regions, and in particular the evolution of the mixed layer in relation to sea ice.

All aspects of current climate models cannot be precisely evaluated. Nevertheless, the ocean-sea ice-atmosphere coupled models used in the Intergovernmental Panel on Climate Change Fifth Assessment Report (IPCC, 2013), which constitute the state of the art in the field, are known to suffer from a number of clear biases. In the Northern Hemisphere, the decline in September sea ice extent (Stroeve et al., 2012) and the rate of ice volume loss (Stroeve et al., 2014) over the last decades are underestimated compared to observational estimates. Moreover, the simulations fail to capture the accelerated motion associated to the mechanical weakening of the ice cover (Rampal et al., 2011). The model skills in the Southern Hemisphere are even lower. The climatological sea ice extent seasonal cycle is not as accurately reproduced as in the Arctic and the models exhibit a decreasing long-term trend instead of the

expansion noted in the satellite data (Turner et al., 2012; Shu et al., 2015). The weak stratification in the Southern Ocean makes convection and vertical mixing processes highly sensitive to the configuration details (Heuzé et al., 2015; Kjellsson et al., 2015; Stössel et al., 2015). Even in models forced by specified atmospheric fields, the summer mixed layer depths are often underestimated, while winter mixed layers are usually too deep (Huang et al., 2014; Downes et al., 2015). The interactions between the ocean, the ice and the atmosphere differ strongly among models, preventing a clear understanding of feedbacks that likely control the sea ice variability (Close and Goosse, 2013). Finally, the formation of bottom water masses is poorly represented (Heuzé et al., 2013).

1.3 Objectives of the thesis

Current climate models show large uncertainties when simulating the present-day sea ice coverage and when projecting sea ice changes in both hemispheres in response to enhanced atmospheric greenhouse gas concentrations. This is inevitably associated with biases in the simulation of the under-ice ocean dynamics. These issues arise from a combination of various factors, but a misrepresentation of the subtle interplay between sea ice and the underlying ocean, and of the oceanic mixed layer processes in polar regions, is likely a part of the problem. The common thread that runs through this thesis is the subgrid-scale **heterogeneity of sea ice-ocean interactions**, and the way it can be **represented in large-scale models**. In this section, we expose this concept in more details and list the scientific questions addressed in the present work.

1.3.1 Heterogeneous sea ice-ocean interactions

Sea ice is an extremely heterogeneous medium that fundamentally modifies the ocean surface conditions. The air-ice-water interactions are therefore variable, at horizontal scales as small as a few meters. The largest differences in surface conditions are found between the ice-covered and ice-free fractions of a region, but gradients also exist in relation to variations in ice characteristics. In summer, for instance, solar radiation enters the ocean in open water without being obstructed, which contributes the most to the warming of the upper water column (Maykut and McPhee, 1995). Solar energy is, however, able to penetrate the ice as well, and a fraction of it, determined by the variable thickness and physical properties of the snow and sea ice, reaches the ice-ocean interface (Nicolaus et al., 2013; Katlein et al., 2015). In winter, the most telling example is the formation of new ice and the associated brine rejections. Compared to the under-ice, these are larger by more than one order of magnitude in leads and polynyas, where the seawater is in direct contact with the cold

atmosphere. Nonetheless, since the insulating properties of ice strongly depend on its thickness and on its snow cover, the ice growth rate also varies in relation to the heterogeneity of ice and snow, especially when these are thin (Maykut, 1978).

Following the same line of argument, air-water and ice-water exchanges have spatially variable effects on the sea surface temperature and salinity, hence on upper-ocean stratification and vertical mixing. Impacts on the atmosphere above are similarly heterogeneous, but this is not the focus of the present study. For clear practical reasons, field measurements have mostly emphasized the large contrast between open water and ice-covered areas. Winter observations have demonstrated the existence of convective plumes of salty water within leads, caused by negative buoyancy fluxes related to intense freezing rates (Morison et al., 1992; Morison and McPhee, 1998; Muench et al., 1995). Brine-induced convection has also been found responsible for vigorous mixing in the mixed layer below leads in modeling studies (e.g., Kantha, 1995). The localized nature of the brine rejection in leads a few to hundreds meters wide induces a specific ocean response, compared to a widespread salt input at the sea surface. In case the lead is slowly moving, the salt plumes sink to the bottom of the mixed layer where they spreads horizontally. Counterintuitively, the depth of the mixed layer is reduced and the gain in salinity is mostly limited to its lower portion (Matsumura and Hasumi, 2008; Nguyen et al., 2009; Jin et al., 2012). A salt input spread out at the surface, on the other hand, generates large-scale convection which deepens the mixed layer and increases its salinity in a vertically uniform manner. Through a comparison of vertical mixing schemes commonly used in coarse resolution models with large eddy simulations, Losch et al. (2006) have confirmed that the former are designed to work with homogeneous surface boundary conditions. If heterogeneous fluxes of buoyancy due to a partial sea ice cover cannot be resolved by the computational grid, these schemes fail to reproduce the upper ocean mixing and structure simulated by the large eddy methods. In summertime, the differential solar warming between the open water and the under-ice is also of importance, in particular to the ice lateral melt and to the formation of a cap of fresh water at the leads surface, as demonstrated by Holland (2003) when analyzing the SHEBA campaign results (Surface Heat Budget of the Arctic Ocean).

1.3.2 Representation in models

Today, advanced sea ice models often include an ITD (e.g., Zhang and Rothrock, 2003; Hunke et al., 2015; Rousset et al., 2015). A representation of the subgrid-scale variability in ice properties exists in such models, and heteroge-

neous ocean surface fluxes have therefore long been available. Actually, even earlier models, which represented ice as a slab of uniform thickness, computed the fractional coverage of the ice within a grid cell, meaning that they were already able to distinguish between the atmosphere-ocean and ice-ocean fluxes. In any case, without a specific coupling strategy to an ocean model, the subgrid-scale fluxes from the sea ice models must be merged so that information is eventually exchanged with the single water cell underneath. This prevents the simulation of the heterogeneity of the oceanic processes described in the previous section. The aggregation of subgrid fluxes relies on the implicit assumption that lateral mixing between the different parts of the grid cells occur at time scales shorter than the model time step. In reality, such horizontal homogenization must definitely occur, but most likely not at the same rate in all conditions. In order to test the influence of the above-mentioned assumption and its consequences, parameterizations have to be developed to take into account the first order effects of the subgrid-scale processes that cannot be explicitly simulated (Goosse, 2015).

Examples exist in the literature of such parameterizations designed to represent convection occurring at horizontal scales smaller than the model grid cells. The ones listed below are not related to sea ice, nor necessarily to heterogeneous ocean surface conditions, but useful insight can be gained from them nonetheless. Using the penetrative plume scheme of Paluszkiewicz and Romea (1997), Kim and Stössel (2001) achieved a reduction of excessive open-ocean deep convection in the Southern Ocean in a coarse resolution ocean and sea ice model, and thereby obtained more realistic simulated deep water properties. Campin et al. (2011) explored the efficacy of a "super parameterization", consisting in embedding local non-hydrostatic high resolution models at each vertical column of a coarser resolution hydrostatic model. Although very complex, this approach allows to resolve, rather than parameterize, small-scale convective processes at much less computational cost than fully non-hydrostatic calculations. More recently, Ilıcak et al. (2014) implemented a two-column vertical mixing scheme to simulate heterogeneous ocean convection. Different density profiles are assumed in the two columns, mimicking the subgrid-scale variability induced by unresolved eddies. The simulation results indicate that deeper convection in the least stratified column reduces a warm model bias at depth in the Atlantic and Southern Oceans.

In the context of sea ice modeling, first attempts to parameterize the impacts of localized brine rejections in leads were from Duffy and Caldeira (1997) and Duffy et al. (1999). They introduced the concept of brine rejection parameterization (BRP), which consists in distributing the salt rejected during sea ice growth within or below the mixed layer, instead of placing it in the top oceanic model layer, hence imitating the effects of salt plumes revealed in observa-

tions and model studies. Their focus was the intermediate and deep salinities and temperatures and the convective activity around Antarctica, whose simulation was improved with the BRP. Nguyen et al. (2009) and Jin et al. (2012) subsequently refined the formulation of the parameterization and tested its influence in the Arctic Ocean. Using a power-law distribution of the rejected brines, both studies showed a better representation of the cold halocline and a reduction of excessive mixed layer depths. In a way similar to Ilıcak et al. (2014), Holland (2003) and Jin et al. (2015) implemented explicit subgrid-scale mixing schemes and examined their impact on the Arctic sea ice and ocean. The principle is to apply fluxes and to compute oceanic vertical mixing separately in columns corresponding to the open water and ice fractions of grid cells, and also possibly distinguishing between ice thickness categories. Holland (2003) investigated the warming and freshening of summertime leads observed during the SHEBA campaign in a one-dimensional ocean-sea ice model. Jin et al. (2015) considered simulated winter mixed layer depths and the upper ocean salinity structure in a full three-dimensional model configuration, and concluded that their two-column mixing scheme achieved more improvements in salinity than the BRP.

1.3.3 Questions addressed and outline

The present modeling study aims at answering the following three main scientific questions.

- What small-scale sea ice-ocean processes are at play under an heterogeneous ice cover?
- How can these subgrid-scale, heterogeneous interactions be represented in large-scale sea ice-ocean models?
- Can we quantify their influence on the sea ice and underlying ocean?

These questions are addressed throughout the next three chapters using schemes of increasing complexity. In Chapter 2, we first study the simple BRP method to parameterize the effects of localized brine rejections in winter leads. Chapter 3 sets the context for the mixing schemes tested in Chapter 4, by examining in details the subgrid-scale heterogeneity of ocean surface conditions under sea ice. It also provides elements to answer the first question. In

Chapter 4, two versions of a multi-column ocean mixing schemes are tested. The simplest one requires the columns to be homogenized at each time step, while the second allows their different properties to persist over a given time scale.

In Chapter 2, the BRP formulation of Nguyen et al. (2009) is introduced into the global ocean-sea ice model NEMO-LIM, on which this whole thesis is based. In contrast to earlier studies, we conduct the analysis in a global configuration and examine the results both in the Arctic and in the Antarctic. Despite significant differences in model setup, we confirm the effects previously noted, namely strong reductions in mixed layer depths in the sea ice zone. However, a careful comparison with observational estimates based on ice-tethered profilers and seals data reveals that this decrease is in general too strong, which makes us question the efficiency of the BRP. Although the method has a sound physical basis for the brine rejected in a slowly moving lead, we conclude that it is an oversimplification to apply it in all conditions to all the salt rejected by sea ice formation. An innovative method is proposed to improve the results of the BRP. Our final recommendation, nonetheless, is to turn to more explicit approaches.

Examples of such explicit schemes are the ones suggested by Holland (2003) and Jin et al. (2015). In Chapter 3, we prepare the ground for an in-depth revision and extension of these studies. As mentioned above, heterogeneous ocean surface conditions are available in current ocean and sea ice models, with especially detailed information in case an ITD is included in the ice component. In situ under-ice observations are still far too sparse to undertake a thorough examination of these subgrid-scale fluxes at large scales and in all seasons. This would be possible using models, but the required analysis was nevertheless missing from the literature. We fill this gap using the NEMO-LIM results. Even without the subsequent implementation of a subgrid-scale mixing scheme, the results of this chapter are of interest to understand the origin of heterogeneous ice-ocean interactions. We determine which variables differ the most between the ice-free and ice-covered parts of a grid cell, and demonstrate that some of them are characterized by a strong dependence to the heterogeneous nature of ice properties, including thickness and snow cover. This latter aspect had been so far partly overlooked.

The central topic of Chapter 4 is the development, inclusion and analysis of a multi-column ocean mixing scheme in NEMO-LIM (Fig. 1.3). The basic idea is to use the subgrid-scale fluxes provided by the sea ice model to drive vertical mixing computations separately in columns corresponding to the open water fraction and to the ice thickness categories. It allows to investigate explicitly the processes associated with the spatial heterogeneity of ice-ocean interactions within the horizontal scope of a grid cell. The impacts

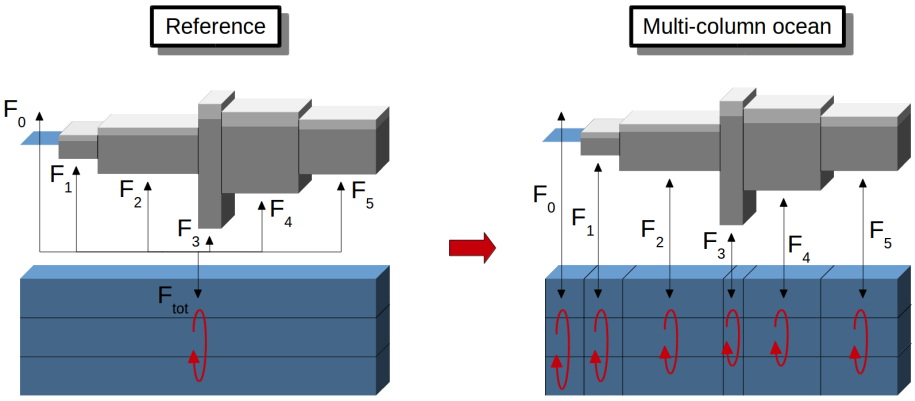

Figure 1.3: Schematic illustration of the differences between the reference and multi-column ocean codes. In the reference case, the subgrid fluxes (F_n) from the ITD sea ice model are aggregated before being transmitted to the single ocean grid cell underneath, and the ocean vertical mixing computation (represented by a red arrow) is unique. In the multi-column case, the water column is divided into several sub-columns, corresponding to the open water fraction and to the ice thickness categories. The specific fluxes are applied at the surface of the sub-columns and the oceanic vertical mixing is computed separately in each of them.

of the scheme on the ocean simulation in both polar regions are examined, as well as the feedbacks on the ice cover itself. Changes in ice properties are indeed caused by the different oceanic heat fluxes at the base of each thickness class, as a result of different oceanic conditions below. Holland (2003) implemented a analogous scheme in a one-dimensional model configuration. Jin et al. (2015) did a similar work for a three-dimensional model of the Arctic Ocean, but they homogenized the properties of the columns at each time step and based their analysis on debatable assumptions regarding the distribution of fluxes at the surface. The major novel contribution of this thesis is our scheme's capability to let the columns evolve separately over several time steps in a three-dimensional simulation. In addition to being a proof-of-concept study, our results attest that the homogenization time scale between the columns is actually the key parameter in the scheme. The magnitude of the changes induced in model results by the new representation of subgrid-scale sea ice-ocean interactions depends strongly on this time scale, whose value is likely variable in time and in space. It is worth noting that, in spite of clear similarities in the methods employed, our scheme was developed independently from the studies by Ilıcak et al. (2014) and Jin et al. (2015).

CHAPTER 2

LIMITATIONS OF SIMPLE BRINE REJECTION PARAMETERIZATIONS

Abstract

The subtle interplay between sea ice formation and ocean vertical mixing is hardly represented in current large-scale models designed for climate studies. Convective mixing caused by the brine release when ice forms is likely to prevail in leads and thin ice areas, while it occurs in models at the much larger horizontal grid cell scale. Subgrid-scale parameterizations have hence been developed to mimic the effects of small-scale convection using a vertical distribution of the salt rejected by sea ice within the mixed layer, instead of releasing it in the top ocean layer. Such a brine rejection parameterization is included in the global ocean–sea ice model NEMO-LIM3. Impacts on the simulated mixed layers and ocean temperature and salinity profiles, along with feedbacks on the sea ice cover, are then investigated in both hemispheres. The changes are overall relatively weak, except for mixed layer depths, which are in general excessively reduced compared to observation-based estimates. While potential model biases prevent a definitive attribution of this vertical mixing underestimation to the brine rejection parameterization, it is unlikely that the latter

can be applied in all conditions. In that case, salt rejections do not play any role in mixed layer deepening, which is unrealistic. Applying the parameterization only for low ice–ocean relative velocities improves model results, but introduces additional parameters that are not well constrained by observations.

2.1 Introduction

Intense turbulent mixing at the surface of the ocean results in a mixed layer whose dynamics regulates the exchanges between the atmosphere and the ocean interior. In polar regions, the mixed layer development is strongly affected by the presence of sea ice. Sea ice dampens direct inputs of heat, momentum and mass from the air, while it generates buoyancy fluxes at the sea surface when it forms or melts. In turn, mixed layer characteristics impact the sea ice energy balance by modulating the oceanic heat flux at the base of the ice layer.

The large difference between seawater and sea ice salinities, the latter being much lower, implies strong brine rejections during ice formation, which may lead to destabilization and hence convective mixing of the upper portion of the water column. This subtle interplay between sea ice formation and mixing of the surface layer is currently poorly represented in large-scale ocean-sea ice models. Indeed, convection due to surface salt input occurs in models at the grid cell scale (typically from 10 to 100 km), while it is likely to prevail in the real ocean in leads and thin ice areas, at horizontal scales ranging from 100 m to a few kilometers (Duffy and Caldeira, 1997; Nguyen et al., 2009; Jin et al., 2012).

The errors caused by the misrepresentation of small-scale convection in large-scale ocean models are examined by Jin et al. (2012). In this study, a model is run on a 100×100 horizontal grid point domain at 1 km and 30 km resolutions, and the ocean response in a 30 km $\times$ 30 km box to a surface brine rejection is investigated. The box therefore consists of 30×30 grid points at 1 km resolution and of a single column at 30 km resolution. On the one hand, in the high resolution simulations, a localized brine rejection results in a salt plume that sinks to the bottom of the mixed layer where it spreads horizontally. The mixed layer actually shoals and the increase in salinity is greater at its base than at the surface. The same process has been observed and described in laboratory experiments and field studies (Nguyen et al., 2009, and references therein). On the other hand, in the low resolution simulations, where the salt input is by default spread out at the surface of the 30 km $\times$ 30 km box, large-scale convection induces a deepening of the mixed layer and a vertically uniform salinity increase.

Subgrid-scale brine rejection parameterizations have been developed and included in models to address the excessive mixing issue and to mimic the effects of small-scale convection. Their basic principle is to distribute vertically the salt rejected by sea ice within or below the mixed layer, instead of releasing it in the top ocean layer. Two preliminary studies (Duffy and Caldeira, 1997; Duffy et al., 1999) distributed the salt uniformly in the upper 160 m and down

to the depth where density becomes 0.4 kg/m^3 higher than at the surface. They noted improvements in the simulated intermediate and deep salinities around Antarctica, as well as in the modeled temperatures and convective activity. Subsequent implementations consisted in a power-law distribution of rejected brines within the mixed layer (Nguyen et al., 2009; Jin et al., 2012). Focusing only on the Arctic, results showed improved modeling of the Arctic cold halocline and reduction of excessive mixed layer depths. Similar ideas have also been used in the context of paleoclimate modeling. By releasing brines due to sea ice formation at the bottom of the ocean, Bouttes et al. (2010) improved the simulated carbon cycle during the last glacial maximum in an intermediate complexity climate model.

In the present study, the brine rejection parameterization scheme of Nguyen et al. (2009) is introduced into the global ocean-sea ice model NEMO-LIM3. The aim is to assess in details its effects on the mixed layer depth and properties, in both the Arctic and Antarctic, using a recently published mixed layer climatology (Schmidtko et al., 2013) and hydrographic data provided by animal-borne instruments in the Southern Ocean (Roquet et al., 2013). Because the vertical mixing scheme in NEMO is different from the one used in the above-mentioned studies, this will also provide an independent confirmation or invalidation of the results previously obtained for the Arctic. Furthermore, the feedbacks triggered by the parameterization on the sea ice cover are examined.

The chapter is organized as follows. The NEMO-LIM3 model, the experimental design and the brine rejection parameterization are presented in Section 2.2. Observational data are described in Section 2.3. Section 2.4 includes the analysis of the simulations results and a discussion of the limitations of our experiments and of the parameterization, and presents a simple method to refine the latter. A summary of our findings and concluding remarks are given in Section 2.5.

2.2 Brine rejection parameterization in the ocean-sea ice model NEMO-LIM3

2.2.1 Model configuration

NEMO-LIM3 is a global ocean-sea ice model routinely used in climate studies. The ocean engine of NEMO (Nucleus for European Modelling of the Ocean) is a finite-difference, hydrostatic, free-surface, primitive-equation model (Madec, 2008). It is coupled to LIM3 (Louvain-la-Neuve sea Ice Model), a dynamic-thermodynamic sea ice model with a representation of the subgrid-scale distributions of ice thickness, enthalpy and salinity (Vancoppenolle et al.,

2009b). The explicit inclusion of brine entrapment and drainage makes the sea ice salinity variable both in space and in time. We use version 3.5 of NEMO, with modifications to the sea ice code that include changes in the time stepping and a reformulation of ice-ocean fluxes allowing to track the different contributions to the ice mass, salt and heat balances (Rousset et al., 2015). Mesoscale eddies are parameterized following Gent and Mcwilliams (1990).

The treatment of oceanic vertical mixing is of particular interest in this study. We use the so-called TKE mixing scheme, introduced in an earlier version of the model by Blanke and Delecluse (1993) and progressively updated since then (Madec, 2008). The vertical eddy viscosity and diffusivity depend on the prognostically computed turbulent kinetic energy (TKE) and on diagnostic non-local turbulent length scales. The TKE evolves in time through production by vertical shear, destruction by stratification, vertical diffusion and dissipation. In theory, this scheme solves the issue of statically unstable density profiles in hydrostatic models because, in that case, the stratification destruction term actually becomes a source of TKE, thus yielding high mixing coefficients. An enhanced vertical diffusion scheme is however used to ensure static stability in the top ocean layers, where turbulent length scales are bounded by the distance to the surface.

Our experimental design is largely similar to the NEMO-LIM3 simulation of Massonnet et al. (2011), where additional details can be found. The model is initialized in 1948 using climatological temperature and salinity data from the World Ocean Atlas 2001 (Conkright et al., 2002), and is run until the end of 2013. The atmospheric forcing is provided by the NCEP/NCAR surface air temperature and wind reanalysis data (Kalnay et al., 1996), and by monthly climatologies for relative humidity, cloudiness, precipitation and river runoffs. Surface heat fluxes are computed following Goosse (1997), while the ice-ocean coupling is formulated as in Goosse and Fichefet (1999). Simulations are performed on the quasi-isotropic global tripolar grid ORCA1, based on the semi-analytical method of Madec and Imbard (1996), which has 1° resolution in the zonal direction. Vertical discretization is based on a partial step z coordinate, meaning that the thickness of the bottom layer is allowed to vary to provide a better representation of the bathymetry (Adcroft et al., 1997). The thicknesses of the 46 levels otherwise range from 6 m at the surface to 20 m at 100 m depth, and reach 250 m for the bottommost layer.

Among the differences in setup compared to Massonnet et al. (2011) are the more recent model version used, tuned ice-ocean drag coefficient (from 5×10^{-3} to 3×10^{-3}) and snow thermal conductivity (from 0.31 W K^{-1} m^{-1} to 0.25 W K^{-1} m^{-1}), and a different implementation of the sea surface salinity restoring towards the PHC3 climatology (Polar Science Center Hydrographic Climatology, Steele et al., 2001). The restoring consists in a damping term in

Table 2.1: Sea ice metrics in observations or reanalyses, and in the reference (REF) and BRP experiments (see Table 2.2 for details). Sea ice extent is compared between 1983 and 2012 with passive microwave products generated with the Bootstrap algorithm (Comiso, 2000). Arctic sea ice volume estimates are from the PIOMAS reanalysis (Schweiger et al., 2011) over the 1983-2013 period. The Antarctic sea ice volume trend is from the model reconstruction by Massonnet et al. (2013) between 1980 and 2008.

	Obs./reanalysis	REF	BRP
Arctic			
Max. monthly extent (10^6 km^2)	15.5	16.5	16.5
Min. monthly extent (10^6 km^2)	6.7	7.7	7.7
Trend extent (10^3 km^2 year^{-1})	-53	-58	-57
Max. monthly volume (10^3 km^3)	27.8	33.3	33.2
Min. monthly volume (10^3 km^3)	11.2	17.3	17.2
Trend volume (km^3 year^{-1})	-346	-374	-377
Antarctic			
Max. monthly extent (10^6 km^2)	19.2	18.4	18.6
Min. monthly extent (10^6 km^2)	3.2	6.2	5.8
Trend extent (10^3 km^2 year^{-1})	+21	+37	+36
Max. monthly volume (10^3 km^3)	n/a	14.4	14.1
Min. monthly volume (10^3 km^3)	n/a	3.7	3.3
Trend volume (km^3 year^{-1})	$+36 \pm 34$	+83	+66

the surface freshwater budget and is necessary to avoid spurious model drift outside the polar regions. Its time scale is 310 days for a 50 m mixed layer. Here, the restoring term is multiplied by $(1 - c)$, with c the sea ice concentration. This suppresses its influence almost completely in intense ice formation areas, and ensures that the effects of the brine rejection parameterization are not altered.

2.2.2 Simulated sea ice in the reference experiment

Despite changes in model configuration, sea ice results remain relatively close to the ones obtained by Massonnet et al. (2011). Key figures are given in Table 2.1.

In the Arctic, the sea ice extent mean seasonal cycle is well reproduced compared to observations (Comiso, 2000), showing only a positive bias around 1×10^6 km^2 throughout the year. The ice volume appears significantly overestimated with respect to the PIOMAS reanalysis using data assimilation (Pan-Arctic Ice-Ocean Modeling and Assimilation System, Schweiger et al., 2011), but the offset is essentially caused by spurious ice accumulations in narrow straits in the Canadian Arctic Archipelago, not accurately represented in the model at 1° resolution. The phase and amplitude of the ice volume seasonal cycle actually closely match the PIOMAS data. Finally, both ice extent and

volume trends are in very good agreement with observations and reanalysis estimates.

In the Southern Hemisphere, the main discrepancy with available observations is an underestimation of the amplitude of the ice extent seasonal cycle, especially at the summer minimum. The simulated upward trend in sea ice extent is also too large, as is the trend in ice volume against the model reconstruction with data assimilation by Massonnet et al. (2013). Compared to the ASPeCt dataset based on shipboard observations (Antarctic Sea ice Processes and Climate, Worby et al., 2008), the model tends to overestimate the sea ice thickness, except northeast of the Antarctic Peninsula and along the coasts of East Antarctica and eastern Ross Sea, where the opposite occurs. The mean absolute error in ice thickness is 43 cm.

This brief evaluation of the sea ice results in the reference experiment shows that NEMO-LIM3 is clearly appropriate to study the impacts of a brine rejection parameterization on the oceanic component of the system. The model skill in the representation of this latter component is discussed in Section 2.4 together with the changes induced by the parameterization. Nevertheless, we note that Antarctic sea ice does not melt enough in summer in the model, which could lead us to underestimate the parameterization effect in the Southern Ocean when ice freezes up again in autumn.

2.2.3 Brine rejection parameterization

In the standard model configuration, all surface fluxes linked to the presence of sea ice are applied in the first ocean layer. In order to mimic small-scale convection associated with sea ice formation, brine rejection parameterizations (BRPs) distribute the rejected salt directly within the mixed layer. Owing to its positive buoyancy, low salinity water resulting from sea ice melt is always placed in the uppermost layer.

Based on salt plume physics, laboratory and numerical experiments, Nguyen et al. (2009) found the optimal brine vertical distribution $s(z)$ to be a power law:

$$s(z) = \begin{cases} Az^n & \text{if} \quad z \leq D \\ 0 & \text{if} \quad z > D \end{cases}$$

where z is depth, A a normalizing factor equal to $\frac{n+1}{D^{n+1}}$, D a measure of the mixed layer depth (MLD) and $n = 5$. The large n implies that most of the salt is rejected at the bottom of the mixed layer. The same value was found independently by Jin et al. (2012) for small leads using their high resolution model. Since the shape of the distribution seems well constrained, we only test here the sensitivity of the BRP to the distribution maximum depth.

Table 2.2: List of sensitivity experiments.

Experiment	Parameterization	Maximum depth D
REF	no	-
BRP-1	yes	1 level above MLD.01
BRP	yes	MLD.01
BRP+1	yes	1 level below MLD.01
BRP_3	yes	MLD.03
BRPv	for low ice-ocean relative velocities	MLD.01

Nguyen et al. (2009) took D as the depth corresponding to a density gradient of 0.02 kg m^{-4}. Jin et al. (2012) rather used the MLD provided in their model by the turbulence k-profile parameterization. In NEMO, the mixed layer base is determined by default by a density difference of 0.01 kg m^{-3} compared to the value at 10 m depth, which is the second oceanic level in our vertical discretization. This low density threshold is found to be appropriate to identify the almost perfectly homogeneous simulated mixed layers. An additional diagnostic, based on the 0.03 kg m^{-3} threshold recommended by de Boyer Montégut et al. (2004) for observed density profiles, is also implemented. These mixed layers depths are denoted MLD.01 and MLD.03, respectively. Besides the reference simulation where the BRP is disabled, four sensitivity experiments are performed, in which the BRP is turned on and D is set to one level above MLD.01, MLD.01, one level below MLD.01 and MLD.03. The latter corresponds almost everywhere to the deepest distribution. A sixth experiment, in which the BRP is only activated for low ice-ocean relative velocities, is mentioned here for completeness and is further discussed in Section 2.4.3. The experiments are summarized in Table 2.2.

An important hypothesis, made here as well as in all previous studies, is that all the salt is rejected by sea ice in a localized manner (for instance in leads). This amounts to saying that all the salt originating from sea ice has to be handled with the parameterization, thus distributed vertically.

2.3 Observational data

Observational data used to validate the ocean model results come from two sources: the MIMOC climatology (Monthly Isopycnal and Mixed layer Ocean Climatology) and the MEOP-CTD hydrographic dataset (Marine Mammals Exploring the Oceans Pole to Pole).

The MIMOC global upper-ocean climatology (Schmidtko et al., 2013) is based on conductivity-temperature-depth (CTD) profiles from the World Ocean Database (i.e. shipboard data), Argo floats and automated ice-tethered

profilers (ITP). The inclusion of the latter increases dramatically the number of upper-ocean observations in the Arctic Ocean, in all seasons, since 2004 (Krishfield et al., 2008). The MIMOC product includes MLDs computed from individual profiles with the Holte and Talley (2009) algorithm. We use the weighted mean monthly fields.

In the Southern Ocean, most of the observations used to construct the MIMOC climatology come from summertime cruises, because Argo floats can hardly sample the ocean beneath sea ice and because there is no equivalent to the ITP project in the Antarctic. Therefore, we also compare our results with the MEOP-CTD dataset (Roquet et al., 2011, 2013), a calibrated compilation of temperature and salinity (T/S) profiles collected by hundreds of seals equipped with CTD sensors between 2004 and 2011. These seal-derived data are nowadays the largest source of hydrographic information south of the Antarctic Circumpolar Current (ACC). A MLD climatology is built from the dataset in the following way.

For each profile, the MLD.01 and MLD.03 are computed as in the model, except that the reference density value is taken at 15 m depth. This is very often the first available T/S value in the profile. Profiles without data at this depth are rejected. In some cases, the required density difference is not reached until the deepest T/S measurement, because the seal did not reach the mixed layer base or because the mixed layer extended down to the seafloor. Including such profiles barely changes the resulting climatology, hence we keep the maximum depth with data as a lower limit for the MLD. Finally, for each ORCA1 grid cell and each month, the available MLD values are averaged to obtain the climatology. In the following figures, all grid points with data are plotted on maps, while only those with at least 5 MLD values are shown on scatter plots, in order to reduce the uncertainty associated with poorly sampled regions in the seal-derived data.

A comparison between MIMOC and MEOP-CTD MLDs in the Southern Ocean is shown in Fig. 2.1. As a reminder, MIMOC MLDs are computed thanks to the Holte and Talley (2009) algorithm. When comparing their algorithm outputs with the 0.03 kg m^{-3} density threshold method for Argo profiles (i.e. not under sea ice), they show that the latter slightly overestimates MLDs. We choose to compare the MIMOC climatology with MLD.01 from the MEOP-CTD data, since this stricter criterion appears better suited for the weakly stratified under-ice ocean in the Southern Hemisphere.

In Fig. 2.1a, a reasonable agreement between MIMOC and MEOP-CTD is obtained in the open ocean, while the MLDs are severely underestimated by MIMOC over continental shelves (how we define exactly these regions is explained in the next section). The slopes of the least squares linear fits shown in the figure and the correlation coefficients are, respectively, 0.93 and 0.62 in

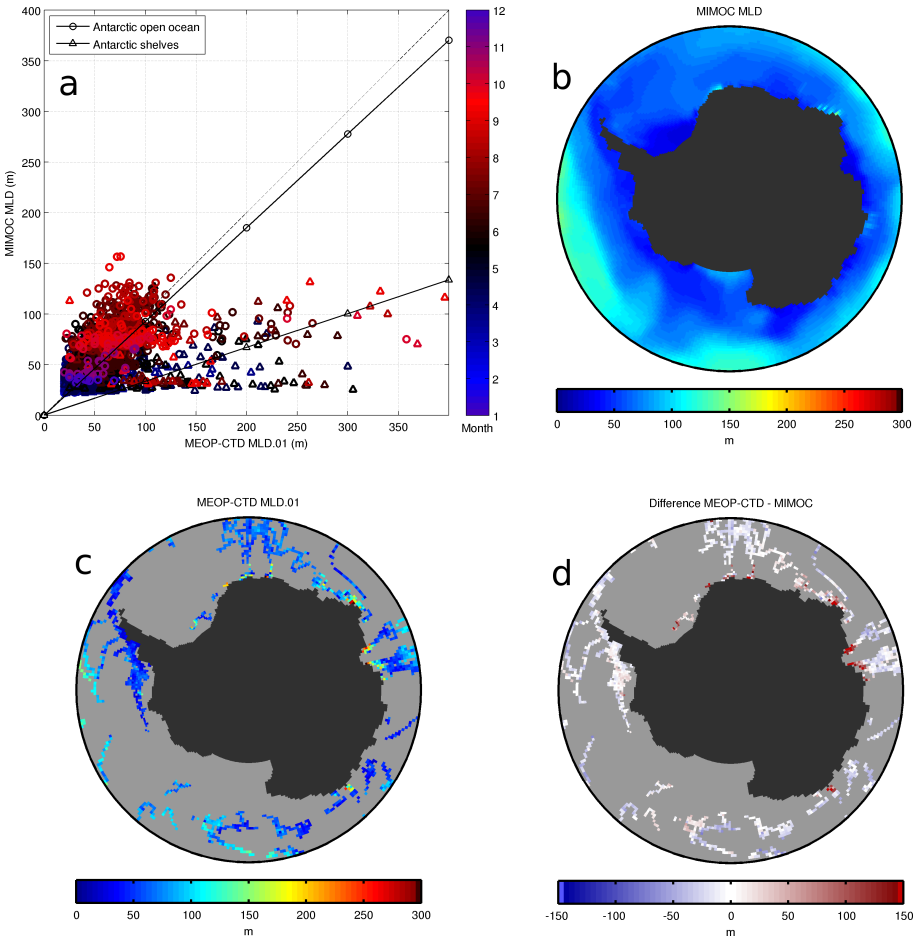

Figure 2.1: Comparison of MIMOC and MEOP-CTD MLDs. Scatter plot of MIMOC MLD versus MEOP-CTD MLD.01 (a), and maps of MIMOC MLD (b), MEOP-CTD MLD.01 (c) and their difference (MEOP-CTD - MIMOC, d) in May. In the scatter plot, a distinction is made between the points in the Antarctic open ocean and over the Antarctic shelves, solid lines are least squares linear fits and the dashed line is the diagonal.

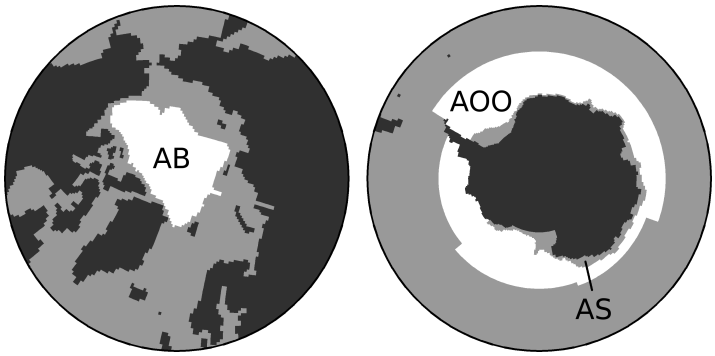

Figure 2.2: Selected areas for the results analysis: Arctic basin (AB), Antarctic open ocean (AOO) and Antarctic shelves (AS).

the open ocean, and 0.33 and 0.49 on the shelves. Maps are shown for May (Fig. 2.1b, c and d), as a compromise between deepening mixed layers and decreasing seal data coverage towards winter. They confirm that the errors between the two climatologies are generally smaller than 30 m away from the continent, but that MIMOC misses the deep MLDs along the coast of East Antarctica, by more than 150 m in several places. Note that this underestimation would have been even larger if we had used the MLD.03 criterion for MEOP-CTD, which would have yielded deeper mixed layers for this dataset.

2.4 Results and discussion

The NEMO-LIM3 response to the introduction of a brine rejection parameterization is now explored in both polar regions, as well as the model sensitivity to the choice of the vertical distribution depth. We examine model outputs averaged over the 1983-2013 period, except for the evaluation against the MEOP-CTD dataset, for which the 2004-2011 period is considered.

In what follows, some diagnostics are performed over three selected areas (Fig. 2.2). Large changes occur in the central part of the Arctic Ocean, hence we identify the "Arctic basin" (AB) as the region enclosed by the 500 m isobath and the 80°N parallel in Fram Strait (with a limited number of adjustments to avoid isolated grid cells). In the Antarctic, we distinguish between the "Antarctic open ocean" (AOO) and the "Antarctic shelves" (AS), based on the large differences in sea ice production rates and associated mixed layer regimes. The limit between both areas is normally the 1000 m isobath. However, the net ice growth over the Amundsen and Bellingshausen Seas shelves is much lower than in the Ross Sea for instance, implying shallower MLDs

(Petty et al., 2014). These shelf regions, along with the northern part of the Antarctic Peninsula, are excluded from AS. The northern limit of AOO is chosen as to ensure that the largest fraction of the area is covered with sea ice in winter.

In addition to the MLD.01 and MLD.03, the model also provides the turbocline depth (TCD). It is defined as the depth at which the vertical eddy diffusivity given by the TKE scheme falls below a given value, namely 5 cm/s^2. As a consequence, the turbocline is the actively mixing layer at the surface of the ocean, while MLD.01 and MLD.03 are only weakly stratified layers, i.e. mixed layers.

2.4.1 Arctic Ocean

The main impact of the BRP inclusion in the model is a dramatic reduction in mixed layer depths (except in late summer), clearly seen from their spatially-averaged seasonal cycles shown in Fig. 2.3a and b. The deeper the vertical salt distribution, the larger the effect. This result is not surprising and is in line with previous studies (Nguyen et al., 2009; Jin et al., 2012). In the absence of sea ice, upper-ocean mixing is caused by wind stirring and/or by surface heat losses. The presence of sea ice lessens the role of these processes, leaving negative buoyancy fluxes linked to brine rejection as the main reason for mixed layer deepening. This has been shown explicitly by Petty et al. (2014) for Antarctic continental shelves. The BRP not only suppresses this deepening mechanism, but also restratifies the mixed layer, since salt is distributed according to an increasing function of depth.

The comparison between the model results and the MIMOC climatology is not direct because of the various MLD definitions used. Without BRP, the different criteria in the model agree within 10 m at the winter maximum, and overestimate the MIMOC value by 10 to 25 m. Summer minima, on the other hand, are constantly underestimated. This latter bias, common in current climate models and possibly caused by a poor or missing representation of mixing processes like surface waves and Langmuir circulations (Huang et al., 2014), is beyond the scope of the present chapter. When the BRP is introduced, the gap widens between the MLDs obtained from the three criteria in the model. The TCD undergoes the largest decrease and becomes in all cases close to the minimum allowed model value (12 m). The MLD.03 is significantly affected only when the brine distribution depth is the MLD.03 itself. The MLD.01, which we consider the best characterization of the almost perfectly homogeneous modeled mixed layers, is excessively reduced compared to MIMOC, although the amplitude of the seasonal cycle fits the climatology better, in particular for experiment BRP.

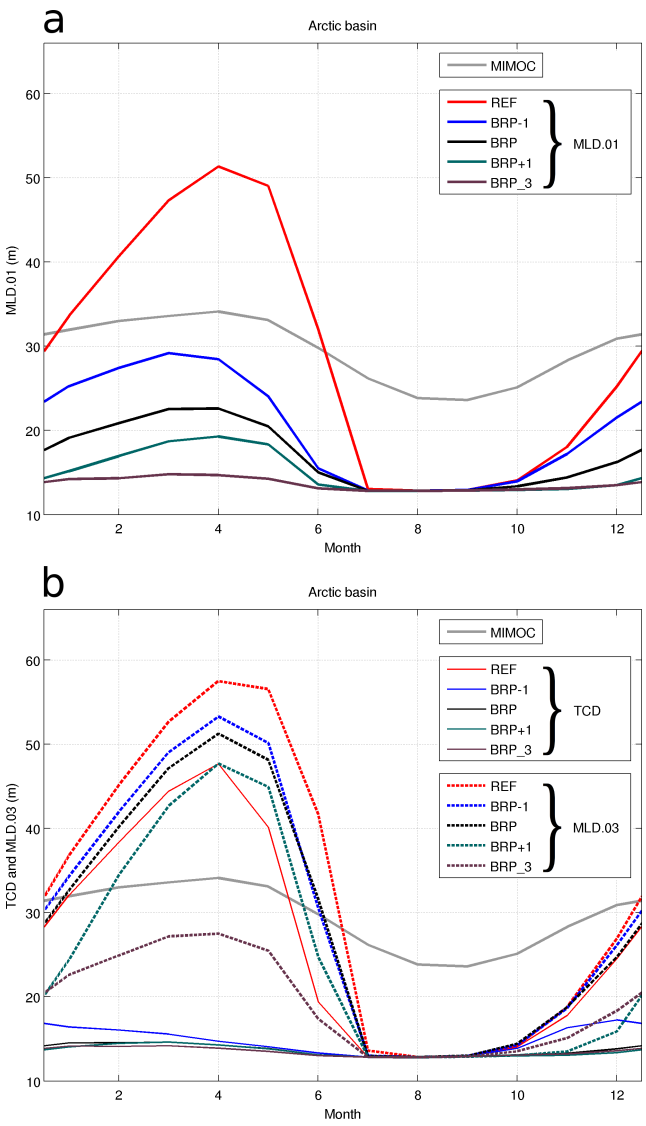

Figure 2.3: Seasonal cycles of mixed layer and turbocline depths, for the MIMOC climatology and model experiments, in the Arctic basin (a, b), Antarctic open ocean (c, d) and Antarctic shelves (e, f) areas. MLD.01s are shown as thick solid lines (top), and TCDs and MLD.03s as thin solid lines and as dashed lines, respectively (bottom). Following the discussion in Section 2.3, the MIMOC climatology is not plotted for the Antarctic shelves area.

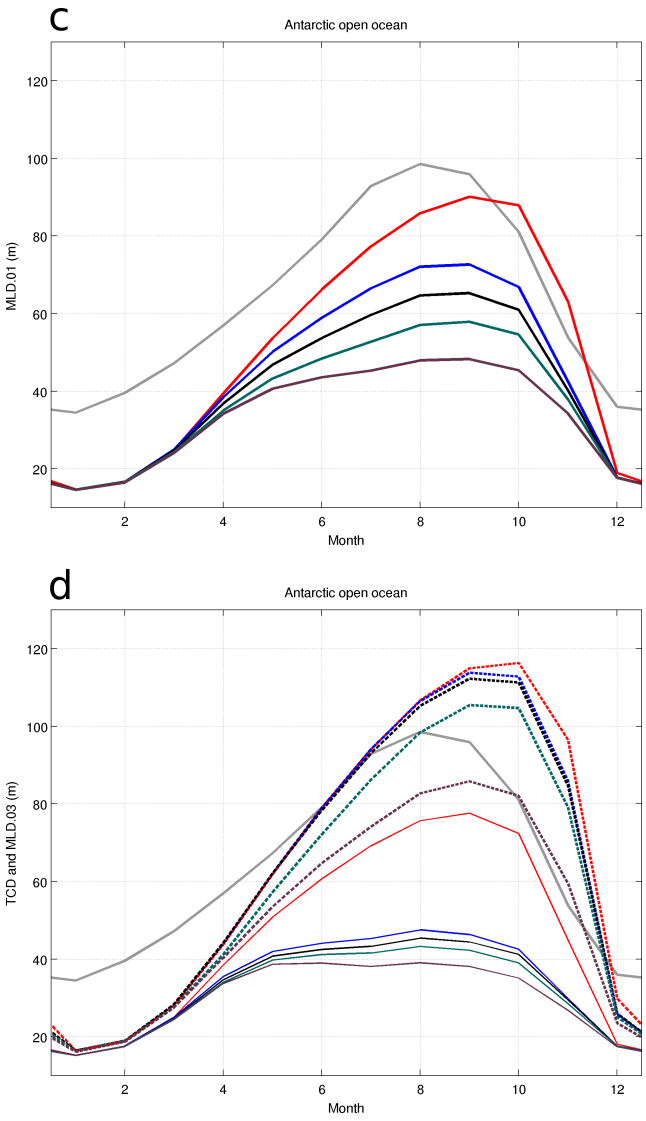

Figure 2.3: continued.

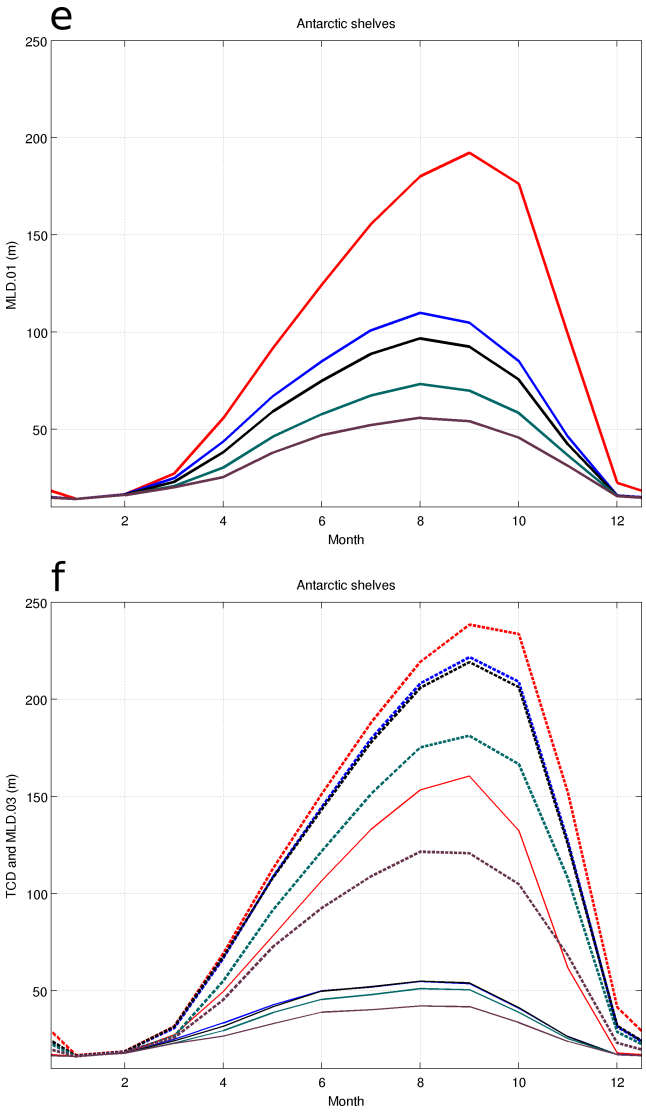

Figure 2.3: continued.

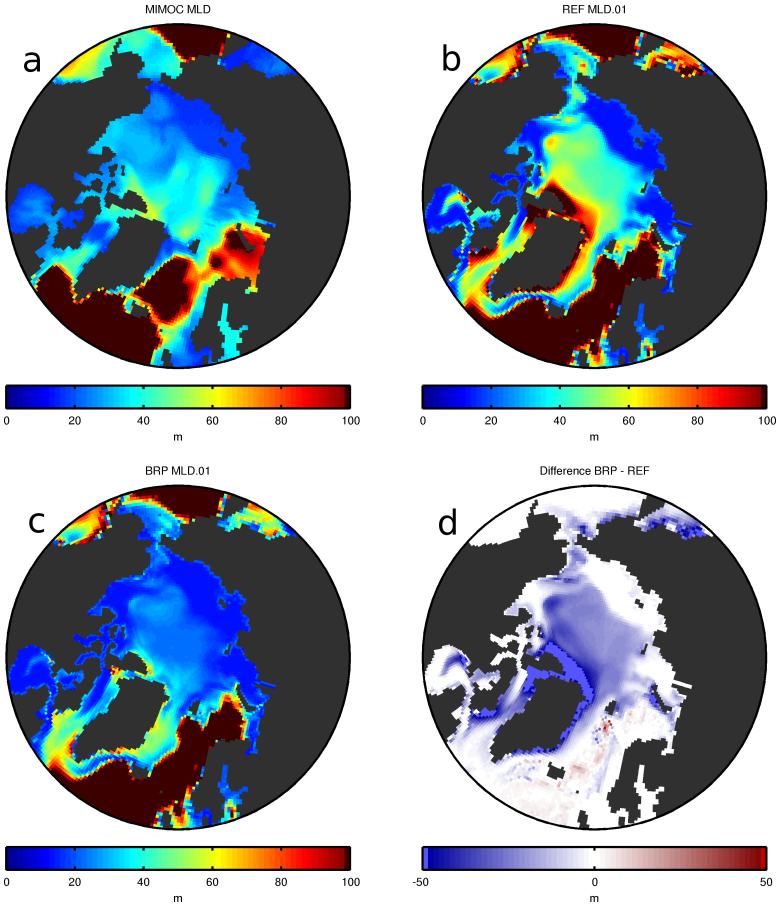

Figure 2.4: MIMOC MLDs (a, e) and model MLD.01s for experiments REF (b, f), BRP (c, g) and their difference (BRP - REF; d, h). Blue (red) areas in panels (d) and (h) correspond to shallower (deeper) mixed layers in BRP compared to REF. Maps are shown for March in the Northern Hemisphere and for September in the Southern Hemisphere.

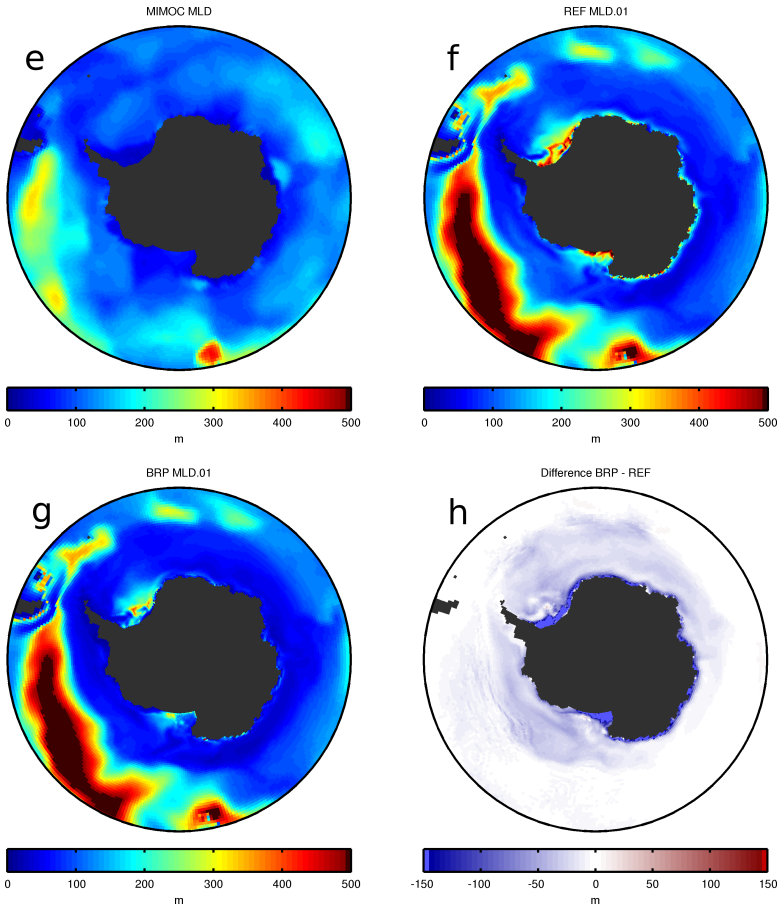

Figure 2.4: continued.

Maps of MLDs in March are shown in Fig. 2.4 for MIMOC and for MLD.01 in experiments REF and BRP. Mixed layers exceeding 100 m occur in REF around Greenland and in the east part of the Canadian Arctic Archipelago, as well as in the western Labrador Sea and the Hudson Bay, in stark contrast to observations. These biases compared to MIMOC are effectively reduced in BRP. Besides, the maps confirm the excessive MLD decrease in the Arctic basin shown in Fig. 2.3. On average, there is a switch from an overestimation of the order of 15 m in REF to an underestimation of around 10 m in BRP with respect to MIMOC.

The mean upper-ocean vertical temperature and salinity profiles in March are plotted for all experiments in Fig. 2.5a and d. As for MLDs, the BRP effect

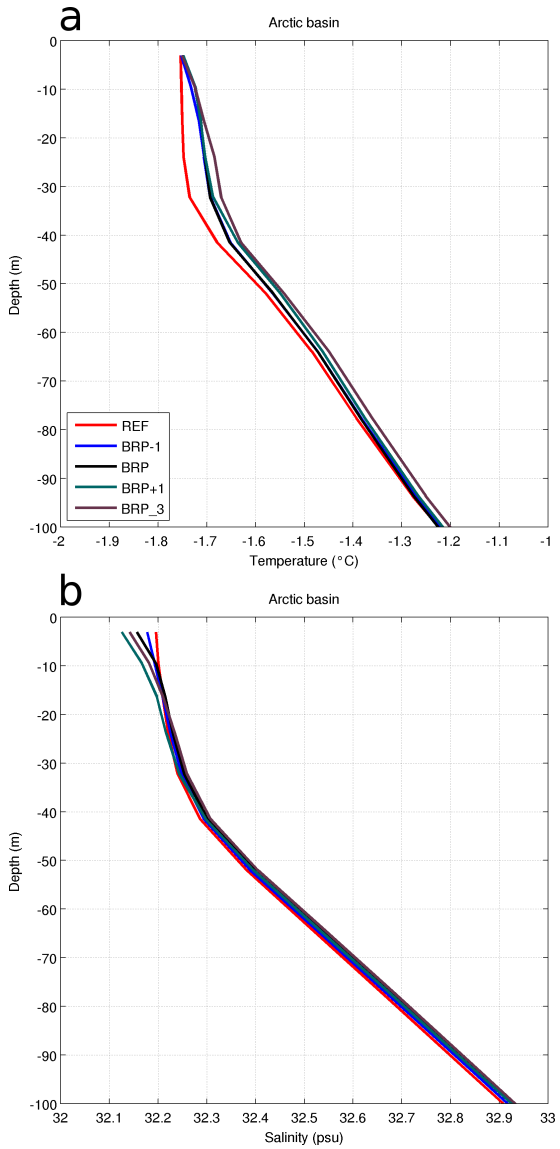

Figure 2.5: Mean model temperature and salinity profiles in the Arctic basin (a, b), Antarctic open ocean (c, d) and Antarctic shelves (e, f) areas, for March in the Northern Hemisphere and for September in the Southern Hemisphere.

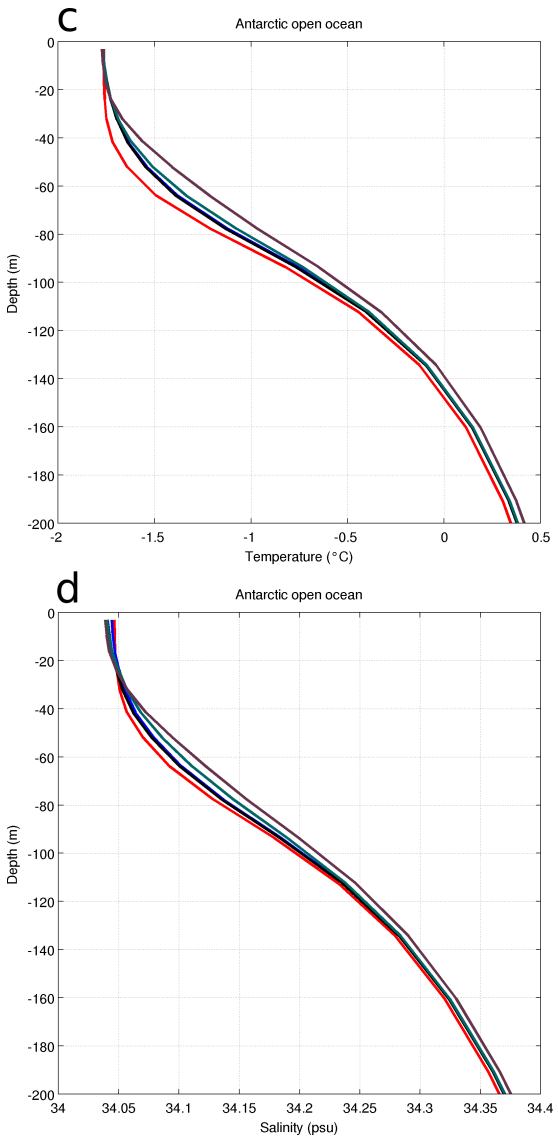

Figure 2.5: continued.

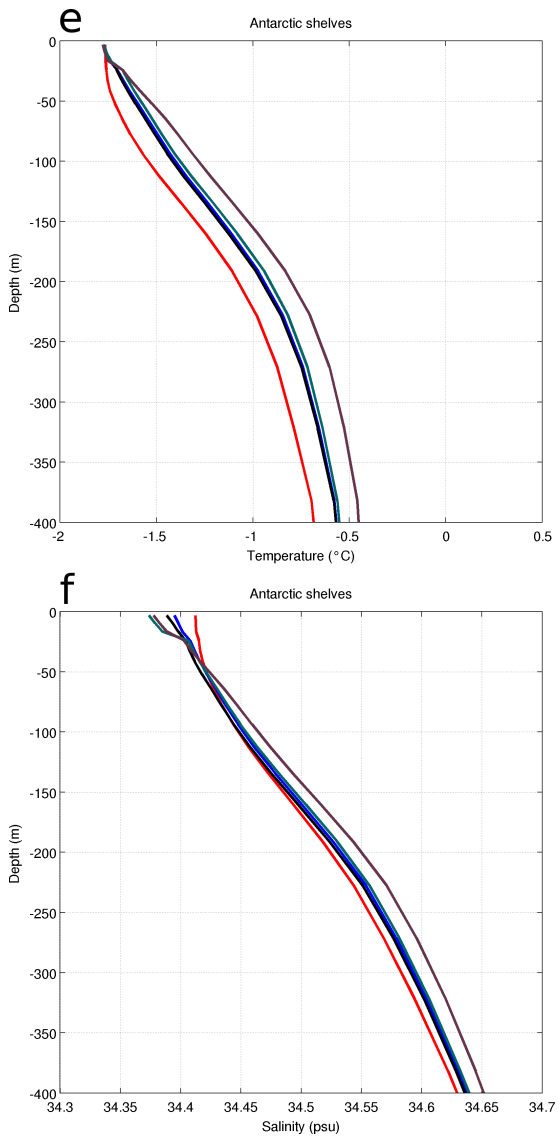

Figure 2.5: continued.

is larger when the maximum distribution depth is greater, but their overall shape remains largely unchanged, as would be a comparison with observed data. The sea surface salinity (SSS) decreases by less than 0.05 psu on average in the AB area in experiment BRP compared to REF. Salinity below 20 m tends to marginally increase when the BRP is activated, as expected from the design of the parameterization.

Sea surface temperature (SST) is forced to remain close to the freezing point due to the presence of sea ice, itself strongly constrained by the atmospheric forcing. In the subsurface, a warming of the water column is noted when the BRP is activated. This is explained by the weaker vertical mixing, which reduces the upward heat transfer in the ocean and therefore lowers the heat losses to the atmosphere active in autumn and winter. The warming is maximum between 15 and 30 m and vanishes below 100 m. On average in the upper 100 m, the temperature is 0.02 °C higher in BRP than in REF from autumn to spring. To a large extent, the difference persists in summer. The reason why changes remain limited is the near freezing temperatures characterizing the cold halocline in the Arctic Ocean, well visible in the upper 40 m of the mean profile in Fig. 2.5a but extending deeper in certain areas. Such a subsurface warming is also noticeable in the results of Nguyen et al. (2009).

As mentioned by Jin et al. (2012), the effects of the BRP on Arctic sea ice are weak. The parameterization slightly enhances the oceanic heat flux at the ice base, through a mechanism that will be described in more details for the Southern Ocean, where the signal is stronger. In the Arctic, given the prescribed atmospheric forcing used by the model, the change is too small to influence markedly the sea ice cover. The latter is indeed nearly identical in all experiments. Figures are shown for REF and BRP in Table 2.1.

Besides some similarities between our results and those of Nguyen et al. (2009) and Jin et al. (2012), two important differences are also noted. First, while the reductions in mixed layer thickness following the introduction of the BRP are of the same order of magnitude, neither of those studies concludes to an excessive MLD decrease. This is essentially due to their reference experiment having positive biases in MLD compared to observations that are clearly larger than ours. Second, the changes in vertical T/S profiles appear much smaller in our results. This difference in ocean response is at least partly explained by the higher background vertical diffusivity used in our model setup (1.2×10^{-5} m/s^2 against 1×10^{-6} m/s^2, see also Section 2.4.3).

2.4.2 Southern Ocean

In the REF experiment, one prominent feature of the under-ice winter mixed layer is the deep MLDs simulated in the Ross and Weddell Seas (Fig. 2.4f).

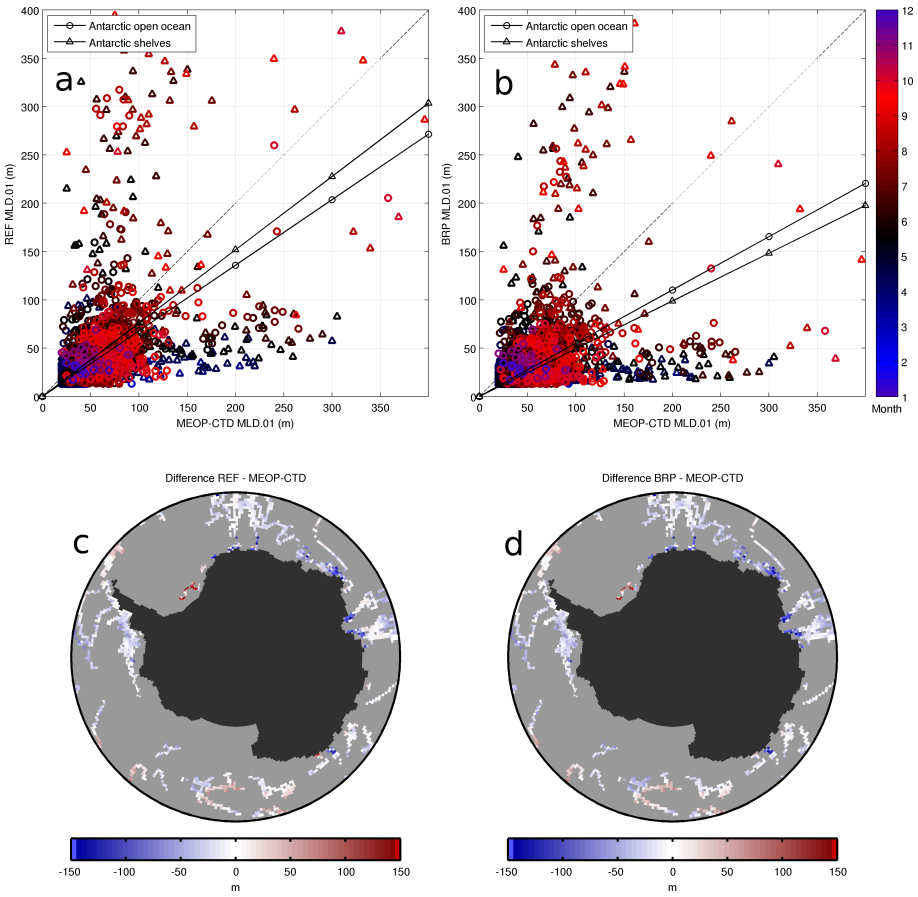

Figure 2.6: Comparison of MEOP-CTD and model MLDs. The MLD.01 is shown in all cases. Scatter plots of MEOP-CTD versus REF (a) and BRP (b) experiments, and maps of differences REF - MEOP-CTD (c) and BRP - MEOP-CTD (d) in May. In the scatter plots, a distinction is made between the points in the Antarctic open ocean and over the Antarctic shelves, solid lines are least squares linear fits and the dashed line is the diagonal.

These reach 500 m along the ice shelves, which implies the destratification of a significant fraction of the water column and the production of dense cold and saline waters over the continental shelves. MLDs close to and locally exceeding 200 m also occur along the coast of East Antarctica. Lower sea ice formation rates imply lower MLDs in the Amundsen and Bellingshausen Seas and around the northern tip of the Antarctic Peninsula. This MLD pattern is most similar with other recent modeling studies (Petty et al., 2014; Holland et al., 2014).

The agreement between model mixed layers and observations is relatively good in the Antarctic open ocean area. The spatially-averaged model MLD.01 winter maximum is less than 10 m smaller than the MIMOC value of 100 m, and it occurs one month later (Fig. 2.3c). This slight underestimation is confirmed by a comparison with the MEOP-CTD data (Fig. 2.6a and c). Over the Antarctic continental shelves, where we have shown that the MIMOC MLDs are unrealistic (Section 2.3), we consider only the seal-derived data. In this area, the mean model MLD.01 reaches as much as 190 m in September (Fig. 2.3e). Fig. 2.6a shows that it might still be underestimated on average compared to reality. The map for May in Fig. 2.6c indicates that too shallow MLDs occur along the coast of East Antarctica, but that the model mixed layer is too deep in the Weddell Sea. No data is available in the Ross Sea. Finally, the summer MLD problem is also present in the Southern Ocean, as well as a strong positive bias in MLDs in the ACC in the Pacific and Atlantic Oceans (Fig. 2.4e and f).

As in the Northern Hemisphere, including the BRP results in a significant mixed layer shallowing in ice-covered areas. Again, the effects are more pronounced for deeper brine distributions and for the turbocline depth (Fig. 2.3c to f). The maximum value of the average TCD is indeed less than 50 m in all experiments with the BRP, while it is not too different from MLD.01 in the reference experiment. In the Antarctic, MLD reductions are stronger in regions where much sea ice forms, reaching there often more than 150 m for MLD.01 (Fig. 2.4f, g and h).

Given the relatively good mixed layer representation in the ice-covered areas of the Southern Ocean in the REF experiment, the BRP inclusion degrades the model performance by yielding too shallow MLDs. The issue is especially clear over the continental shelves. The spatially-averaged MLD.01 in the AS region decreases by almost 100 m in September for experiment BRP (Fig. 2.3e). The reductions mostly occur in areas where the MLD was already underestimated in REF, whereas the simulation is only partly improved in the Weddell Sea (Fig. 2.6b and d). In AOO, for the same experiments, the MLD.01 diminishes by more than 20 m on average in September, leading to an under-

estimation of the seasonal cycle maximum by more than 30 m with respect to MIMOC. (Fig. 2.3c).

Consistently with the MLD changes, the BRP impacts on the mean vertical salinity and temperature profiles in September are larger in the AS area than in AOO (Fig. 2.5). The decrease in SSS is less than 0.01 psu in experiment BRP compared to REF in AOO, while it is 0.03 psu in AS. The increase in salinity in the subsurface between these two experiments reaches 0.01 psu at 60 m depth in AOO and the same value at 300 m in AS. The difference becomes much smaller in AOO below 200 m. The analysis of the mean response below 400 m depth in AS becomes gradually less significant due to the diminishing number of grid points participating in the average.

As in the Arctic, reduced vertical mixing in autumn and winter in simulations with the BRP induces a warming of the water column, except at the surface which remains at the freezing point. Changes are however larger due to the presence of warmer water below the surface layer in the Southern Ocean. The temperature is up to 0.1 °C higher in experiment BRP compared to REF at 60 m depth in AOO, while the difference is fairly constant at almost 0.15 °C in the upper 400 m in AS. These changes, originating in MLD differences in the winter season, are partly maintained in summer.

The link between sea ice-related surface processes and bottom ocean properties in the Antarctic has long been recognized (e.g., Goosse and Fichefet, 1999). Given the previous results, the inclusion of the BRP is expected to have an influence on the cold and saline waters present on the continental shelves around Antarctica. The bottom temperature indeed increases by more than 0.2 °C in the Weddell and Ross Seas and along the coast of East Antarctica, and the bottom salinity by up to 0.03 psu in the Ross Sea (not shown). These changes do not help reducing the model biases of deep ocean properties. The Antarctic Bottom Water body also becomes warmer and saltier in experiment BRP, but the length of our simulations does not allow us to be conclusive on this matter.

The ocean changes caused by the introduction of the BRP are sufficient to affect sea ice, through modifications of the oceanic heat flux at its base, in spite of the prescribed atmospheric forcing. Reducing the vertical mixing has two competing effects on this flux. On the one hand, less mixing tends to lower the upward heat transfer from the ocean subsurface to the ice, thus reducing the heat flux. On the other hand, smaller heat losses to the atmosphere in autumn and winter have been shown to increase the upper-ocean temperature. Yet, during winter, vertical mixing events, such as those induced by storms, are able to transfer heat from this layer to the sea ice base (Jackson et al., 2012; Zhang et al., 2013). This process is associated with a larger heat flux when the subsurface is warmer, as in BRP.

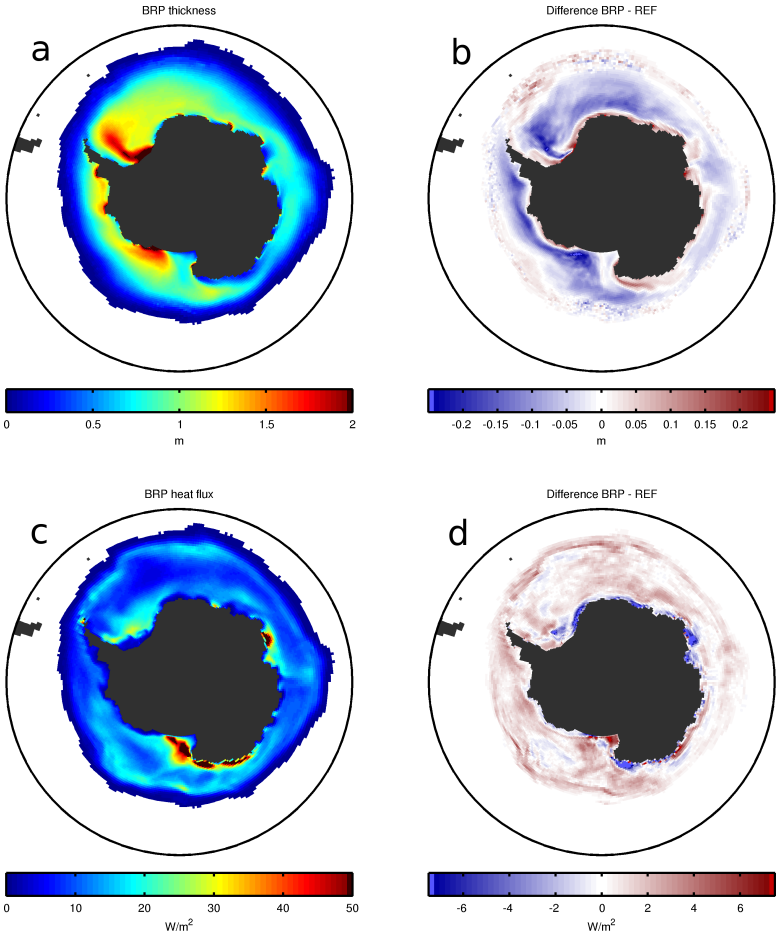

Figure 2.7: September sea ice thicknesses (a) and oceanic heat fluxes (c) in experiment BRP, and differences with experiment REF (BRP - REF; b, d). Red (blue) areas in panels (b) and (d) correspond to thicker (thinner) ice or higher (lower) heat flux in BRP.

Looking at the heat flux maps in September for experiment BRP and at differences with REF (Fig. 2.7c and d), we note that the first effect dominates in coastal areas undergoing intense heat flux in the reference experiment. Elsewhere, the second effect prevails, resulting in a higher heat flux when the BRP is included. The combined influence of these changes and of ice advection patterns explains the differences in sea ice thickness between experiments BRP and REF (Fig. 2.7a and b). For instance, the smaller heat fluxes encountered in the eastern Weddell Sea generate positive ice thickness anomalies that are transported along the Filchner-Ronne Ice Shelf and the Antarctic Peninsula by the cyclonic gyre existing in this region. Overall, sea ice is generally thicker along the coast, by up to 0.2 m, while it is thinner in the open ocean, mainly in the Pacific and Atlantic sectors, where the decrease reaches 0.2 m. Because thinner ice retreats further south in summer, and because the shallower mixed layer has a smaller inertia in winter, the seasonal cycle of ice extent is slightly stronger in experiment BRP, by 0.6×10^6 km^2 (Table 2.1). Nonetheless, for both the thickness and the extent, the changes are insufficient to correct the model errors compared to observations.

2.4.3 Limitations of the approach and simple refinement of the parameterization

Field and numerical studies have shown that the salt rejected during intense sea ice formation at the surface of a slowly moving lead mainly settles at the base of the mixed layer, instead of being incorporated uniformly within it (Smith and Morison, 1998; Morison and McPhee, 1998; Matsumura and Hasumi, 2008; Jin et al., 2012). As a consequence, the mixed layer is made shallower and more stratified. This provides a sound physical basis for the brine rejection parameterization proposed by Nguyen et al. (2009).

It may therefore appear surprising that the introduction of the BRP does not systematically provide a closer match between our model results and observations. In the Arctic, mixed layer depths are better simulated with a BRP only around Greenland and in the east part of the Canadian Arctic Archipelago, the western Labrador Sea and Hudson Bay. Anywhere else, namely inside the Arctic Ocean and in the Antarctic, MLDs are excessively reduced in simulations with a BRP compared to climatologies and hydrographic products. This is particularly obvious over the continental shelves around Antarctica.

Another feature of interest in the model results is the enhanced gap that appears when the BRP is activated between the MLDs computed from density threshold methods and the TCD. Under growing sea ice, vertical mixing in the upper ocean is mainly due to convection caused by negative buoyancy

fluxes linked to brine rejection. The BRP suppresses this effect, resulting in a very low vertical mixing. This is immediately reflected in the depth of the turbocline, the latter being by definition the layer of active mixing. By contrast, as defined in this study, the MLD decreases only if restratification takes place. The stratification visible close to the surface in vertical profiles in ice-covered regions (Fig. 2.5) is a sign of an extremely shallow mixing layer, but is too weak to diminish the MLDs as much as the TCD (Fig. 2.3). In a broader perspective, the lack of vertical mixing would be problematic if NEMO was coupled to a biogeochemical model. This would indeed impede vertical replenishment of nutrients and strongly alter surface biogeochemical cycles (e.g., Vancoppenolle et al., 2013; Smith et al., 2014).

Since the BRP can only reduce MLDs, whether the parameterization improves the comparison with observations actually depends on the model mean state. Consequently, an evaluation of the parameterization is inevitably linked to the biases present in the standard version of the model. We have already mentioned in Section 2.4.1 that poorly-represented or missing processes, among which surface waves and Langmuir circulations, could explain shortfalls in simulated vertical mixing in open waters during summer (Huang et al., 2014). The biases that we have pointed out in winter in simulations with a BRP could hence also originate in the absence or misrepresentation of such mixing sources. In particular, the NEMO TKE scheme includes parameterizations of near-inertial wave breaking and Langmuir turbulence, but they require further testing and development (Calvert and Siddorn, 2013; Rodgers et al., 2014), and potentially some adaptations in ice-covered oceans. Moreover, no submesoscale eddy parameterization is activated in our model configuration, although the primary impact would anyway be a shoaling of the mixed layer, especially in polar winter regions (Fox-Kemper et al., 2011).

The background vertical diffusivity is one key model parameter that could as well influence our conclusions. This diffusivity is used to account for unresolved and otherwise unparameterized mixing processes. Lowering its value has been shown to improve Arctic Ocean simulations, in models using both the turbulence k-profile parameterization (Zhang and Steele, 2007; Nguyen et al., 2009) or TKE mixing schemes (Komuro, 2014). As a test, the experiments REF and BRP have been repeated with a tenfold reduction of the background vertical diffusivity poleward of 60° N and of 60° S. The reference value (1.2×10^{-5} m/s^2) was maintained between 50° N and 50° S, with linear transitions between the different sectors. While results are barely affected in the Antarctic, the model mean state in the Arctic is indeed significantly impacted. Under-ice mixed layers shoal rather uniformly. As a result, the regions where the BRP improves the agreement with observations are more limited, and the

MLDs underestimation in other regions is more pronounced. The behavior of the parameterization itself is nonetheless unchanged.

In spite of the reservations expressed above about the attribution of biases to the BRP, it is doubtful that the parameterization can be applied in all conditions to all the salt rejected by sea ice. This simplification, also used in previous studies, totally suppresses the potential of brine rejections to deepen the mixed layer. With the BRP turned on, their effect becomes on the contrary to weakly restratify the mixed layer, which is unrealistic.

Firstly, although in the wintertime open waters undergo the highest heat losses to the atmosphere and hence the highest freezing rates (Maykut, 1978), only a fraction of the ice volume is formed in leads. The remaining fraction is produced at much larger horizontal scales, in particular by bottom accretion below the existing ice cover. As noted by Jin et al. (2012), the BRP becomes unnecessary for such widespread salt input at the ocean surface, for which the model vertical mixing scheme is likely to work properly. Identifying the part of the brine that is rejected in a localized manner and has to be handled with the BRP is, however, not easy. Using the BRP only for the salt rejected in the open water fraction of the grid cell barely changes the model results compared to the reference experiment (not shown). This is because openings within the sea ice cover refreeze quickly, making the open water fraction and the associated sea ice production very low.

Secondly, studies based on field observations and on model results have shown that ice-water relative velocities higher than 5 cm s^{-1} prevent the formation of salt plumes (Morison et al., 1992; Smith and Morison, 1993; Muench et al., 1995; Kantha, 1995; Skyllingstad and Denbo, 2001). In that case, mixing generated by shear turbulence dominates convective mixing. Additionally, since the lead is moving, the brine is spread out at the ocean surface. The rejected salt simply mixes into the mixed layer and the application of a BRP is not appropriate. This might explain why results are not as problematic in the Arctic as below the faster-moving Antarctic sea ice.

Finally, it is not clear whether the BRP is valid for the very deep MLDs encountered over the Southern Ocean continental shelves. Although these parameterizations were at first developed for the Antarctic (Duffy and Caldeira, 1997; Duffy et al., 1999), it would be surprising that salt plumes generated by narrow leads reach the mixed layer base situated several hundred meters below the surface. Other types of convection schemes have been proposed to address specifically the problem of deep convection (Kim and Stössel, 2001). Applying such methods might yield better results than the BRP tested here in deep mixed layer areas.

Among the three issues raised above, testing a parameterization including a dependency on the ice-ocean relative velocity appears to be the most

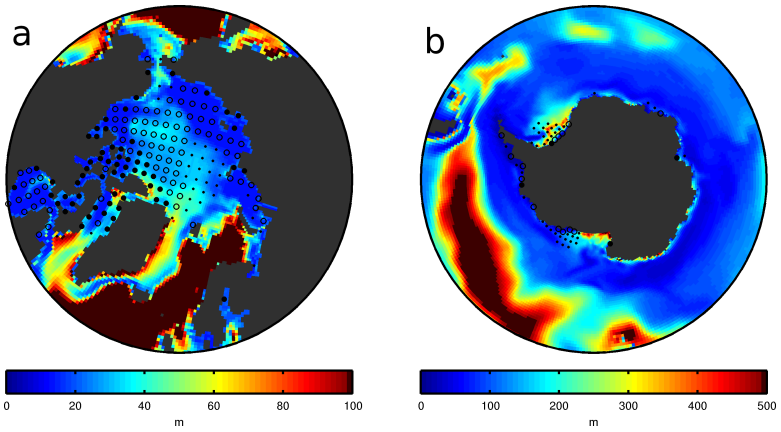

Figure 2.8: MLD.01s in model experiment BRPv, for March in the Arctic (a) and for September in the Antarctic (b). Large dots, empty circles and small dots indicate areas where the BRP applies to 100 %, more than 50 % and less than 50 % of the salt rejected by sea ice, respectively. The BRP is not applied in areas without symbols.

straightforward and instructive. Accordingly, an additional experiment called BRPv is performed, corresponding to the simulation BRP with the parameterization only active for low velocities. In practice, the instantaneous ice-ocean relative velocity is used to compute the fraction of the rejected salt that is handled with the BRP. This fraction is 1 below 2.5 cm/s and 0 above 7.5 cm/s, and increases linearly between these two values. The remaining salt fraction is rejected in the top ocean layer. Results are shown in Fig. 2.8.

In the Arctic, the parameterization is applied in the same way as in the BRP experiment in and north of the Canadian Arctic Archipelago, in Baffin Bay and in sparse coastal sectors. Besides, between 50 % and 100 % of the rejected salt is distributed vertically in most of the Arctic Ocean, where it allows to recover MLDs that are closer to the MIMOC climatology. On average in the AB area, the winter maximum of MLD.01 is still underestimated by 5 m in BRPv with respect to MIMOC (not shown). The BRP finally does not apply east of Greenland and in the Labrador Sea, where the model biases present in the reference simulation therefore reappear. In the Antarctic, the BRP is only applied in very limited coastal areas, and to less than 50 % of the rejected salt in parts of the Weddell and Ross Seas. As a consequence, MLDs are much less reduced in BRPv than in BRP, the best match with observations being nevertheless still provided by REF.

Although this simple refinement of the BRP improves the simulated MLDs, it also brings new significant sources of uncertainty. In particular, a proper be-

havior of the parameterization relies on a correct representation of both the sea ice circulation and the ocean surface currents. Furthermore, the choice of the velocity thresholds used to separate the different mixing regimes is rather arbitrary. They could be considered as ad hoc model tuning parameters.

2.5 Conclusions

In this study, a brine rejection parameterization has been introduced in the global ocean-sea ice model NEMO-LIM3. The aim of this parameterization is to mimic the effects of small-scale convection associated with intense brine rejections in leads in winter, and to avoid excessive grid-scale mixing. The basic principle is to distribute the salt rejected by sea ice according to a power-law profile within the mixed layer, a greater fraction being deposited at its base than at the surface. Model results were validated against two recently published products, namely a mixed layer depth climatology and a hydrographic dataset derived from seal-borne CTD sensors.

The main effect of the parameterization is to reduce significantly the mixed layer depth in ice-covered areas. Salinity decreases at the surface and marginally increases in the subsurface. Less heat is lost to the atmosphere in autumn and winter, due to the reduced vertical mixing, inducing an increase in upper-ocean temperature. In the Antarctic, the oceanic changes are large enough as to impact the sea ice thickness, although the atmospheric forcing is prescribed.

While mixed layer depths are locally in the Northern Hemisphere in better agreement with observational estimates, the reduction in surface mixing is in general too strong, hence degrading model results in most regions. Uncertainties in the comparison to observations and inaccuracies in the representation of other mixing processes prevent a definitive attribution of these biases to the brine rejection parameterization itself. However, in the way it is first applied here, all brine rejections from sea ice are unrealistically turned into a process which restratifies the mixed layer, without any deepening effect left.

In reality, salt plumes are likely to occur only for low ice-ocean relative velocities, otherwise shear-driven mixing is dominant over convection caused by a moving brine source, and for the salt rejected in a localized manner, which is not easy to identify in a model. Including a dependency on the relative velocities has been tested and shown to yield clear improvements in the simulated mixed layer depths. Yet, this comes at the price of introducing new poorly constrained parameters in the design of the parameterization. A more explicit approach is possible and promising. Following Holland (2003), the ice-ocean fluxes can be differentiated at the subgrid-scale across sea ice cate-

gories and open water, and the oceanic conditions and mixing regimes below each category can be represented. This is the subject of the next chapters.

CHAPTER 3

SPATIAL HETEROGENEITY OF OCEAN SURFACE BOUNDARY CONDITIONS UNDER SEA ICE

Abstract

The high heterogeneity of sea ice properties implies that its effects on the ocean are spatially variable at horizontal scales as small as a few meters. Previous studies have shown that taking this variability into account in models could be required to simulate adequately mixed layer processes and the upper ocean temperature and salinity structures. Although many advanced sea ice models include a subgrid-scale ice thickness distribution, potentially providing heterogeneous surface boundary conditions, the information is lost in the coupling with a unique ocean grid cell underneath. The present chapter provides a thorough examination of boundary conditions at the ocean surface in the NEMO-LIM model, which can be used as a guideline for studies implementing subgrid-scale ocean vertical mixing schemes. Freshwater, salt, solar heat and non-solar heat fluxes are examined, as well as the module of the surface stress. All of the thermohaline fluxes vary considerably between the open water and ice fractions of grid cells. To a lesser extent, this is also the case for the surface stress. Moreover, the salt fluxes in both hemispheres and the solar heat fluxes in the

Arctic show a dependence on the ice thickness category, with more intense fluxes for thinner ice, which promotes further subgrid-scale heterogeneity. Our analysis also points out biases in the simulated open water fraction and in the ice thickness distribution, which should be investigated in more details in order to ensure that the latter is used to the best advantage.

3.1 Introduction

The presence of sea ice at the polar oceans surface has numerous impacts on their upper layer physics and biogeochemistry. Its high albedo compared to seawater strongly reduces the amount of absorbed solar radiation, giving rise to the well-known positive ice-albedo feedback (Curry et al., 1995). It constitutes an efficient barrier for mass exchanges between the atmosphere and the sea surface, inhibiting evaporation and preventing at least a fraction of precipitation from entering the ocean at the time when it falls. Owing to its low thermal conductivity (Pringle et al., 2007), sea ice dampens the oceanic heat losses to the atmosphere in winter. Because its salinity is lower than that of the sea surface, and because it is transported by winds and currents, its formation and melt are associated with buoyancy fluxes that influence the upper ocean stratification, convective processes and eventually the global thermohaline circulation (e.g., Goosse and Fichefet, 1999). A compact sea ice cover prevents the formation of waves and direct wind-generated turbulence in the water column, but its relative motion with respect to the water is a source of stress at the ocean surface. From a biogeochemical point of view, sea ice modulates the gas exchanges at the atmosphere-ice-ocean interface, provides a support for microbiological activity and chemistry, and acts to concentrate, transport or release nutrients and substances like inorganic carbon (Vancoppenolle et al., 2013).

The sea ice cover is a fundamentally heterogeneous medium. During summer, large open water areas can exist between the melting floes. A few percent of the sea surface remain free of ice even at the core of the winter season, in the form either of linear openings caused by divergence of the pack, known as leads, or of polynyas created by strong winds or high oceanic heat supply. The ice itself is a mixture of components ranging from thin new ice formed in open water areas to ridges several meters thick resulting from deformation inside the pack (Thorndike et al., 1975). While the most substantial differences in surface conditions occur between ice-covered and ice-free areas, several of the processes listed above also depend on the sea ice type, thickness and surface state. As these vary significantly on small horizontal scales, so do their effects on the underlying ocean and the atmosphere above.

It has long been recognized important to represent the subgrid-scale heterogeneity of ice thickness in order to accurately simulate the sea ice evolution (Thorndike et al., 1975; Hibler, 1980). As a consequence, ice thickness distributions are included in most advanced models nowadays, among which CICE (Los Alamos Sea Ice Model, Hunke et al., 2015) and PIOMAS (Pan-Arctic Ice-Ocean Modeling and Assimilation System, Zhang and Rothrock, 2003). It allows them to compute the open water fraction and the concentration of ice

of various thicknesses based on thermodynamic and dynamic processes. The implementation details and the impacts on model results are likewise intensively studied (e.g., Massonnet et al., 2011; Komuro and Suzuki, 2013; Castro-Morales et al., 2014; Hunke, 2014). However, the spatial heterogeneity in ocean surface boundary conditions implied by this variability in ice properties has been so far overlooked. This is explained by the fact that the various ice thickness categories have to exchange information with a unique ocean grid cell underneath, which requires the fluxes to be aggregated into single values.

Previous studies have nonetheless shown that taking the surface conditions heterogeneity into account is necessary in order to adequately simulate the ocean physics below sea ice. By comparing vertical mixing parameterizations commonly used in coarse resolution large-scale models with large eddy simulations, Losch et al. (2006) have demonstrated that neglecting the heterogeneous nature of buoyancy fluxes associated with a partial ice cover leads to biases in the mixed layer depth and the upper ocean density structure. Brine rejection parameterizations have for instance been developed to represent the impacts of intense convective mixing in winter leads (e.g., Duffy and Caldeira, 1997; Nguyen et al., 2009, Chapter 2). Further studies have implemented explicit separate vertical mixing computations in fractions of individual grid cells corresponding to ice and to open water (Holland, 2003; Jin et al., 2015).

Nevertheless, a detailed description of the heterogeneous ocean surface boundary conditions under sea ice is still missing, to our knowledge. The objective of the present chapter is therefore to fill in this gap. In addition to leading to a better understanding of the spatial distribution of sea ice-ocean interactions, this will be of great interest to help interpreting the results of the above-mentioned studies. It will as well constitute the basis for a further analysis of subgrid-scale mixing below sea ice (Chapter 4). Under-ice observations are still far too sparse to allow examining under-ice fluxes at large scale and in all seasons. Our study will hence make use of the global ocean-sea ice model NEMO-LIM, whose ice component includes a state-of-the-art ice thickness distribution and in which the subgrid-scale heterogeneity of all fluxes and of the stress provided at the ocean surface will be thoroughly investigated.

This chapter is organized as follows. The NEMO-LIM model setup is described in Section 3.2, with a particular emphasis on the ocean surface boundary condition aspects. The modeled mean sea ice state and ice thickness distribution are documented in Section 3.3, because they constitute the background for the simulation of heterogeneous boundary conditions. The latter are presented and discussed in Section 3.4. A summary of our findings is finally given in Section 3.5.

3.2 Model setup

3.2.1 Ocean-sea ice model NEMO-LIM

The ocean component of NEMO (Nucleus for European Modelling of the Ocean) is a finite difference, hydrostatic, free surface, primitive equation model fully described in Madec (2008). The ocean model's version 3.5 is coupled to the latest revision of the dynamic-thermodynamic sea ice model LIM (Louvain-la-Neuve sea Ice Model), known as LIM3.5 (Vancoppenolle et al., 2009b; Rousset et al., 2015). LIM includes an ice thickness distribution (ITD), which allows to represent the subgrid-scale heterogeneity of ice thickness, enthalpy and salinity. The model configuration is very close to the one used in Chapter 2. Three noticeable differences are listed hereafter, along with details about the ocean surface boundary conditions (SBCs) and the experimental design.

First, compared to Chapter 2, we use a slightly updated version of LIM, in which several minor heat conservation leaks have been fixed (Rousset et al., 2015).

Second, the background diffusivity in the so-called TKE vertical mixing scheme (for turbulent kinetic energy, Blanke and Delecluse, 1993; Madec, 2008) has been lowered in the polar regions, following studies showing that it improves Arctic Ocean simulations (Zhang and Steele, 2007; Nguyen et al., 2009; Komuro, 2014). In practice, a tenfold reduction of the background vertical diffusivity poleward of 60° N and of 60° S is implemented, whereas the reference value (1.2×10^{-5} m/s^2) is maintained between 50° N and 50° S. The transitions between the different sectors are linear. Results are mostly unaffected in the Antarctic, but simulated mixed layer depths (MLDs) in the Arctic Ocean are reduced, leading to a better agreement with observations (Chapter 2).

Third, two artificial connections present in the standard version of LIM between the ice-free and ice-covered fractions of grid cells have been removed. Previously, ice was allowed to grow in the ice-free part of a grid cell only if the surface heat loss was large enough as to cool the entire top oceanic cell down to the freezing point. On the other hand, in the melting season, positive surface heat fluxes in open water were not used to increase the temperature of ocean cells in which ice was still present, but were rather transferred to the sea ice base. These two processes provided an instantaneous link between the ice-free and ice-covered parts of grid cells, and complicated the interpretation of ocean surface fluxes in open water and below ice. Their removal leads to smaller open water fractions in winter, but the combined effect on sea ice thickness is weak. The code has been modified so that ice can grow in the ice-free fraction of a grid cell as soon as the heat loss is sufficient to lower

the temperature of the corresponding cell fraction to the freezing point, and positive heat fluxes in open water simply increase the sea surface temperature (SST).

In virtually all large-scale applications so far, the ITD in LIM has been used with five ice thickness categories. The surface of each grid cell is thus separated into six parts. The first one is the ice-free fraction, representing open water and leads within the sea ice cover, and the remaining five correspond to the ice thickness classes, each one having its own concentration. The upper thickness limits for the first four categories are 0.63 m, 1.33 m, 2.25 m and 3.84 m, while the fifth is unbounded. Transfers between the different categories are caused by thermodynamic growth or melt and by the deformation processes that the model accounts for, namely ridging and rafting (Vancoppenolle et al., 2009b).

3.2.2 Ocean surface boundary conditions

Our aim here is examining the subgrid-scale heterogeneity of ocean SBCs associated with the ITD present in LIM. To this end, the surface thermohaline fluxes and the module of the surface stress have been diagnosed separately for the six fractions of each grid cell. On the one hand, the thermohaline fluxes are the main drivers of SST and sea surface salinity (SSS) variations, and hence of buoyancy changes at the ocean surface. We will look at the freshwater, salt and heat fluxes, the latter being further split into its solar and non-solar components. By convention, a positive flux is directed towards the ocean. The surface stress is, on the other hand, driving turbulent mixing at the ocean surface. In the TKE vertical mixing scheme used in our NEMO configuration, its module sets the surface boundary condition on turbulent kinetic energy (Madec, 2008). The SBCs also have effects on upper ocean currents, but the impact of their heterogeneity is more complex and not discussed here.

It is important to mention that these subgrid-scale fluxes and stress are merely diagnostics in this study. They are still aggregated across the six grid cell fractions before being transmitted to the ocean model. All model features detailed in this section are from Vancoppenolle et al. (2009b) and Rousset et al. (2015) for the sea ice and from Madec (2008) for the ocean.

3.2.2.1 Freshwater and salt fluxes

To understand how freshwater fluxes affect the SSS in the model, it is worth noting that our setup uses NEMO in its linear free surface formulation, with a filtering term in the momentum equation to dampen the fast external gravity waves (Roullet and Madec, 2000). This approach allows taking into account

the mass flux due to freshwater input at the ocean surface in the momentum equation. However, the linearization implies that the ocean volume is fixed in time and that the thickness of the first ocean layer in particular is constant. Consequently, the salinity concentration or dilution effect associated with negative or positive (according to the convention chosen above) freshwater fluxes F_{fw} is achieved by turning them into virtual, or equivalent, salt fluxes $F_{s,v}$ following:

$$F_{s,v} = -F_{fw} S_{ss},$$

where S_{ss} is the sea surface salinity. By comparison, in a non-linear free surface context with variable volumes, such a virtual salt flux would not be necessary. In that case, the thickness of the first ocean layer would adjust to the freshwater flux and the SSS change would arise from the concentration or dilution of its unchanged salt content.

Freshwater fluxes in open water include evaporation and solid precipitation. A fraction f_0^β of all solid precipitation, with $\beta = 0.6$, reaches the open water area f_0, because winds blow some snow off the sea ice surface. In the rare cases when the air temperature is high enough to allow liquid precipitation over sea ice, these are supposed to percolate through the ice and reach the oceanic grid cell surface uniformly. Concentrating liquid precipitation in open water, in an attempt to mimic runoff from the ice, would indeed result in extremely large freshwater fluxes when the ice-free area is small. Moreover, a SSS restoring towards the PHC3 climatology (Polar Science Center Hydrographic Climatology, Steele et al., 2001) is implemented as a damping term in the surface freshwater budget, with a 310 days time scale for a 50 m mixed layer. This term is likewise spread out uniformly at the surface. It is furthermore multiplied by the open water fraction f_0, meaning that its magnitude is reduced under sea ice, as in Chapter 2. Finally, although continental runoffs are taken into account in the model, they are not included in the freshwater fluxes examined here.

Since the pressure effect of sea ice is not included in our model configuration, the formulation of ice-related processes implies small errors on the ocean dynamics, but their consideration is beyond the scope of the present study (e.g., Schmidt et al., 2004). As a concrete example of freshwater and salt exchanges between the ice and the ocean, the formation of sea ice at salinity S_i is associated in reality with a negative freshwater flux F^i_{fw} (out of the ocean) and with a real salt flux $F^i_{s,r}$ given by:

$$F^i_{s,r} = F^i_{fw} S_i.$$

This flux is also negative, meaning that a relatively weak amount of salt is extracted from the ocean to be stored in the sea ice. The observed increase in SSS following sea ice formation is due to the concurrent freshwater output, whose concentration effect is included, as above, by means of a virtual salt flux in the model. The total flux used to compute the SSS evolution is then:

$$F_s^i = F_{s,r}^i + F_{s,v}^i = F_{fw}^i (S_i - S_{ss})$$

and is indeed positive for sea ice formation, since $F_{fw}^i < 0$ and $S_i < S_{ss}$. Bottom growth, bottom melt, surface melt, snow-ice formation and formation of new ice in open water are handled with such a combination of real and virtual salt fluxes. The fluxes from each category and from open water are readily attributed to the corresponding grid cell fractions.

Three additional sea ice and snow processes affect freshwater and salt fluxes below each ice category. Firstly, the advanced halodynamics scheme included in LIM allows a representation of brine entrapment and drainage, and makes the sea ice salinity variable both in space and time. The rejection of brine through gravity drainage and flushing is treated as pure, real salt fluxes which are specific to each ice category. Secondly, the melt of snow accumulated on sea ice induces a pure freshwater flux to the ocean, distinct for each category. It is thus handled as a virtual salt flux in the computation of SSS. At last, ridges simulated in LIM are assumed to have a porosity of 0.3. The entrapped water volume is turned into ice with salinity $S_i = S_{ss}$, i.e. there is no immediate brine rejection. The corresponding F_s^i is zero, showing that the formation of porous ridges has no direct impact on the SSS. Subsequent brine drainage occurs nonetheless and lowers the ridges salinity.

What we refer to as salt flux in the following sections is actually the combination of both real and virtual components, the latter accounting for the effects of freshwater fluxes, which therefore do not need to be examined separately.

3.2.2.2 Heat fluxes

The solar radiation reaching the ocean surface is strongly reduced under sea ice. The high ice albedo, which in the model depends on the state of the surface, the ice thickness, the snow depth and the cloudiness, implies that a large fraction of the radiation is reflected back to the atmosphere. The remaining solar flux is totally absorbed by snow, if present. Without snow, the upper ice layer absorbs a fraction of the net surface radiation, while the rest is transmitted through the ice, where it attenuates exponentially with an attenuation length equal to 1 m. The solar heat flux considered here is the amount of energy per unit time and area that eventually reaches the ice-ocean interface. It

can vary significantly from one sea ice category to another, since they have different snow covers and, by definition, different thicknesses. Inside the ocean, as parameterized in the model, 42 % of the surface flux, associated to wavelengths for which seawater is more transparent, penetrate the top few tens of meters with a decreasing exponential profile and contribute to local heating. Because of a much shorter depth of extinction, the remaining 58 % are absorbed in the first few meters.

The constituents of the non-solar heat flux at the ocean surface are very distinct under sea ice and in the open water. Under ice, the major contribution is the sensible heat flux from the ocean to the ice F_w. Following McPhee (1992), it is taken to be proportional to the difference between the sea surface temperature T_{ss} and the ice base temperature, corresponding to the freezing point T_{fr} at the local salinity. It is also related to the module of the ice-ocean relative velocity through the friction velocity u^*_{io}, whose lower bound is fixed here at 5×10^{-3} m s^{-1}. We have:

$$F_w = \rho_w c_w c_h u^*_{io} (T_{ss} - T_{fr})$$

where ρ_w is the reference seawater density, c_w the specific heat of seawater and c_h a heat transfer coefficient equal to 0.0057. Positive heat flux to the ice F_w are negative contributions to the non-solar heat flux, with our convention. They are identical for all ice categories, since the SST and SSS (hence T_{fr}) are unique within one grid cell. The non-solar heat flux at the ice-ocean interface also includes smaller terms originating from mass exchanges at temperatures different from the SST, for instance from ice or snow melt, which can vary from one category to another.

In the open water fraction of grid cells, the non-solar heat flux is made up of the atmosphere-ocean longwave, sensible and latent heat fluxes, which are computed from the classical CLIO bulk formulas described by Goosse (1997). Smaller contributions come from the sensible heat of precipitation and from the latent heat of solid precipitation. In conditions of sea ice formation, a fraction of the non-solar flux is used to erode the ocean heat content and lower the SST to the freezing point, while the remaining is compensated by the latent heat released by seawater freezing. The first component can be non-negligible in case oceanic heat is supplied from the subsurface (Haid and Timmermann, 2013). The second component does not lead to SST variations, and its effects on the water column stability are through salt fluxes associated with ice formation. In the following, we consider the first component only and refer to it simply as the non-solar heat flux, although it might not be its usual definition.

3.2.2.3 Surface stresses

Both the atmosphere-ocean and the ice-ocean stresses derive from quadratic bulk formulas. The drag coefficients are 1×10^{-3} and 3×10^{-3}, respectively. The module of the ice-ocean stress is the same for all categories, since the drag coefficient is taken as a constant. More recent parameterizations allow this coefficient to be dependent on the sea ice state and therefore to evolve spatially and temporally (Tsamados et al., 2014), and could be of interest to refine the ice-ocean momentum exchange.

3.2.3 Experimental design

The model simulation is designed as follows. The initial temperature and salinity fields are taken from the World Ocean Atlas 2001 (Conkright et al., 2002), and the ocean-sea ice model is run from January 1948 until December 2014. Atmospheric forcing fields consist of a combination of NCEP/NCAR daily reanalysis data of surface air temperature and wind speed (Kalnay et al., 1996) with monthly climatologies of relative humidity (Trenberth et al., 1989), cloudiness (Berliand and Strokina, 1980) and precipitation (Large and Yeager, 2004). Continental runoff rates are prescribed from the climatological dataset of Dai and Trenberth (2002). Heat fluxes at the atmosphere-ice and atmosphere-ocean interfaces are parameterized as in Goosse (1997).

The ocean and sea ice models run over a common domain extending from 78° S to 90° N. This domain is discretized on the quasi-isotropic global tripolar grid ORCA1, based on the semi-analytical method of Madec and Imbard (1996), which has 1° resolution in the zonal direction. A z coordinate is used on the vertical. The surface layer is 6 m thick. The thickness of the 46 layers increases non-uniformly with depth, reaching 20 m at 100 m depth and 250 m for the bottommost layer. The ocean model has a time step of 1 h and LIM is called every six ocean time steps.

3.3 Results: sea ice

Results from our NEMO-LIM simulation are now examined, starting with the overall state of the sea ice and the ITD. Except when compared to specific observational datasets, the last 20 years (1995-2014) of the outputs are analyzed. In this section and the following, mean seasonal cycles of several model fields averaged over the regions depicted in Fig. 3.1 and where sea ice concentration exceeds 15 % are shown. The 15 % threshold is required to avoid including areas of very low ice concentrations in summer, where the considered fields tend to depart very strongly from the values they have elsewhere. The selected ar-

Table 3.1: Sea ice metrics in observations or reanalyses and as simulated by the model. Sea ice extent is compared between 1983 and 2012 with passive microwave products generated with the Bootstrap algorithm (Comiso, 2000). Arctic sea ice volume estimates are from the PIOMAS reanalysis (Schweiger et al., 2011) over the 1983-2013 period. The Antarctic sea ice volume trend is from the model reconstruction by Massonnet et al. (2013) between 1980 and 2008.

	Arctic		Antarctic	
	Obs./reanalysis	Model	Obs./reanalysis	Model
Max. monthly extent (10^6 km^2)	15.5	17.1	19.2	20.8
Min. monthly extent (10^6 km^2)	6.7	7.9	3.2	7.6
Trend extent (10^3 km^2 year^{-1})	-53	-56	+21	+28
Max. monthly volume (10^3 km^3)	27.8	33.0	n/a	16.2
Min. monthly volume (10^3 km^3)	11.2	17.4	n/a	4.7
Trend volume (km^3 year^{-1})	-346	-361	$+36 \pm 34$	+60

eas are chosen so that the winter average values are typical of the inner sea ice pack. The Arctic area includes the Arctic Ocean and the marginal seas, excluding the Barents Sea and with boundaries at Bering Strait, the northern limit of the Canadian Arctic Archipelago (CAA) and Fram Strait. The Antarctic area is based on a visual examination of the position of the simulated winter sea ice edge. Additionally, several maps will be shown for February and July in the Northern Hemisphere (NH) and for January and August in the Southern Hemisphere (SH). These months have been found to be the most representative of the winter situation immediately prior to the sea ice extent maximum (February and August) and of the summer season (July and January) for the various fields that we examine.

3.3.1 Overall view

In Table 3.1, general sea ice metrics are given that allow to compare the model results with observations.

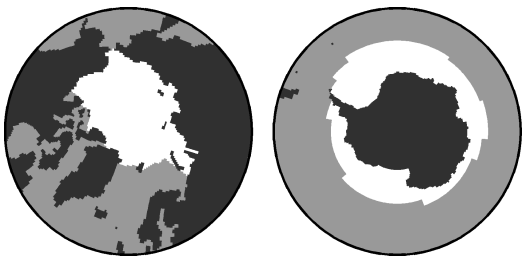

Figure 3.1: Selected areas for the computation of mean seasonal cycles.

Arctic sea ice extent is slightly overestimated compared to passive microwave products generated with the Bootstrap algorithm (Comiso, 2000). The positive bias is larger in winter and is comprised between 1 and 2×10^6 km^2 throughout the year. The declining trend over recent decades is in excellent agreement with observational estimates. While absolute values of ice volume appear significantly larger than the PIOMAS reanalysis using data assimilation (Schweiger et al., 2011), the amplitude of its mean seasonal cycle is very similar, as is its interannual trend. The differences in total volume can be shown to originate from the CAA, whose representation by the model is challenging at 1° resolution and where thick stagnant ice accumulates in LIM.

The positive bias in sea ice extent in the Antarctic is larger than in the NH, most importantly in summer when the observed extent is less than half the simulated one. This seems to be caused by an inability to melt ice rapidly enough during spring in the simulation. This issue was already present in studies using older versions of LIM with a similar atmospheric forcing (Massonnet et al., 2011; Lecomte et al., 2013), but is absent in Rousset et al. (2015) where another forcing formulation is used. The excessive summertime ice cover is located mostly in the eastern Weddell Sea, and to a lesser degree in the Ross and Amundsen Seas. This is the main discrepancy between model results and available observations, which has to be kept in mind when analyzing other aspects of the simulation. Interestingly, the simulated trend in Antarctic ice extent is comparable with satellite estimates, whereas the volume trend in LIM lies within the range provided by the model reconstruction with data assimilation by Massonnet et al. (2013).

3.3.2 Ice thickness distribution

Mean seasonal cycles showing the behavior of the ITD in LIM are presented in Fig. 3.2. In both hemispheres, the mean open water fraction falls very close to zero in winter and peaks between 0.3 and 0.4 in summer. As a reminder, these values are obtained from an averaging inside the sea ice pack and excluding areas with less than 15 % concentration. The amplitude of the seasonal variations of ice categories fractions tends to decrease with increasing thickness. This is more striking in the SH where the third category already has a very weak seasonal cycle. The distribution across the different classes is also very distinct in the Arctic and the Antarctic. In the former, all categories contribute notably to the total sea ice concentration, while in the latter the first two ice classes are clearly dominant, with a smaller contribution from the third one in winter. A recent study has shown that having five categories in an ITD may

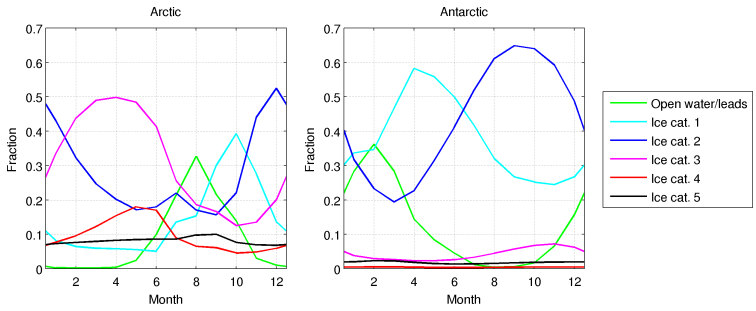

Figure 3.2: Seasonal cycles of simulated fractions of grid cells covered by open water/leads and by ice categories, averaged in the areas depicted in Fig. 3.1 and where sea ice concentration exceeds 15 %, in the Arctic (left) and the Antarctic (right). The upper bounds for the first four ice thickness categories are 0.63 m, 1.33 m, 2.25 m and 3.84 m. The fifth category is unbounded.

not be enough to provide an accurate representation of the Arctic sea ice cover (Hunke, 2014). The issue is therefore likely even more critical in the SH.

Fig. 3.3 shows that the distribution among ice categories is extremely variable in space. Thin ice forms as the freezing season begins, before being progressively replaced by thicker ice, either from thermodynamic growth or from deformation processes. This evolution is visible in the mean seasonal cycles as well. Starting in summer, the months of the maximum mean fraction of each ice class are indeed exactly ordered according to their thickness.

In February in the NH, high concentrations in the first and second ice categories are confined along the sea ice edge and in the marginal seas and eastern part of the Arctic basin, respectively. Most of the Arctic Ocean is occupied by ice in the third thickness category, with large values in the fourth and fifth ones north of Greenland and in the CAA. In July, extensive areas are still covered with ice in the third class, while the concentration of the first one has increased in the central part of the basin as a result of melting of thicker ice.

The same transitions across categories can be observed in the SH. In winter, thin ice is present in the northernmost regions, but also in coastal areas (mostly in the Ross Sea and along the coast of East Antarctica), where strong offshore winds transport ice northwards, creating polynyas and reducing the mean ice thickness (e.g., Barthélemy et al., 2012; Nihashi and Ohshima, 2015). Thicker ice in the inner sea ice pack is represented mostly by the second category, and to a small extent by the third one in the Weddell, Bellingshausen and Amundsen Seas. In summer, the open water fraction is more variable than in the Arctic, with large values in the regions of thin winter ice, especially in the Ross Sea polynya.

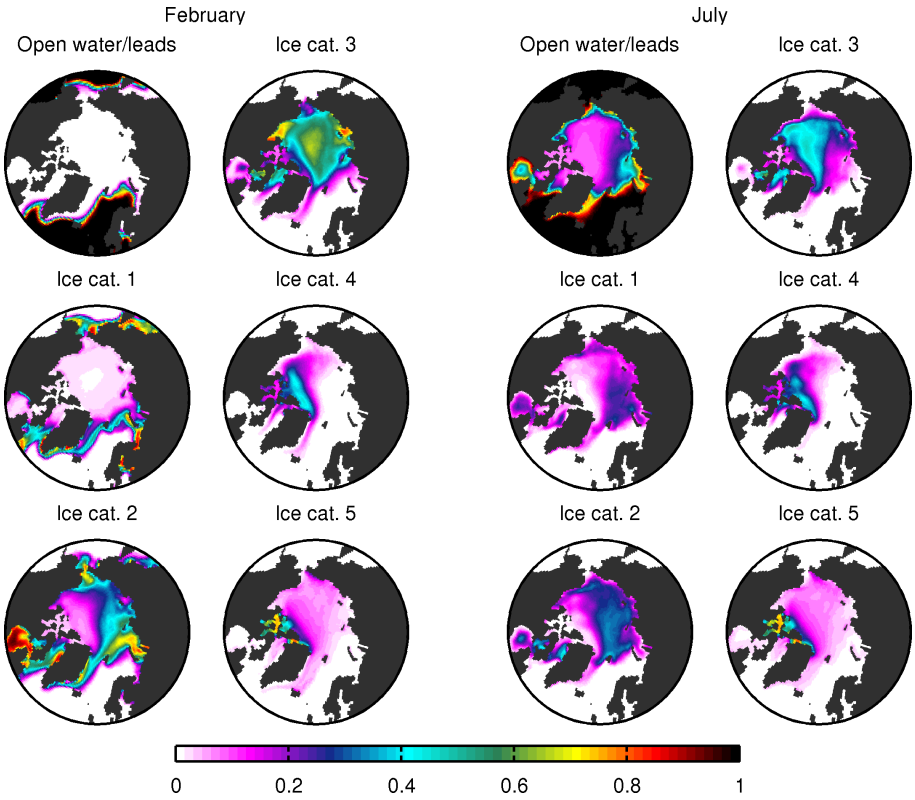

Figure 3.3: Simulated fractions of grid cells covered by open water/leads and by ice categories, for February and July in the Arctic and for January and August in the Antarctic.

The large-scale validation of a modeled ITD is a complex task. Nonetheless, the measurements collected during Operation IceBridge campaigns provide a way to carry out a model-observation comparison in specific seas and regions with sizes of the order of 500 km. Datasets obtained during airborne surveys from an array of remote sensing platforms have been processed to retrieve sea ice freeboard and snow depth, from which ice thickness is derived based on a hydrostatic balance assumption (Kurtz et al., 2013). Two separate datasets are utilized here. The first one, which has been reprocessed very recently, includes data collected mostly in the American side of the Arctic Ocean from 2009 to 2013 in the months of March and April (Kurtz et al., 2015). The second includes measurements from two campaigns in October of the years 2009 and 2010, primarily in the Weddell Sea (Kurtz et al., 2012).

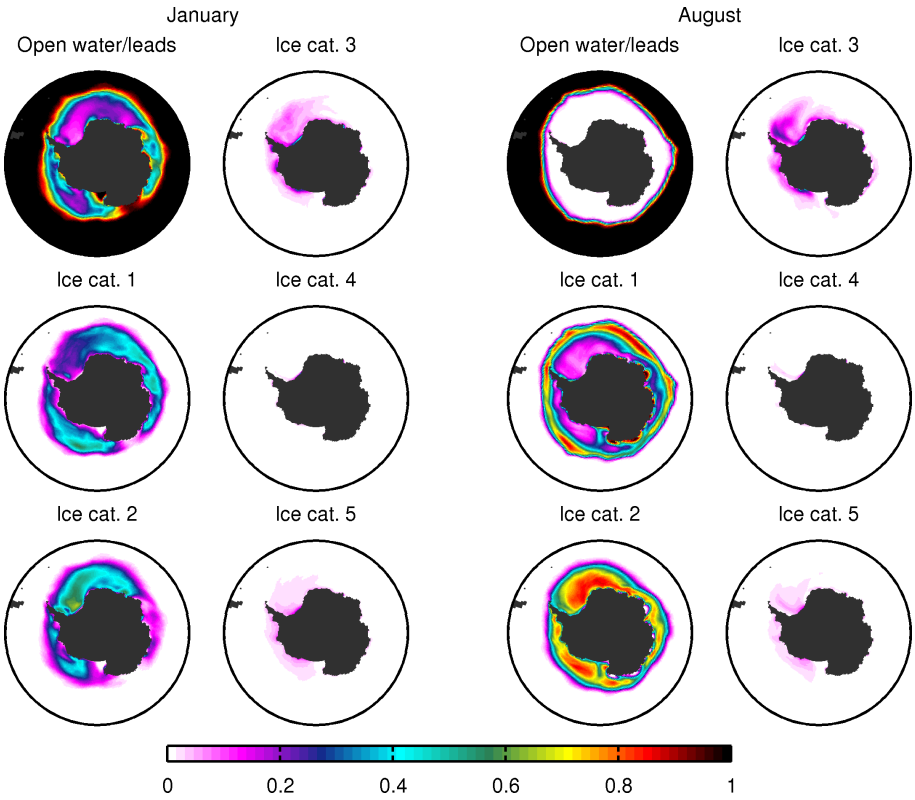

Figure 3.3: continued.

IceBridge data are given at 40 m resolution in the along-track direction. We compute the observed ITD by constructing histograms with thickness ranges corresponding to the LIM ice thickness categories. The simulated ITD is taken as the five ice classes average concentrations. Because of this difference in the way mean ITDs are computed, large spatial gradients in sea ice properties could make the model-data comparison questionable. In order to minimize the issue, the analysis is carried out in limited areas where the IceBridge data coverage is high (Fig. 3.4). Three areas are selected in the Arctic: north of Greenland and the CAA (NH-A, 84-87° N, 5-115° W), in the northern part of the Canada Basin (NH-B, 81-84° N, 120-155° W) and north of Alaska (NH-C, 72-77° N, 140-170° W). The data from March and April are aggregated. In the SH, a single area in the Weddell Sea is considered (SH-D, 68-73° S, 38-53° W). Nevertheless, the retrieval of snow depth from the radar system for the Antarctic region is still highly uncertain (Kurtz et al., 2013). As a conse-

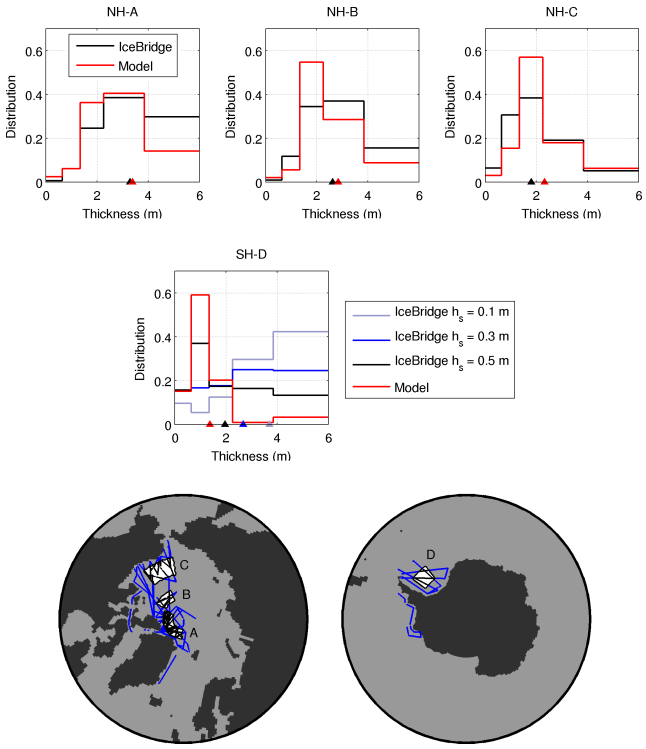

Figure 3.4: Ice thickness distribution in selected areas (delineated on the maps) in the IceBridge dataset and in the model, averaged in March and April between 2009 and 2013 in the Arctic and in October between 2009 and 2010 in the Antarctic. The triangles on the x-axis indicate the mean ice thickness in those areas. The three IceBridge curves on the SH plot correspond to different hypotheses regarding the snow depth onto sea ice (h_s, see text for details). The numbers of IceBridge data points used in NH-A, NH-B, NH-C and SH-D are 317 534, 55 069, 113 854 and 74 053, respectively.

quence, only sea ice freeboard is provided in the IceBridge dataset. We crudely assume three uniform snow depths of 0.1, 0.3 and 0.5 m, to obtain an uncertainty range in the ice thickness recovered from hydrostatic balance. The range in snow depth is likely sufficiently wide to include a realistic estimate (Lecomte et al., 2013). For points where the assumed snow thickness is larger than the measured freeboard, it is reduced to be equal to the latter. In the end, several tens of thousands thickness data points can be used in each region.

The ITDs derived from observations and from the model are shown in Fig. 3.4. In the Arctic, the overall shape of the distribution is well reproduced, exhibiting in each region a dominance of intermediate ice thicknesses over

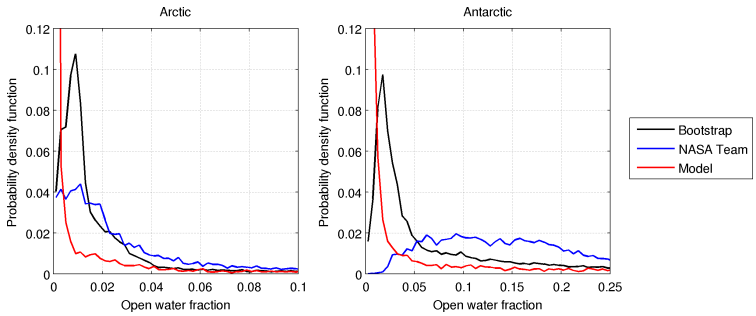

Figure 3.5: Probability density functions of the winter open water fraction, for the Bootstrap (Comiso, 2000) and NASA Team (Cavalieri et al., 1996) satellite products and for our model simulation, on average over the 2001-2010 period, for March in the Arctic (left) and for September in the Antarctic (right).

thin and thick ice types. Yet, quantitatively, large differences occur with IceBridge estimates. In NH-A, the model lacks 50 % of the ice thicker than 3.84 m. In the other two Arctic areas, the ice is too concentrated in the third category, at the expense of almost all other ones in NH-B, or of only the thinner ones in NH-C. The apparent good agreements between simulated and observed mean thicknesses are therefore achieved through a representation of the ITD that is reasonable but still displays clear biases. Errors up to 50 % in specific category concentrations are indeed not uncommon. It is worth noting however that the IceBridge ice thicknesses have a large uncertainty, of the order of 75 cm on average in the NH areas considered (Kurtz et al., 2015).

In the SH, the absence of snow measurements prevents a detailed model-observation comparison. Nonetheless, whatever the assumed snow depth, too much ice lies in the second category, while ice above 2.25 m appears critically missing from the modeled ITD. The processing of the IceBridge measurements includes a filter designed to remove the data contaminated by icebergs (Kurtz et al., 2012), which hence cannot explain this discrepancy. We note a negative bias in the simulated mean ice thickness in SH-D, that is specific to this region. Except in a few coastal areas, LIM in this configuration actually overestimates the Antarctic sea ice thickness compared to the ASPeCt dataset based on shipboard observations (Antarctic Sea ice Processes and Climate, Worby et al., 2008), with a mean absolute error of 45 cm.

A comparison of the observed and simulated winter open water fractions is finally presented in Fig. 3.5, over a common and longer period for both hemispheres (2001-2010). Results are qualitatively insensitive to the chosen winter months. A large spread exists between the probability density functions obtained for the Bootstrap (Comiso, 2000) and NASA Team (Cavalieri

et al., 1996) algorithms, although they utilize the same passive microwave datasets. These uncertainties in the observational estimates illustrate the difficulties to derive accurately low open water fractions from satellite measurements. The differences between the two products are especially large in the Antarctic, where the NASA Team algorithm yields much lower sea ice concentrations. In any case, the simulated open water fractions seem strongly underestimated in winter in both hemispheres. This is related either to a lack of ice divergence in the model, or to an excessively rapid closing of leads. The bias likely reaches a few percent in the Arctic and is as large as 10 to 15 % in the Antarctic if the NASA Team product is considered.

3.4 Results: ocean surface boundary conditions

The discussion in the previous section has demonstrated that the simulated concentrations in open water and in ice thickness categories differ quantitatively from reality. In the detailed examination of SBCs that follows, we will thus mostly focus on the thermohaline fluxes and surface stress for the six parts of grid cells separately, regardless of their areal fraction. In other words, the spatially averaged seasonal cycles are computed without weighting the fields by the concentrations of the open water and ice categories, in order not to be impacted by errors in the modeled ITD. The contribution of a specific portion of the surface to the total flux or stress is also of interest to estimate to which extent it participates in the forcing of the ocean. But these mean contributions depend on the areal fractions of open water and ice categories, whose representation in the simulation is uncertain. This aspect will consequently be only briefly addressed in Section 3.4.4.

3.4.1 Salt fluxes

The mean seasonal cycles of salt fluxes are shown in Fig. 3.6 and the geographical distributions are presented in Fig. 3.7. In winter, the most intense ice production rates take place in leads. Their salt fluxes are at least one order of magnitude larger than those of any ice category. They reach almost 0.05 and 0.04 kg PSU m^{-2} s^{-1} on average in the Arctic and Antarctic, respectively. To put these values in perspective, the growth of 1 m of ice at a salinity 30 PSU fresher than the SSS over the course of one month corresponds to a salt flux of 0.01 kg PSU m^{-2} s^{-1}, which would increase the salinity of a 50 m mixed layer by 0.5 PSU. Fluxes of large magnitude are widespread across the Arctic basin and their values tend to decrease towards lower latitudes and towards the sea ice edge, where air is less cold. In the SH, the largest fluxes are essentially found in a narrow band around the continent. Exceptions are the northern tip

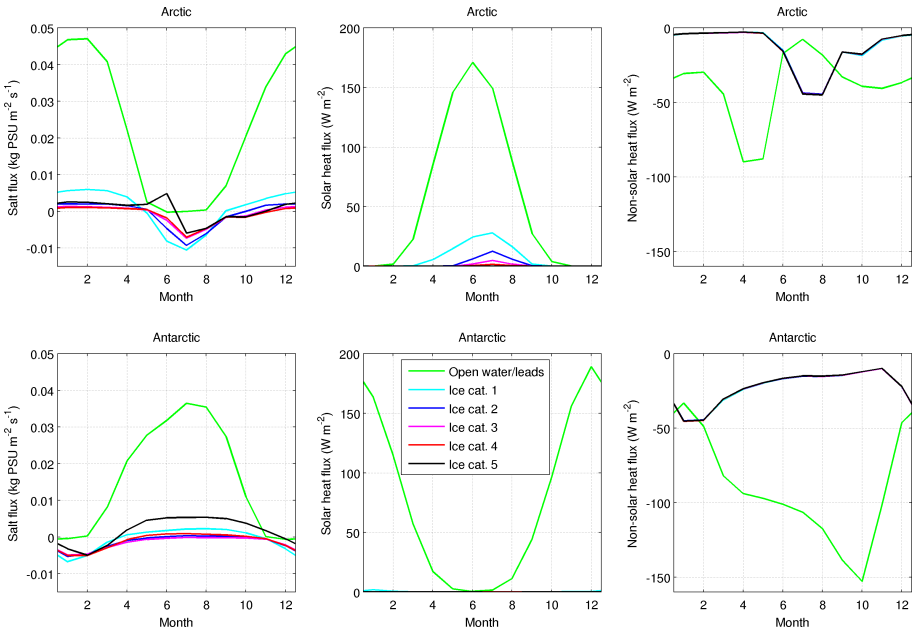

Figure 3.6: Seasonal cycles of simulated salt (left), solar heat (center) and non-solar heat (right) fluxes in open water/leads and under ice categories, averaged in the areas depicted in Fig. 3.1 and where sea ice concentration exceeds 15 %, in the Arctic (upper panels) and the Antarctic (lower panels). Positive fluxes are directed towards the ocean. The solar heat fluxes in the Antarctic are very close to zero for all ice categories, whereas the non-solar heat flux seasonal cycles are nearly identical for all categories.

of the Antarctic Peninsula, as well as a central part of the Ross Sea and an area west of the Amery Ice Shelf, where sea ice production is counteracted by high oceanic heat supply (see Fig. 3.9).

The freezing rate below existing ice is determined by the balance between the oceanic and conductive heat fluxes. Since the latter is inversely related to ice thickness while the former is identical for all categories, more ice forms under the thinner classes. Other factors contributing to this relation include a shallower depth of insulating snow on young thin ice and, in the Antarctic, more frequent snow-ice formation for thin ice that cannot support a lot of snow. Decreasing salt fluxes for categories of increasing thickness are indeed visible in model results, but the relation breaks in the Arctic seasonal ice zone and in the Antarctic for the fourth and fifth categories. In those regions, very thick ice is only produced by ridging, which incorporates large amounts of salt. The effect of later brine drainage is to yield positive salt fluxes, up to 0.02 kg PSU m^{-2} s^{-1} locally, even though such ridges may be so thick as to

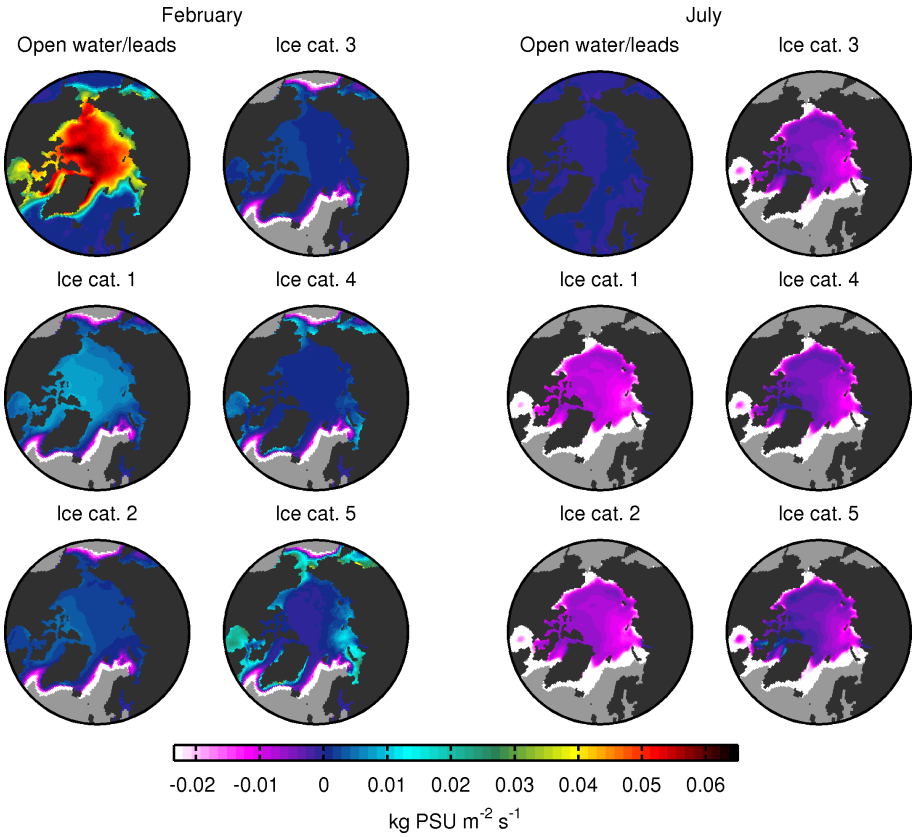

Figure 3.7: Simulated salt fluxes in open water/leads and under ice categories, for February and July in the Arctic and for January and August in the Antarctic.

melt from below throughout the year. This process occurs, however, for very small concentrations. Finally, for all categories and both hemispheres, sea ice advected close to or across the ice edge is melting, hence freshening the ocean, even during the coldest winter months.

In summer, the salt fluxes in the open water and leads are negligible. They actually only comprise the effects of evaporation and precipitation, since no explicit lateral melt is implemented in LIM. Besides, no runoff from the snow and ice surface melt is assumed. This is a physical shortcoming of the model, but determining the fraction of the meltwater that flows onto the ice surface and reaches the open water is a non-trivial question. This is also related to the representation of melt ponds, which are absent from this version of LIM but have been examined recently (Lecomte et al., 2015).

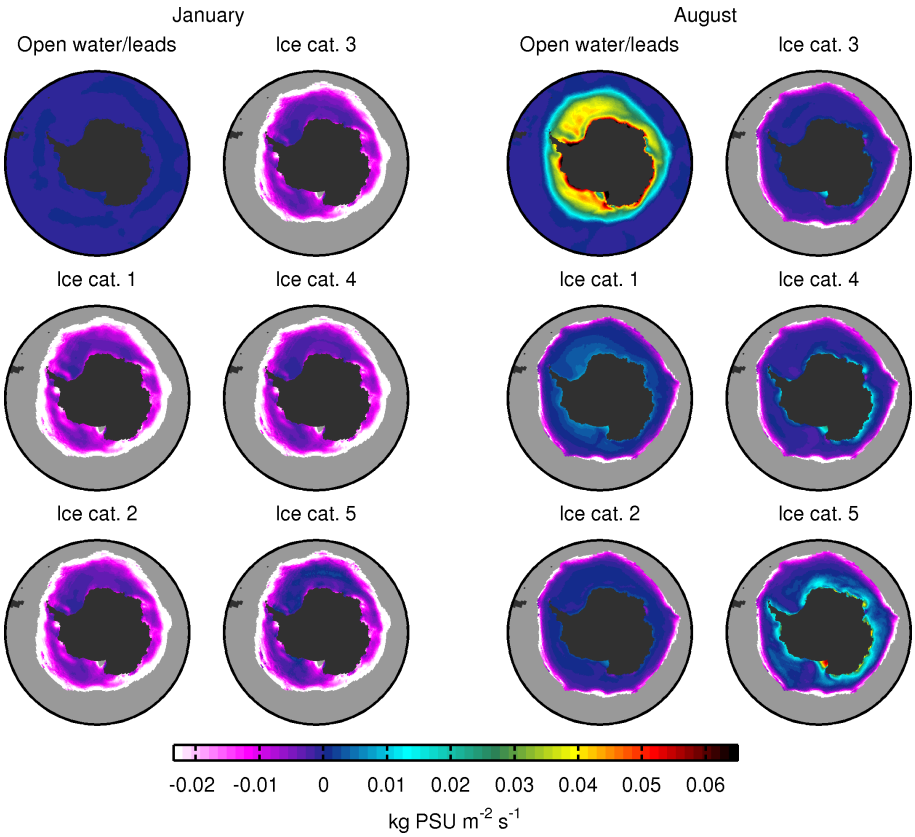

Figure 3.7: continued.

The larger absolute value of negative salt fluxes below ice during summer compared to the positive fluxes in winter indicates than melting is more rapid than freezing. Summer fluxes are of the order of -0.01 kg PSU m^{-2} s^{-1} in the NH and -0.005 kg PSU m^{-2} s^{-1} in the SH. The differences among the ice categories show that the melt rate varies from one to the other as well. Thin ice loses its snow cover more rapidly, which increases its albedo and its surface melt. In July in the Arctic, the ocean freshens almost twice as fast under the first category than under the fifth. The peak in salt flux for the fifth ice class in June is due to brine flushing favored by increasing ice temperatures and meltwater input at the surface. The largest freshening occurs along the sea ice edge, where air temperatures are high and where the ocean is strongly warmed by solar radiation entering large open water areas.

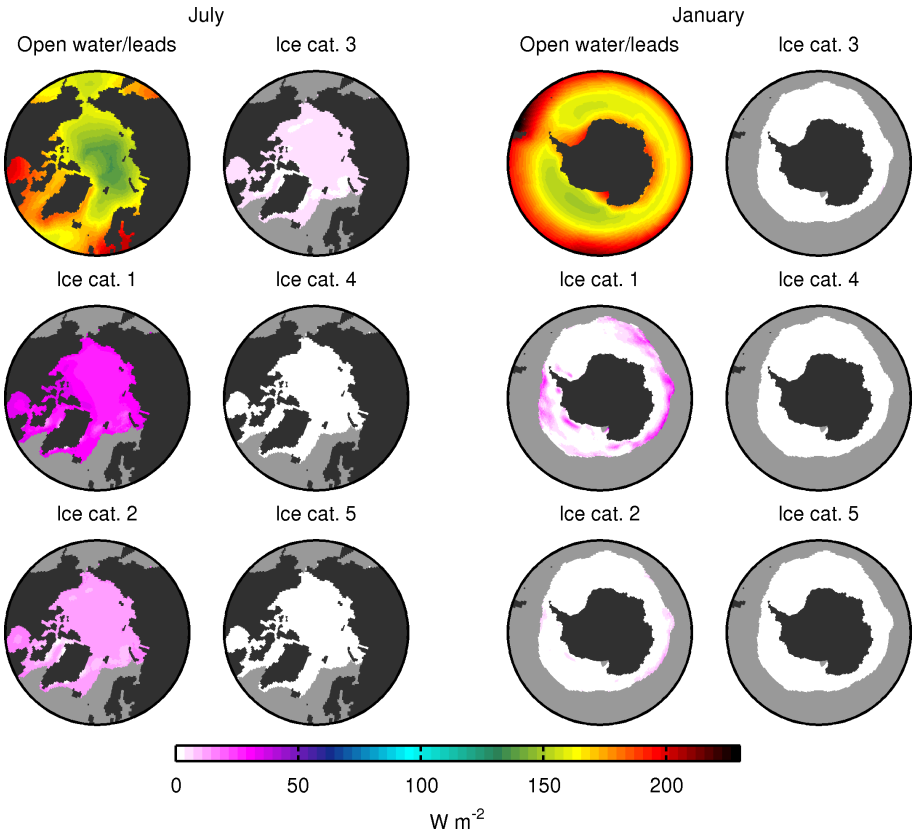

Figure 3.8: Simulated solar heat fluxes in open water/leads and under ice categories, for July in the Arctic and for January in the Antarctic.

3.4.2 Heat fluxes

Simulated solar heat fluxes are shown in Figs 3.6 and 3.8. Their mean seasonal cycle for the open water portion of grid cells is mostly driven by the strong seasonality of insolation in polar regions. To a small extent, these cycles can be modulated by changes in cloudiness, whose importance is clearly visible in the spatial distribution. In the Arctic, solar radiation at the ocean surface is essentially zero from October to February and peaks at 170 W m^{-2} in June. The mean solar heat flux in the SH area that we have chosen for analysis (Fig. 3.1) is close to zero only from May to July, because it extends to lower latitudes. The maximum insolation of 190 W m^{-2} occurs in December.

As explained in Section 3.2.2.2, the amount of solar energy transmitted through sea ice depends not only on its thickness, but also on the state of the

snow cover and of the ice surface. In our simulation, Antarctic sea ice remains snow-covered throughout summer, except the first category in limited areas along the edge and in the Amundsen Sea. There, up to 25 W m^{-2} can be transmitted through ice. Yet, on average, little solar radiation appears to reach the Southern Ocean from the ice, although this claim could be affected by the positive summer ice bias in the model.

The situation is different in the Arctic. Except very locally for the thickest ice, snow melts away during summertime. The peak in transmitted solar heat results from both the changes in surface conditions and the general increase in insolation. Expectedly, more radiation enters the ocean earlier in the season through thinner ice. The maximum occurs in July with values of 28, 13 and 5 W m^{-2} on average for the first three categories, while being negligible for the thickest two. This is slightly later than suggested by the results of Arndt and Nicolaus (2014), whose observation-based estimates indicate a maximum monthly mean solar heat flux under ice in June, with 96 % of the annual input taking place between May and August. Using under-ice measurements taken mainly in August 2011, Nicolaus et al. (2012) find a threefold increase in transmitted solar radiation between first-year ice and multi-year ice. The ratios between the solar heat flux in August under the first category and the second, third and fourth ones are 3, 9 and 27, respectively. Under the assumption that thicker ice is older, this might suggest too large a gradient in transmitted solar energy in the model. Finally, energy budget measurements of a melting ice floe 0.8 m thick north of Svalbard in July and August 2012 give a transmitted heat flux through ice of 26 W m^{-2} (Hudson et al., 2013). Simulated solar fluxes for the corresponding region and period range between 10 and 15 W m^{-2} for the second ice category, whose thickness interval (0.63 to 1.33 m) encompasses that of the observed floe. A better agreement is found with the thinner first category, whose fluxes lie between 20 and 30 W m^{-2}.

The mean seasonal cycles of non-solar heat fluxes are plotted in Fig. 3.6. As mentioned in Section 3.2.2.2, differences among the sea ice categories can only originate in heat fluxes associated with mass exchanges in the model. It turns out that the fluxes for the different categories are practically indistinguishable, meaning that the only significant contribution is the oceanic heat flux to the ice base. Only the first category is therefore represented in the spatial distributions shown in Fig. 3.9. In contrast to the solar component of the surface heat flux, the non-solar part always acts to cool the ocean.

Seasonal changes in ocean-to-ice heat flux are mostly driven by SST variations, because the ice base temperature is fixed at the freezing point, which does not vary much. Maxima (in absolute values) occur in both hemispheres just after the peak in insolation, i.e. in July and August in the NH and in January and February in the SH. The oceanic heat loss to the ice is around

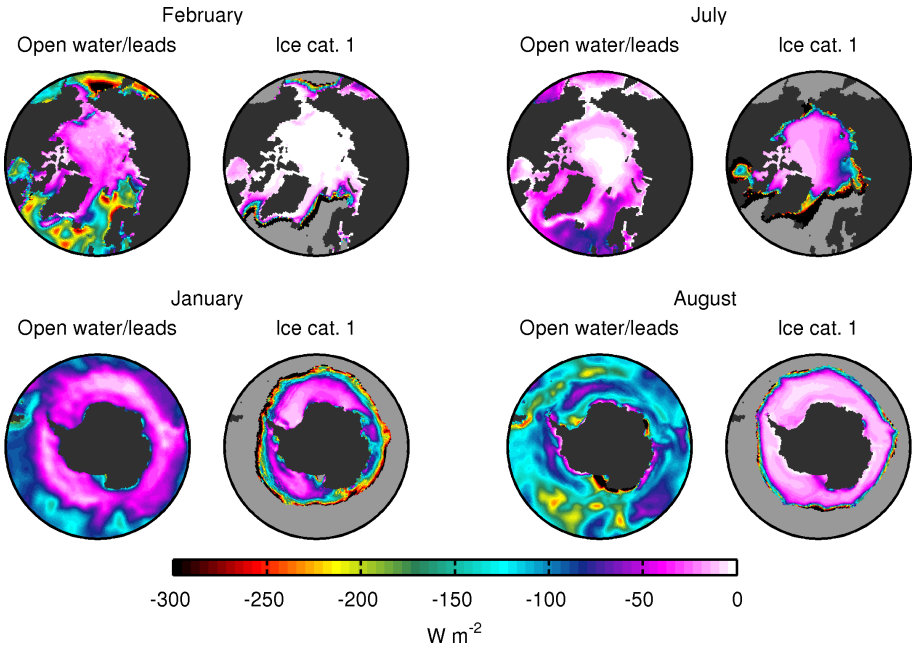

Figure 3.9: Simulated non-solar heat fluxes in open water/leads and under the first ice category, for February and July in the Arctic and for January and August in the Antarctic.

45 W m^{-2} on average during these months. As insolation vanishes and the solar heat stored in the ocean decreases, the oceanic heat flux diminishes, reaching minima of 3 W m^{-2} in April in the Arctic and 10 W m^{-2} in November in the Antarctic, on average. At those times, the ocean surface is maintained above the freezing point mainly due to entrainment of warmer water from below. The very low value in the NH is consistent with the view that, at least away from shallow bathymetric features, heating of the Arctic mixed layer mostly originates in summer solar heating (Maykut and McPhee, 1995; McPhee et al., 2003).

As shown in Fig. 3.9, strong spatial variations exist, which complicates the comparison between the existing local observations and the simulated average values given above. Higher heat fluxes are encountered in winter in peripheral regions where a longer ice-free season allows more solar energy to enter the ocean (Hudson Bay, for instance) and along the ice edge where sea ice is advected in warm waters. In summer, intense oceanic heat fluxes are associated to large open water fractions and reach several hundreds W m^{-2} in low ice concentration areas.

In the Arctic, the high mean summertime value of 45 W m^{-2} arises partly from the large fluxes in the low ice concentration regions. Based on data collected between 2002 and 2010 in the Transpolar Drift in the framework of the North Pole Environmental Observatory, Stanton et al. (2012) obtained a lower maximum ocean-to-ice heat flux of around 15 W m^{-2} from mid-July to the end of August. In their energy budget analysis of a melting ice floe in the Nansen Basin in July and August 2012, Hudson et al. (2013) found that the oceanic turbulent heat flux provided, on average, 13 W m^{-2} of energy to the ice. Measurements from the SHEBA study (Surface Heat Budget of the Arctic Ocean) in 1997 and 1998 showed a heat flux as low as a few W m^{-2} from October through June, followed by a steady increase reaching a peak value of about 33 W m^{-2} in July (Perovich and Elder, 2002). Results from the AIDJEX campaign (Arctic Ice Dynamics Joint Experiment) in 1975 in the Beaufort Sea also found the heat flux from the ocean to the ice to be strongly seasonal, with maximum values of 40 to 60 W m^{-2} in August (Maykut and McPhee, 1995). A comparison with the synthesis by Krishfield and Perovich (2005) ultimately confirms the good observation-model agreement, at least qualitatively, at the scale of the Arctic basin (Fig. 5 in the above-mentioned reference).

Oceanic heat flux measurements are even rarer in the Antarctic. Observations collected during the Austral winter in 1994 in the Weddell Sea near Maud Rise yielded fluxes between 25 and 35 W m^{-2} (McPhee et al., 1999). Mixed layer turbulence data obtained during two wintertime drift stations in August 2005 in the same region gave average fluxes of 13.8 and 28.0 W m^{-2} (Sirevaag et al., 2010). By comparing sea ice thickness observed using upward-looking sonars with simulations of thermodynamic sea ice growth in the central Weddell Sea, Behrendt et al. (2015) noted that the best consistency between observations and model results was obtained for oceanic heat fluxes between 6 and 14 W m^{-2}. Although the information is very limited, these values appear compatible with the mean seasonal cycle in Fig. 3.6 and with the spatial distribution in Fig. 3.9.

The non-solar component of the surface heat budget is significantly different in the open water compared to the ice-covered fraction of the grid cells. The heat loss at the water surface depends on both the SST and the state of the atmosphere. Minima are reached in summer, about at the same period ocean-ice fluxes are at their maximum, in absolute value. The mean in the regions considered for the computation of seasonal cycles is as low as -8 W m^{-2} in the Arctic and -30 W m^{-2} in the Antarctic. As already explained, during the freezing season, the total heat loss from the ocean to the atmosphere is used partly to cool the ocean and partly to compensate latent heat released by sea ice production, and the flux considered here corresponds to the first component only. Very low values simulated in the Antarctic in winter along the

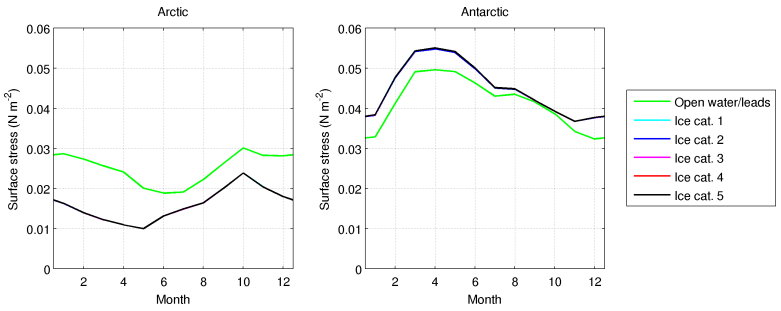

Figure 3.10: Seasonal cycles of simulated surface stress modules in open water/leads and under ice, averaged in the areas depicted in Fig. 3.1 and where sea ice concentration exceeds 15 %, in the Arctic (left) and the Antarctic (right). The seasonal cycles are identical for all ice categories.

coast of the Amundsen and Bellingshausen Seas and of most of East Antarctica indicate that the ocean there is close to the freezing point and that almost all of the heat loss is used to form ice. On the contrary, large fluxes are found in the Weddell Sea (< -200 W m^{-2}) and in and west of the Ross Sea and west of the Amery Ice Shelf (< -300 W m^{-2}), which are the signs of a strong energy supply from the subsurface. On average, the non-solar heat flux becomes higher over the course of the freezing season, as the deepening of the mixed layer entrains larger amounts of heat, reaching -90 W m^{-2} in April in the NH and -150 W m^{-2} in October in the SH. The increase is relatively steady in the Antarctic, whereas in the Arctic, it first settles at an intermediate value between -30 and -40 W m^{-2} from September to February. A more detailed examination of its various components would be needed to fully understand this behavior. The smaller value in the Arctic again point towards a lower heat supply from the subsurface in that hemisphere.

3.4.3 Surface stresses

Simulated surface stress modules are shown in Figs 3.10 and 3.11. In open water, it actually corresponds to the wind stress. As parameterized in LIM, the ice-ocean stress is the same for all ice categories. Overall, surface stress is the SBC variable that differs the least between ice and open water in the model. Furthermore, it shows less seasonal variations than salt and heat fluxes. Maxima take place just after the sea ice extent minima, while minima occur a few months before. In the Arctic, stresses are typically 0.02 N m^{-2} in magnitude on average, and can be up to twice larger in the open water compared to the ice-covered fraction of grid cells. In the Antarctic, the typical module of the

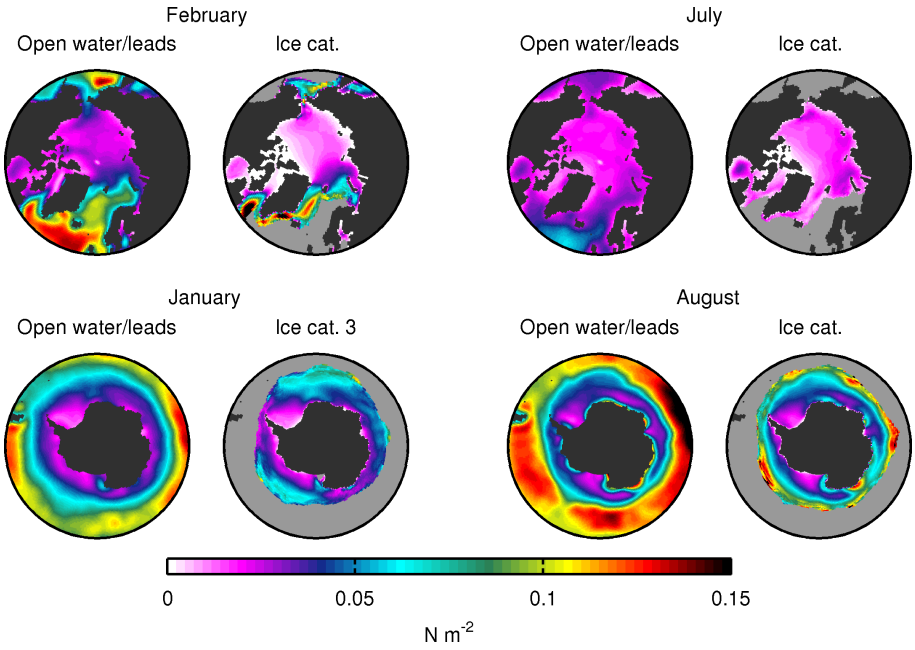

Figure 3.11: Simulated surface stress modules in open water/leads and under ice, for February and July in the Arctic and for January and August in the Antarctic.

surface stress is close to 0.045 N m^{-2}. It is slightly larger for ice than for open water and leads, which is made possible by the differences in drag coefficients between the atmosphere-ice and atmosphere-ocean interfaces (1.3×10^{-3} and 1×10^{-3}, respectively) and which reflects the more mobile nature of Antarctic sea ice compared to its Arctic counterpart.

In the Arctic, the spatial distribution of winter stresses in open water shows that surface winds are weak within the sea ice zone. High values are only found in peripheral seas outside the Arctic basin. Stresses are even smaller under ice, exceeding 0.05 N m^{-2} only in the Barents Sea, around Greenland and in the Bering Sea. Widespread areas of very low stresses along Siberia and in the CAA indicate almost motionless ice in the model. In July, winds appear to be weaker, mostly at lower latitudes, but the ice-ocean stresses start increasing in the inner pack as a result of a loosening and weakening sea ice cover. The Antarctic shares similarities with the NH, among which the low winds, hence stresses in open water, in summer and in winter inside the sea ice. Differences include the presence of strong coastal winds in winter, resembling the katabatic winds existing in reality, which drive locally stresses up to 0.1 N m^{-2} in open water and are also visible in the under-ice fields. Much

less ice is stationary along the coast than in the Arctic, reducing the regions where stresses are close to zero to small embayments barely visible in Fig. 3.11 and to the area close to the Amery Ice Shelf. The fact that Antarctic sea ice is thinner and not constrained in a basin implies that it is more tightly linked to winds, which is why the open water and ice stress maps match better than in the NH. Our results are in line with Goosse and Fichefet (1999), who had already pointed out that the modifications of the stress at the ocean surface induced by the internal ice forces have only a regional effect.

3.4.4 Integrated contributions

Although a specific fraction of a grid cell may have the largest fluxes, its net contribution to sea surface changes depends on its area. Integrated contributions of open water and leads and ice categories to the total mean fluxes and stress seen by the ocean are thus given in Table 3.2 for the typical winter and summer months that we have considered so far. This gives an insight into their relative importance in the surface forcing of the ocean. With the exception of the solar heat flux, the results described hereafter show that the contribution of any ice category, even the thickest ones, can be dominant over open water because of a much higher concentration.

Although winter leads have the largest salt fluxes due to intense ice growth, they only contribute 3 % to the total flux in the Arctic, and 12 % in the Antarctic, due to their very small concentrations. Associating these fluxes to frazil ice formation in open water, these numbers suggest an model underestimation of the amount of ice produced in this way. In the Antarctic in particular, local observations indicate that possibly up to 50 % of the ice volume originates from frazil (Wilchinsky et al., 2015, and references therein). In summer, the role of open water appears rather limited by weak freshwater fluxes, but this could be underestimated since lateral melt and runoff from ice are lacking in LIM. The salt budget is dominated in the NH by the first three categories, which combine non-negligible fluxes with high concentrations, and by the first two in the SH, mainly because they are the only ones with significant areas.

As suggested by previous results, almost all solar radiation reaches the ice-covered Southern Ocean through open water. Only 1 % of the total energy is supplied through the first sea ice category. During July in the Arctic, the average solar heat flux amounts to nearly 40 W m^{-2}, among which 20 % originates from radiation transmitted through the first three categories.

Since the non-solar heat flux and the surface stress are essentially the same for all ice classes, differences among them result from different mean areal coverage as well as distinct spatial distributions. Indeed, ice tends to be thin-

Table 3.2: Integrated contributions of open water and leads (O.w./l.) and ice categories (1 to 5) to the total mean fluxes and stress seen by the ocean (Tot.), in the areas depicted in Fig. 3.1 and where sea ice concentration exceeds 15 %. The winter (summer) month is February (July) in the Arctic and August (January) in the Antarctic. Mean fractions of open water/leads and ice categories are given (Frac.), along with corresponding contributions to salt (F_s), solar heat (F_{sol}) and non-solar heat (F_{nsol}) fluxes and to surface stress modules (τ).

	Frac. (%)		F_s (10^{-4} kg PSU m^{-2} s^{-1})		F_{sol} (W m^{-2})		F_{nsol} (W m^{-2})		τ (10^{-3} N m^{-2})	
	Win.	Sum.	Win.	Sum.	Win.	Sum.	Win.	Sum.	Win.	Sum.
Arctic										
O.w./l.	0.2	21.3	0.4	0.2	0.0	32.0	-0.3	-1.7	0.1	4.3
1	6.5	13.6	2.5	-15.7	0.0	3.7	-0.6	-7.4	1.9	2.4
2	32.3	22.0	5.2	-18.9	0.0	2.8	-1.3	-8.0	5.8	3.7
3	43.8	25.6	5.6	-13.2	0.0	1.2	-1.2	-5.7	4.7	3.6
4	9.6	8.9	0.8	-3.6	0.0	0.2	-0.3	-1.5	0.7	0.9
5	7.6	8.6	0.4	-3.7	0.0	0.0	-0.2	-2.4	0.7	1.0
Tot.	100.0	100.0	14.8	-54.8	0.0	39.8	-3.8	-26.7	14.0	15.8
Antarctic										
O.w./l.	0.4	28.3	1.1	-0.5	0.1	46.3	-0.8	-9.4	0.2	9.5
1	32.1	33.7	5.4	-20.7	0.0	0.6	-6.0	-13.9	16.9	14.1
2	61.1	31.7	2.1	-10.0	0.0	0.0	-8.5	-8.3	25.7	11.7
3	4.5	3.8	0.0	-0.9	0.0	0.0	-0.5	-0.9	1.4	1.0
4	0.4	0.5	-0.0	-0.2	0.0	0.0	-0.0	-0.2	0.1	0.1
5	1.5	2.0	0.4	-0.4	0.0	0.0	-0.2	-0.7	0.5	0.6
Tot.	100.0	100.0	9.1	-32.7	0.1	46.9	-16.0	-33.4	44.9	37.1

ner in areas close to the edge where the oceanic heat flux is higher, which explains the large contribution of the first category relative to its mean concentration (particularly obvious in summer in the Antarctic). The non-solar heat loss in open water and leads is less than 10 % of the total, except in January in the SH where it reaches 28 %, mostly due to large open water fractions. The link between mean concentrations and integrated contributions is even stronger for the stress module. This is consistent with a smaller spatial variability and with a lesser difference between the ice categories and the open water.

3.5 Conclusions

Sea ice being a fundamentally heterogeneous medium, its effects on the underlying ocean are highly spatially variable as well. Although most advanced sea ice models today attempt to represent the ice subgrid-scale heterogeneity by means of ice thickness distributions, the information about the spatial variability of surface boundary conditions is lost in the process of coupling them in a classic way to an ocean model. The present study is the first comprehensive examination of the simulated heterogeneity of ocean surface boundary conditions in an ocean-sea ice model including an ice thickness distribution, namely NEMO-LIM. It is intended to serve as a guideline for the understanding of small-scale ice-ocean processes, and in particular for the interpretation of studies evaluating subgrid-scale ocean vertical mixing schemes under sea ice. The heterogeneous nature of atmosphere-ice interactions is a related and interesting question, that we have not addressed in this work.

The analysis of sea ice results in our simulation calls for two comments about ice thickness distributions in general. First, a recent study has shown that the commonly used number and boundaries of ice categories may not be optimal for an accurate representation of Arctic sea ice (Hunke, 2014). We have shown here that Antarctic sea ice is mostly confined in the two thinnest ice categories. Therefore, it is likely that in the current configuration we do not make the best use of the ice thickness distribution in the Southern Hemisphere. The second comment concerns the simulated concentrations of ice of given thickness ranges. A brief evaluation of NEMO-LIM results against IceBridge observations has indicated errors up to 50 %, even when the mean modeled thickness is close to the observational estimate. A closer analysis of the origin of these errors, which could arise from biases in the large-scale sea ice deformation patterns or in the thickness redistribution process, is needed.

Our study has confirmed and quantified the high spatial variability of boundary conditions at the ocean surface in the sea ice zone in a model. While a large seasonality and geographical variations exist, the following conclu-

sions can be drawn. Unsurprisingly, the largest differences occur between the open water/leads and ice-covered fractions of grid cells. Even though the various sea ice categories are usually associated with smaller fluxes, integrated contributions (i.e. weighted by the concentrations) highlight their importance in the overall forcing of the ocean. Winter salt fluxes due to brine rejection during ice formation are up to an order of magnitude in leads than below the ice. In summer, solar radiation can only penetrate the ocean through open water in the Antarctic. The situation is only slightly different in the Arctic, where some solar energy is transmitted through thin ice. Except in summer, the ocean cooling by non-solar heat fluxes is several times larger in the open water than under ice. Finally, as parameterized in the model, the module of the surface stress is the same for all ice categories. It is up to 50 % smaller than the wind stress in open water in the Arctic, whereas it is just a few percent larger in the Antarctic where sea ice is more mobile. This variable is nonetheless much less spatially variable than thermohaline fluxes.

Salt and solar heat fluxes in the Arctic are furthermore dependent on the ice thickness category. Thin ice forms and melts faster, which is visible in the simulated salt fluxes in both hemispheres. In the Arctic, snow on top of the ice melts in summer, allowing solar radiation to be transmitted through the ice. This results in different amounts of solar heat flux reaching the ice-ocean interface for different thickness categories. If this differential heating could be properly taken into account, it could lead to an oceanic heat flux at the ice base that would be larger for thinner ice. Faster melt of thin ice could thereby enhance the ice-albedo feedback (e.g., Maykut and Perovich, 1987). Moreover, Long et al. (2015) have demonstrated that representing the subgrid-scale heterogeneity of shortwave radiation is required to simulate correctly the primary productivity in sea ice-covered waters.

At this point, the obvious next step is to implement an ocean mixing scheme that makes use of the subgrid-scale surface boundary condition variables, and no longer leaves them as mere diagnostics. The results presented above suggest that effects on model results would mostly arise from differences in convection due to the highly heterogeneous buoyancy fluxes, the latter being, at low temperatures, tightly linked to salt fluxes. Such a scheme has been developed, tested and evaluated in a parallel study (Chapter 4), which revisits and generalizes the work of Holland (2003) and Jin et al. (2015).

CHAPTER 4

A MULTI-COLUMN VERTICAL MIXING SCHEME TO PARAMETERIZE THE HETEROGENEITY OF OCEANIC CONDITIONS UNDER SEA ICE

Abstract

The heterogeneity of ocean surface conditions associated to a spatially variable sea ice cover needs to be represented in models in order to represent adequately mixed layer processes and the upper ocean density structure. This study assesses the sensitivity of the ocean-sea ice model NEMO-LIM to a subgrid-scale representation of ice-ocean interactions. The sea ice component includes an ice thickness distribution, which provides heterogeneous surface buoyancy fluxes and stresses. A multi-column ocean scheme is developed to take them explicitly into account, by computing convection and turbulent vertical mixing separately in the open water/lead fraction of grid cells and below each ice thickness category. For the first time in a three-dimensional simulation, the distinct temperature and salinity profiles of the ocean columns are allowed to be maintained over several time steps. It is shown that, if columns are laterally mixed with homogenization time scales shorter than 10 h, subgrid-scale effects

exist but the model mean state is practically unaffected. For longer mixing time scales, in both hemispheres, the main impacts are reductions in under-ice mean mixed layer depths and in the summer melt of sea ice, following decreased oceanic heat flux at the ice base. Large changes in the open water temperature in summer suggest that the scheme could trigger important feedback processes in coupled simulations.

4.1 Introduction

The sea ice covering the surface of polar oceans is an extremely heterogeneous medium. Within a restricted region, areas of open water, thin newly-formed ice, level ice a few meters thick or pressure ridges several meters thick may be found (Thorndike et al., 1975). Because the insulating properties of ice strongly depend on its thickness, the atmosphere-ice-ocean interactions are highly spatially variable as well. The ice growth rate, which is associated to brine rejections in the underlying ocean, decreases rapidly with thickness, especially for thin ice (Maykut, 1982). Furthermore, warming of the oceanic mixed layer in summer results mostly from the absorption of solar radiation in ice-free areas (Maykut and McPhee, 1995). The effects of sea ice on the sea surface temperature and salinity, hence on upper ocean stratification and mixing, are therefore variable at small horizontal scales. The mixed layer dynamics, on the other hand, is of crucial importance for the evolution of the sea ice cover. Indeed, it determines the ice bottom boundary conditions, most importantly influencing the ice energy balance through modulations of the oceanic heat flux at the ice base.

Modeling studies have shown that representing the heterogeneous nature of ocean surface boundary conditions under sea ice might be necessary to achieve an adequate simulation of the upper ocean physics in polar regions (Losch et al., 2006). Convective mixing related to intense brine rejections following ice formation is for instance likely to prevail only in open water or thin ice areas, which may represent a small fraction of grid cells in large-scale models. Brine rejection parameterizations have been developed to mimic such processes (e.g., Nguyen et al., 2009), but their effect is to suppress convection instead of making it localized (Chapter 2). They are consequently not able to account for the entrainment of water from the upper pycnocline, while this could constitute a significant component of the mixed layer heat budget (e.g., Polyakov et al., 2013; Close and Goosse, 2013). In the Arctic, a part of the solar heat that is absorbed in summer is indeed stored in a near-surface temperature maximum below the mixed layer (e.g., Jackson et al., 2012; Timmermans, 2015). Besides, although they are largely insulated from the surface layer by the strong halocline stratification (e.g., Toole et al., 2010; Shaw and Stanton, 2014), warm waters of Atlantic and Pacific origins are present at depth in the Arctic Ocean. Because of the much weaker stratification, entrainment of heat from below the mixed layer by localized convective mixing might be even more important in the Southern Ocean (e.g., Gordon and Huber, 1984; Martinson, 1990; Wong and Riser, 2011).

In most advanced sea ice models nowadays, an ice thickness distribution is used to represent the subgrid-scale variability of ice thickness, which has

long proven crucial to simulate accurately the ice cover evolution (e.g., Hibler, 1980). Heterogeneous ocean surface boundary conditions are therefore available in such models. For example, in the coupled ocean-sea ice model NEMO-LIM (see the next section for description), all surface variables show a clearly distinct behavior in the open water fraction of grid cells compared to the ice-covered one (Chapter 3). This includes freshwater, salt, solar heat and non-solar heat fluxes and the surface stress. Salt and freshwater fluxes, as well as the solar heat flux reaching the under-ice interface in the Arctic, further show a strong dependency on ice thickness. However, the coupling with a single ocean grid cell underneath requires the subgrid contributions from the different fractions of the surface to be aggregated (Fig. 1.3). The information about their heterogeneity is hence not utilized and potentially important subgrid-scale ocean physics is not resolved. Such merging of subgrid-scale fluxes amounts to assuming an instantaneous lateral mixing between the different parts of the ocean model columns. Although horizontal homogenization definitely occurs, it is most likely not instantaneous in all situations.

Previous studies have investigated the implications of explicit subgrid-scale vertical mixing schemes on ocean and sea ice simulations. By performing the mixed layer calculations separately in six columns corresponding to five ice thickness categories and to open water, Holland (2003) reproduced in a one-dimensional ocean and sea ice model the warming and freshening of summertime leads observed during the SHEBA campaign (Surface Heat Budget of the Arctic Ocean). In this study, the ice-covered columns were laterally mixed every time step, while the mixing with the open water column occurred every six hours. A large sensitivity to this homogenization time scale was underlined. Jin et al. (2015) implemented a two-column vertical mixing scheme in an ocean-sea ice configuration of the Community Earth System Model (CESM). The total salt flux resulting from ice growth was applied solely in one of the two columns, and lateral mixing between them occurred at the end of each time step. They noted strong effects on the simulated mixed layer depths only when the salt column was reduced to a size much smaller than the actual lead fraction. In the different context of heterogeneous ocean convection related to unresolved eddies, Ilıcak et al. (2014) also developed a two-column scheme with a homogenization at each time step. In contrast to the previous examples, changes in the depth of convective mixing between the columns were not caused by heterogeneous surface fluxes, but rather by different initial stratifications in each of them. Strong assumptions were needed to set the relative size of the two columns as well as the imposed spread in density profiles.

Our main objective in this study is to assess the impacts of a representation of subgrid-scale ice-ocean interactions on the NEMO-LIM model results. For that purpose, an improved multi-column ocean mixing scheme has been

developed for NEMO-LIM, based on and generalizing the studies described above. Basically, it consists in dividing each ocean grid cell in several columns, whose areas are imposed by the ice thickness distribution and the open water fraction provided by the sea ice model. Those columns are forced at the surface by available subgrid fluxes and vertical physics computations are done separately in each of them (Fig. 1.3). The major novelty lies in the possibility to maintain different columns properties over several time steps. It is the first time that this option is enabled in three-dimensional simulations. The sensitivity to the columns homogenization time scale is evaluated, and model results are analyzed in both polar regions.

This chapter is organized as follows. The NEMO-LIM model setup and the multi-column ocean scheme are described in Section 4.2 and 4.3, respectively. Results are presented and discussed in Section 4.4, starting with the heterogeneity of ocean surface boundary conditions in the reference simulation and continuing with the ocean and sea ice changes in the sensitivity experiments. A summary of our findings and concluding remarks are finally given in Section 4.5.

4.2 Model description

The current study is based on the global ocean-sea ice model NEMO-LIM, configured strictly in the same manner as in Chapter 3. Only the major model features and configuration aspects are thus described here, while components of importance to the multi-column scheme are presented in Section 4.3.2. A revised version of the Louvain-la-Neuve sea Ice Model (LIM3.5, Vancoppenolle et al., 2009b; Rousset et al., 2015) has been incorporated in version 3.5 of NEMO (Nucleus for European Modelling of the Ocean, Madec, 2008). The ocean component is a finite difference, hydrostatic, free surface, primitive equation model, while LIM is a dynamic-thermodynamic sea ice model including an ice thickness distribution (ITD) and an advanced halodynamics scheme. The number of ice thickness categories N_{cat} is taken equal to five, with upper bounds for the first four categories fixed at 0.63 m, 1.33 m, 2.25 m and 3.84 m.

The reference model simulation is initialized in January 1948 with climatological temperature and salinity data from the World Ocean Atlas 2001 (Conkright et al., 2002) and is run until December 2014. The ocean-sea ice coupled model is forced using the so-called CLIO formulation, by a combination of NCEP/NCAR daily air temperature and wind reanalysis data (Kalnay et al., 1996) and of monthly climatologies for relative humidity, cloudiness, precipitation and river runoffs. The ice-ocean coupling is thoroughly discussed in Chapter 3, whereas surface heat fluxes are parameterized as in Goosse (1997). The sea surface salinity (SSS) restoring has a time scale of

Table 4.1: List of symbols used in the text.

Symbol	Description	Value and/or unit
Δt	Ocean time step	1 h
N_{cat}	Number of ice categories	5
N_{col}	Number of ocean columns	6
F_{fw}	Freshwater flux	kg m^{-2} s^{-1}
F_s	Salt flux	kg PSU m^{-2} s^{-1}
F_{sol}	Solar heat flux	W m^{-2}
F_{nsol}	Non-solar heat flux	W m^{-2}
F_b	Buoyancy flux	m^2 s^{-3}
τ	Surface stress module	N m^{-2}
N^2	Square of the Brunt-Väisälä frequency	s^{-2}
K_z	Vertical eddy diffusivity	m^2 s^{-1}
$f^{(n)}$	Fractional area of column n	-
f_{mix}	Mixing fraction in MCO#2	-
τ_{hom}	Homogenization time scale in MCO#2	h

310 days for a 50 m mixed layer, but it is reduced under sea ice, proportionally to the ice concentration, in order to avoid altering the ice-ocean interactions. The ocean and sea ice models share the quasi-isotropic global tripolar grid ORCA1, with a nominal 1° resolution in the zonal direction and 46 layers based on a z coordinate on the vertical, ranging from 6 m at the surface to 250 m at the bottom. The ocean model time step Δt is 1 h. LIM is embedded in the surface boundary condition (SBC) module of NEMO, which is called every six time steps.

While the model skill in representing the ocean will be addressed when we examine the sensitivity experiments results, a few comments about the sea ice simulation are worthy. In the reference configuration, LIM tends to overestimate the sea ice extent compared to observations (Chapter 3). The bias in the Arctic ranges between between 1 and 2 $\times$ 10^6 km^2 throughout the year. In the Antarctic, the issue is most striking during the melting season, at the end of which the simulated extent is more than twice the observed one. The sea ice trends over the past decades, however, agree well in both hemispheres with satellite products (for the extent, Comiso, 2000) and reanalysis estimates (for the volume, Schweiger et al., 2011; Massonnet et al., 2013). NEMO-LIM is an appropriate tool to study the effects of a subgrid-scale representation of ice-ocean interactions, but this discrepancy between simulated and observed sea ice extents has to be kept in mind when analyzing model results.

4.3 Multi-column ocean scheme

Our aim in this study is to develop a scheme in which the ocean vertical physics is calculated separately below the open water and the N_{cat} ice thick-

ness categories, in order to investigate the role of subgrid-scale ice-ocean interactions. The ocean grid cells are therefore split into N_{col} parts that we name columns (with $N_{col} = N_{cat} + 1 = 6$), and the scheme is referred to as multi-column ocean (MCO). In this section, we first detail the modifications that are needed in the SBC module. Some background about the other ocean model components involved in the scheme is then presented, before describing the two distinct versions of MCO that will be tested.

4.3.1 Surface boundary conditions

First of all, the MCO scheme requires to keep track of the SBC variables for each column separately. We follow exactly the methodology presented in Chapter 3, where additional details can be found. The code modifications are straightforward and simply consist in saving the contributions of open water and ice categories when they are calculated. They mostly take place in the sea ice code. The salt, freshwater, solar heat and non-solar heat fluxes are diagnosed for each column, as well as the surface stress module. The latter is however identical for all ice categories. Since NEMO is used here in a linear free surface configuration, freshwater fluxes are turned into virtual salt fluxes that, along with real salt fluxes from sea ice processes, affect the SSS evolution.

A second modification is needed in the SBC and ice modules to allow the use of sea surface temperatures (SSTs) and SSSs specific to each oceanic column, instead of grid cell-average values. This further implies that the oceanic heat flux at the ice base can vary from one category to the other, mostly because of SST differences, but also because the ice bottom is at the local freezing point, which depends on the SSS.

4.3.2 Overview of relevant ocean model components

The MCO scheme requires substantial changes in the ocean model. The components of the code that are involved in its implementation are reviewed in Fig. 4.1. These are essentially the ones computing the vertical mixing and the update of tracers. Other components, related in particular to ocean dynamics and lateral mixing, are left untouched. Those only see the mean temperature and salinity (T/S) fields and are not directly affected by MCO.

In our model configuration, turbulent vertical mixing is handled with the so-called TKE scheme (Blanke and Delecluse, 1993; Madec, 2008). Turbulent kinetic energy (TKE) is calculated from a prognostic equation. The vertical eddy viscosity and diffusivity are then derived using diagnostic non-local turbulent length scales. The TKE input at the surface is prescribed as a function of the module of the surface stress τ, provided by the SBC module. Within

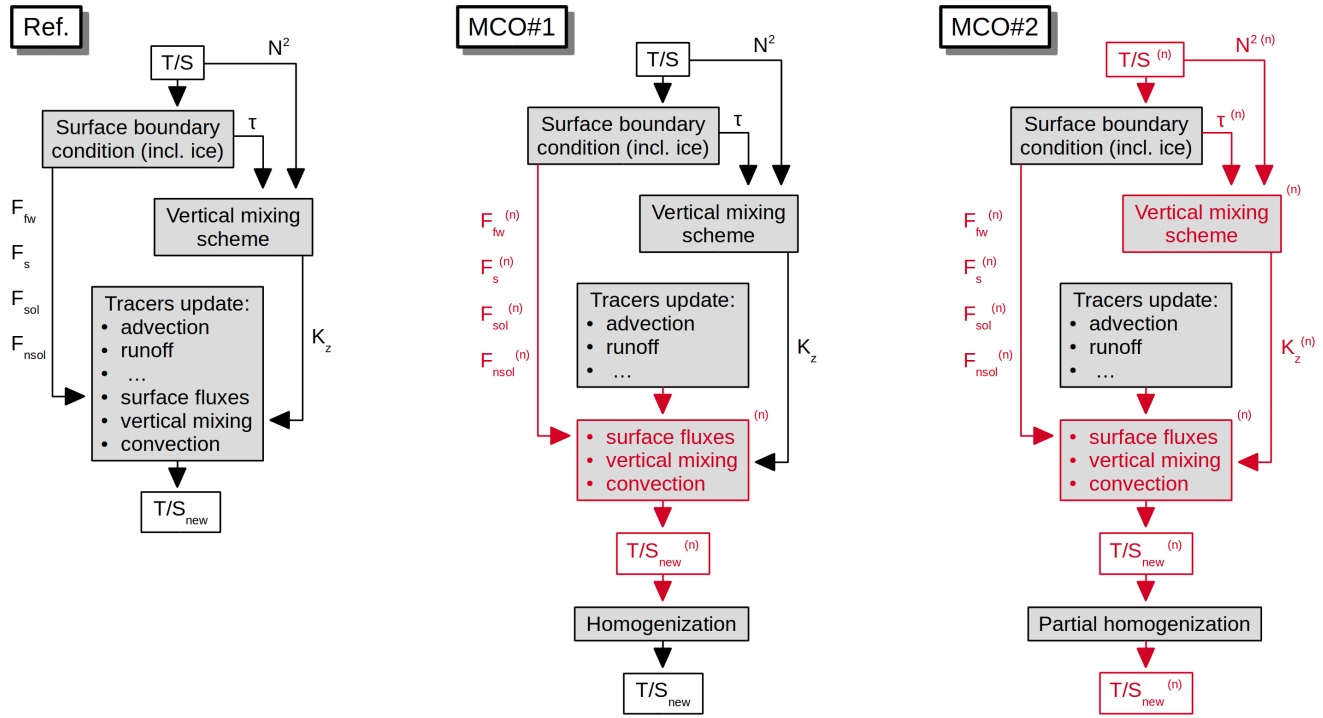

Figure 4.1: Model components and variables relevant to MCO, as they stand in the reference code (left) and as they are modified in the MCO schemes (center and right). T/S denotes the temperature and salinity fields, whose surface values are used by the SBC module, while vertical profiles are used to compute the water column stability. Vertical mixing and convection are treated using the TKE and NPC schemes, respectively, which are described in Section 4.3.2. The elements in red and with exponents (n) are the ones that exist/are computed separately in each column.

the ocean, TKE is produced by vertical shear and destroyed by stratification, which is represented by the square of the Brunt-Väisälä frequency N^2. The TKE evolution is further influenced by vertical diffusion and Kolmogorov dissipation. Among the outputs of the TKE scheme, the most important one in the context of MCO is the vertical eddy diffusivity K_z.

The part of the code most impacted by MCO is the tracer update, where the changes in temperature and salinity from various processes are successively taken into account. Advection, lateral mixing, runoffs and bottom boundary layer processes are associated with tracer trends that will remain common to all columns, while others will be computed separately within the MCO schemes. These first include the application of surface fluxes (freshwater F_{fw}, salt F_s and non-solar heat F_{nsol}). The penetrative solar radiation scheme used in our configuration implies that the solar heat flux F_{sol} is not, strictly speaking, a surface flux. Instead, it is exponentially absorbed in the first few tens of meters of the ocean. We will nonetheless not make the distinction further in the text. The effect of vertical mixing is then calculated, using the K_z mixing coefficient from TKE. Finally, a non-penetrative convection scheme (NPC, Madec et al., 1991) is applied to remove the static instabilities that may have appeared in any of the ocean columns.

4.3.3 MCO#1

The main feature of the first version of the MCO scheme is to homogenize the oceanic columns at the end of each time step. It follows in this respect the work of Ilıcak et al. (2014) and Jin et al. (2015). Given the NEMO time-stepping, the only differences in turbulent mixing that could arise across the columns would be due to different surface stresses in open water/leads and below ice categories. However, Chapter 3 has shown that the stress is the SBC variable that shows the least variability at the subgrid scale. Therefore, in MCO#1, the only mixing process that is computed separately in each column is convection, which may present a strong heterogeneity as a result of the large subgrid-scale variability of buoyancy fluxes.

The details of the implementation are illustrated in Fig. 4.1. The tracer trends due to processes common to all columns are first calculated. These trends are then updated in the N_{col} columns using the specific thermohaline fluxes provided for each of them by the SBC module. In contrast to the study of Jin et al. (2015), where only a subgrid-scale repartition of salt fluxes is accounted for, we deal with all surface fluxes and with their simulated distribution across the open water/leads and ice categories. Vertical mixing is then computed, using however the same diffusivity K_z in each column. Note that, as in the reference code, this mixing coefficient is calculated at the beginning

of the time step and hence cannot be affected by the buoyancy fluxes applied during the latter. Finally, the NPC convection scheme is called, yielding N_{col} T/S profiles at each grid point. The last step consists in the homogenization of these profiles, which is done in a conservative way by weighting them by the columns relative areas.

4.3.4 MCO#2

The principle of the second version of MCO is to allow the ocean columns to be maintained over multiple time steps. In several aspects, it corresponds to a three-dimensional generalization of the study by Holland (2003). A number of technical issues need to be addressed and consequently make the implementation of MCO#2 much more complex than MCO#1. Furthermore, since the differences in T/S fields among the columns can grow over time, the vertical mixing scheme has now also to be called independently in each of them.

At the beginning of a time step, N_{col} T/S profiles are available at each grid point. The SBC module, including the sea ice model, receives SSTs and SSSs that may differ across the columns. This means in particular that atmosphere-ocean exchanges in open water are calculated with a specific SST. The heat fluxes at the base of each ice category are likewise computed with distinct SSTs and SSSs (hence freezing points). The sea ice integration is possibly associated with shifts in the ITD and changes in the open water fraction, which induce modifications of the column areas. As a consequence, a redistribution of T/S profiles is required. It is handled in the following basic way. On the one hand, the properties of columns of decreasing area are unchanged. On the other hand, expanding ones are updated according to:

$$X_{new}^{(n)} = \frac{f_{old}^{(n)} X_{old}^{(n)} + (f_{new}^{(n)} - f_{old}^{(n)}) X_{rds}}{f_{new}^{(n)}},$$

where $X^{(n)}$ is the field considered and $f^{(n)}$ the fractional area of column n. The field X_{rds} used in the redistribution corresponds to the average in the areas lost by the decreasing columns:

$$X_{rds} = \frac{\sum_{n=1}^{N_{col}} \max(0, f_{old}^{(n)} - f_{new}^{(n)}) X_{old}^{(n)}}{\sum_{n=1}^{N_{col}} \max(0, f_{old}^{(n)} - f_{new}^{(n)})}.$$

In the vertical mixing scheme, the production of TKE by shear is computed only once, using velocities and a turbulent viscosity that are common to all columns. This term is then used in the TKE evolution calculations that are done separately in each column. These use distinct surface stress modules as

boundary conditions in the ice-free and ice-covered parts of grid cells, as well as stratifications specific to each column. This results in N_{col} vertical diffusivity profiles K_z at each grid point. The profiles of TKE by column are transferred to the next time step in exactly the same way as the T/S fields. They undergo in particular the same redistribution as described above. A final TKE computation is done based on the mean surface stress and mean stratification, in order to calculate the eddy viscosity for use in the ocean dynamics and in the shear production.

The update of tracers is basically the same as in the MCO#1 case, except that the turbulent vertical mixing coefficients can now differ among the columns. Nonetheless, a major difference is that the T/S profiles are only partially homogenized. More precisely, at each time step and for each oceanic column, a fraction f_{mix} of the profile is replaced by the average:

$$X_{new}^{(n)} = (1 - f_{mix}) X_{old}^{(n)} + f_{mix} X_{ave},$$

where the average X_{ave} is simply:

$$X_{ave} = \sum_{n=1}^{N_{col}} f^{(n)} X_{old}^{(n)}.$$

This actually corresponds to a restoring towards the mean profile, with a time scale τ_{hom} given by:

$$\tau_{hom} = \frac{\Delta t}{f_{mix}},$$

with Δt the ocean time step.

4.3.5 Sensitivity experiments

MCO#1 has no tunable parameter. The columns homogenization in that version of the scheme is complete and has a fixed implicit time scale equal to the ocean time step, i.e. 1 h in our model configuration. The only parameter in the MCO#2 scheme is the homogenization time scale τ_{hom} between the columns. This lateral mixing is most likely variable both in space and time, because it depends on the columns distribution and on the ocean and sea ice dynamics (see the discussion in Section 4.4.4). For the sake of simplicity, it is kept constant in this study.

The set of sensitivity experiments conducted in this chapter is given in Table 4.2. The REF and S1.1 experiments correspond to the reference code without MCO scheme and to MCO#1, respectively. For MCO#2, a wide range of homogenization time scales are tested, from 2 to 250 h, which are equivalent

Table 4.2: List of sensitivity experiments.

Experiment	MCO	f_{mix}	τ_{hom}
REF	no	n/a	n/a
S1.1	MCO#1	n/a	~ 1 h
S2.2	MCO#2	0.5	2 h
S2.10	MCO#2	0.1	10 h
S2.50	MCO#2	0.02	50 h
S2.250	MCO#2	0.004	250 h

to mixing fractions from 0.5 to 0.004. All sensitivity tests begin in 1985 from a restart of the REF simulation. They are run until end of 2014 and, unless otherwise stated, their last 20 year outputs are analyzed. The 10 year spinup is sufficient for the mixed layer and sea ice to adjust to the introduction of the MCO schemes.

4.4 Results and discussion

The results of the reference and sensitivity experiments are now presented. We first illustrate the heterogeneity of SBC across the columns, then examine the impacts of MCO on the ocean properties and finally investigate feedbacks on the sea ice itself. Several diagnostics consist of spatial averages, which are computed in the areas represented in Fig. 4.2. The objective is to obtain mean values that are representative of the inner sea ice pack and of regions where significant changes occur in the ocean. The area chosen for the Arctic is delineated by the 500 m isobath and by the 80°N parallel in Fram Strait, hence excluding the highly stratified continental shelves where little vertical mixing occurs. Without an obvious physical northern boundary, the Antarctic area is based on a visual examination of the simulated sea ice concentration, and is chosen as to ensure that is is fully covered with ice in winter.

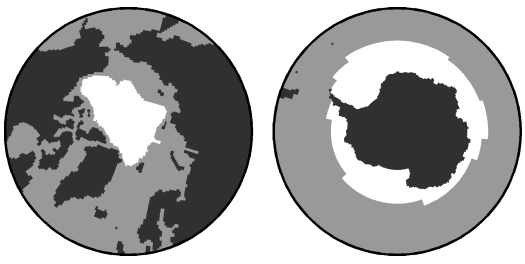

Figure 4.2: Selected areas for the computation of spatial averages.

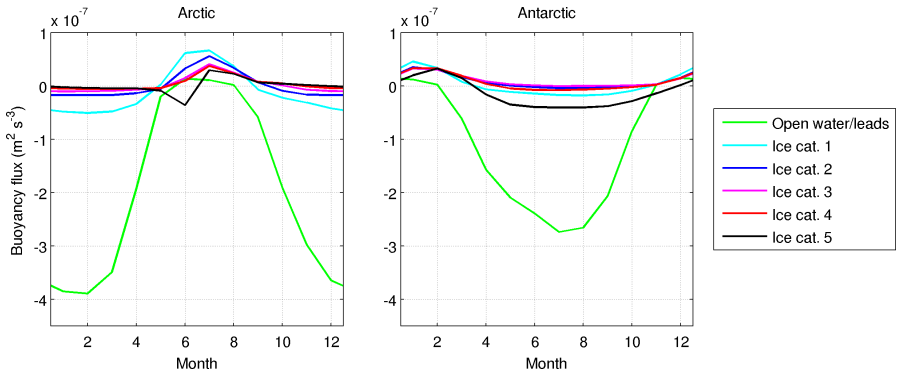

Figure 4.3: Seasonal cycles of the ocean surface buoyancy flux in each column in experiment REF, averaged in the areas depicted in Fig. 4.2 and where sea ice concentration exceeds 15 %, in the Arctic (left) and in the Antarctic (right).

4.4.1 Surface boundary conditions

A complete discussion of the modeled SBC heterogeneity across the columns in NEMO-LIM is provided in Chapter 3. Only major results are recalled here.

Changes in the density structure of the ocean upper layer, which may lead to convective mixing, are largely driven by the fluxes of salt, freshwater and heat that influence the evolution of SST and SSS. These fluxes can be combined into a single buoyancy flux F_b following:

$$F_b = \frac{g}{\rho_w}\left(\frac{\alpha_T}{c_w}(F_{sol} + F_{nsol}) - \beta_S F_s^*\right)$$

where g, ρ_w and c_w are the gravitational acceleration (9.81 m s^{-2}), reference seawater density (1035 kg m^{-3}) and specific heat (4000 J kg^{-1} K^{-1}), respectively. The thermal expansion and haline contraction coefficients α_T and β_S are taken equal to 0.3 10^{-4} K^{-1} and 7.7 10^{-4} PSU^{-1}, respectively, which are typical values for the cold and fresh waters found in the polar oceans (Marshall and Plumb, 2007). Finally, F_s^* is the total salt flux made up of real components from sea ice processes (F_s) and virtual components associated with freshwater fluxes (F_{fw}).

The mean seasonal cycles of the simulated ocean surface buoyancy flux for all columns are plotted in Fig. 4.3. Positive values indicate a gain of buoyancy, leading to an increase in stratification. The averaging is computed without weighting the fluxes by the column fractional areas. Furthermore, it only takes into account regions where the sea ice concentration exceeds 15 %. This

threshold is useful in order not to include low ice concentration areas where the fluxes depart significantly from their inner ice pack values.

The most obvious features in Fig. 4.3 are the strong seasonality and the stark contrast between the ice and open water/lead columns. Since at low temperature the seawater density is mostly determined by salinity, the buoyancy fluxes follow closely the seasonal cycles of salt fluxes. The intense ice formation rates in leads in winter lead to large buoyancy losses associated with brine rejections. These are at least one order of magnitude larger than below ice. In summer, the strong warming of open water by solar radiation yields positive buoyancy fluxes. These are however weaker than the fluxes existing under melting ice due to the freshwater input at the ocean surface. This is because ice lateral melt and runoff of meltwater from the ice to the open water are not implemented in the model.

Differences among ice categories also exist. In winter, thin ice grows more rapidly and therefore produces larger destabilizing salt fluxes. In summer, it loses its thinner insulating snow cover earlier, hence melting more rapidly. In the Arctic, penetration of solar radiation through thin ice categories also play a minor role in strengthening their positive buoyancy fluxes. The peculiar behavior of thickest ice categories in summer in the Arctic and in winter in the Antarctic is due to the porosity of ridges in LIM. Large amount of salty water are indeed entrapped when thick ice forms through ridging, and the subsequent brine drainage gives rise to large salt fluxes below the thickest ice.

In LIM, the ocean-ice stress is the same for all ice categories. As shown in Chapter 3, the surface stress is characterized by a much weaker seasonality than thermohaline fluxes, and does not differ much between the columns. Still, on average in the Arctic, it is up to twice larger in open water compared to ice. In the Antarctic on the other hand, the stress tends to be stronger below ice and differs by less than 15 % in the ice-free fraction of grid cells.

By influencing ocean and sea ice (see the next sections), the introduction of the MCO schemes implies feedbacks on the SBC variables, mostly on the thermohaline fluxes. It turns out that this results in only slight quantitative adjustments to the main picture described above, which remains fully valid. These are therefore considered as second order effects that will only briefly be addressed in the context of sea ice changes induced by MCO.

4.4.2 Ocean

The impacts of MCO on the ocean are presented in this section. We consider first the subgrid-scale processes, and then examine what influence they have on the mean fields.

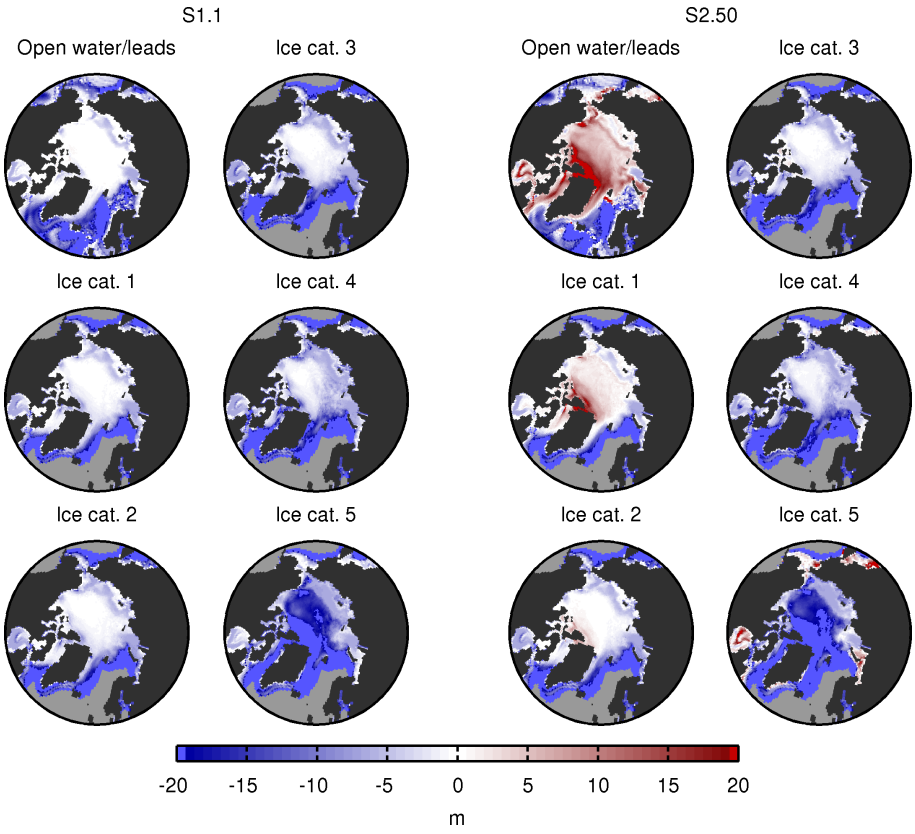

Figure 4.4: Difference between the convection depth in each oceanic column and the mean mixed layer depth, in experiments S1.1 (left) and S2.50 (right), for February in the Arctic and for August in the Antarctic.

4.4.2.1 Subgrid-scale processes

The difference between the depth of convection (CVD) in each column and the mean mixed layer depth (MLD) in winter is shown in Fig. 4.4. As its name implies, the CVD is the depth up to which the ocean column is homogenized by the NPC algorithm in order to remove static instabilities. A single MLD value is computed at each grid point from the mean density profile. It is defined in the model as the depth where the density is 0.01 kg m^{-3} higher than in the second level, at 10 m depth. The CVD - MLD difference maps are shown for February in the Arctic and for August in the Antarctic. This is just before the sea ice maximum, at a time when sea ice still forms in all regions but the ice edge and when the spread between subgrid-scale fluxes is the largest. Exper-

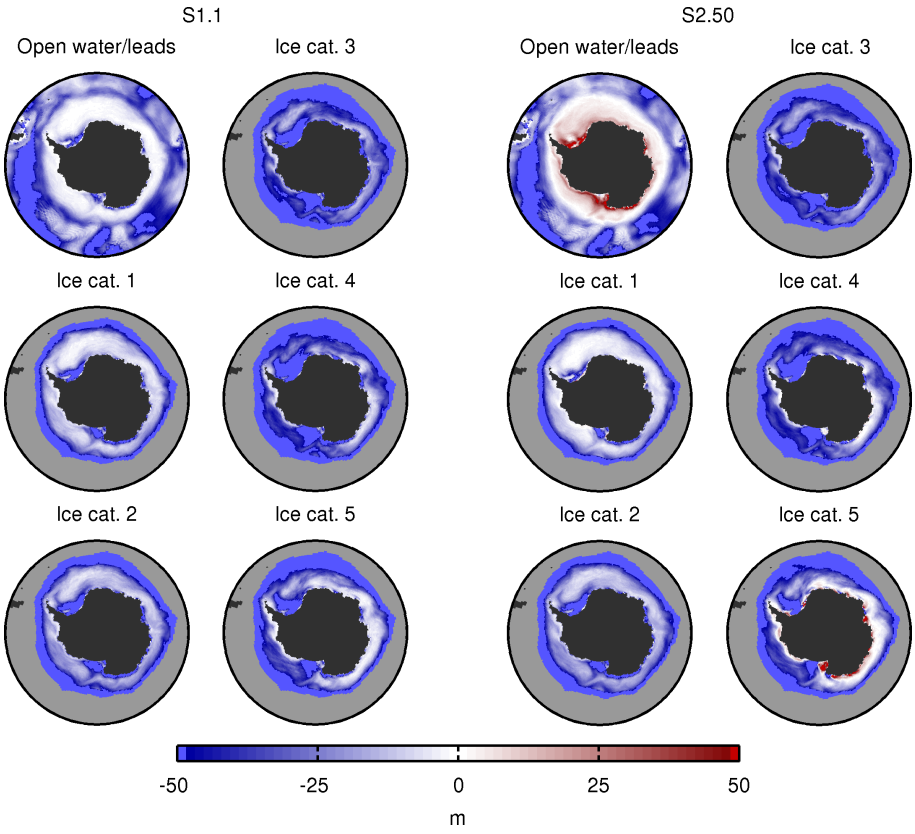

Figure 4.4: continued.

iments S1.1 and S2.50 are presented. This first one illustrates the effects of the MCO#1 scheme, while the second is used to exemplify a situation in which clear changes in the mean fields are obtained (see the next section).

In experiment S1.1, the deepest CVDs within the sea ice zone are close to the MLD, suggesting that convective mixing due to surface fluxes (mostly brine rejections) is a major process in the mixed layer deepening. Furthermore, a gradient in CVD exists among the columns, which is readily explained by the variability of ice growth rates, the latter being the most intense in leads and decreasing with increasing sea ice thickness. An exception is the fifth ice category in the Antarctic, whose concentration is nonetheless very low, due to brine drainage from ridges as explained above. The differences of CVD between the columns also occur because a finite, weak stratification may exist inside the mixed layer in the multi-column formalism. Indeed, whenever a

single ice category melts, the mean profile resulting from the averaging of one stratified column with others, possibly undergoing convection, will present a weak stratification close to the surface. Only the most intense brine rejections will generate enough instability to overcome this stratification. Convection shallower than the MLD occur in two other cases. First, in both hemispheres, the melting of ice advected towards warmer waters produces freshwater fluxes that inhibit convection, as is the case close to the ice edge. Second, in the Antarctic, the Ross and Weddell Seas are characterized by relatively small CVDs. In those regions, the very weak stratification at depth may however cause an overestimation of the MLD estimated using the density threshold method.

The MCO#2 scheme allows differences in temperature and in salinity between the columns to accumulate over several time steps. As a consequence, in experiment S2.50, convection is able to penetrate well below the mean MLD for the columns with the strongest surface fluxes. This includes in both hemispheres the column corresponding to leads, as well as the first (and to a lesser extent the second) sea ice category in the Arctic. The effect related to saline, newly formed ridges is again visible for the fifth category. In S2.50, north of Greenland and the Canadian Arctic Archipelago (CAA), convection in leads reaches depths more than 20 m larger than the mean MLD, while it can be up to 50 m in many coastal regions along Antarctica. Changes in MLDs compared to the reference experiment are smaller than these values (see Fig. 4.6). This means that the MCO#2 scheme allows, in at least a fraction of the grid cells, to entrain within the mixed layer waters from below, which would not have been put in contact with the surface otherwise.

The T/S profiles in each column are plotted in Fig. 4.5. The sole experiment S2.50 is considered here, since such profiles exist only in the MCO#2 scheme. Winter profiles are for the same months as in Fig. 4.4, while summer results are for July in the Northern Hemisphere (NH) and January in the Southern Hemisphere (SH), when the subgrid-scale fluxes are the most representative of the summer season.

The profile characteristics are fairly consistent for both hemispheres in each season. Expectedly, the most visible differences are between the open water/leads column and the ice ones. In winter, the column corresponding to leads is more saline in the mixed layer, by 0.25 PSU down to around 25 m in the Arctic and by 0.1 PSU down to 50 m in the Antarctic. This arises from additional salt input at the surface, as well as from entrainment of saltier water from below through deeper convection. A very slight salinity gradient also exists among ice categories in the NH. The effect of deeper convective mixing in leads has an impact on temperature profiles too. Vertical mixing of warmer water from below the mixed layer with cold surface water results in

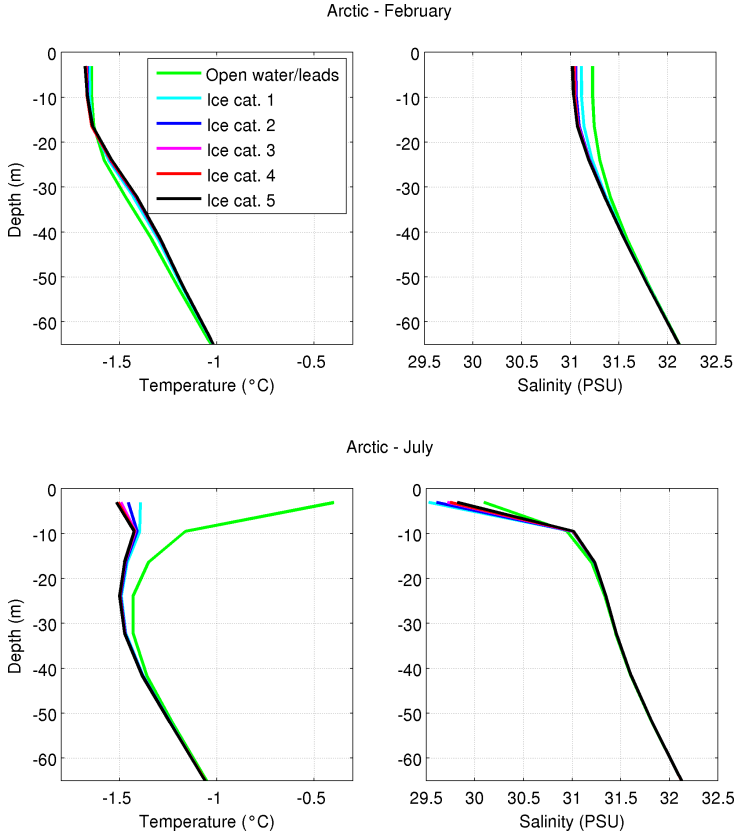

Figure 4.5: Temperature and salinity profiles in each oceanic column in experiment S2.50, averaged in the areas depicted in Fig. 4.2 and where sea ice concentration exceeds 15 %, for February and July in the Arctic and for January and August in the Antarctic.

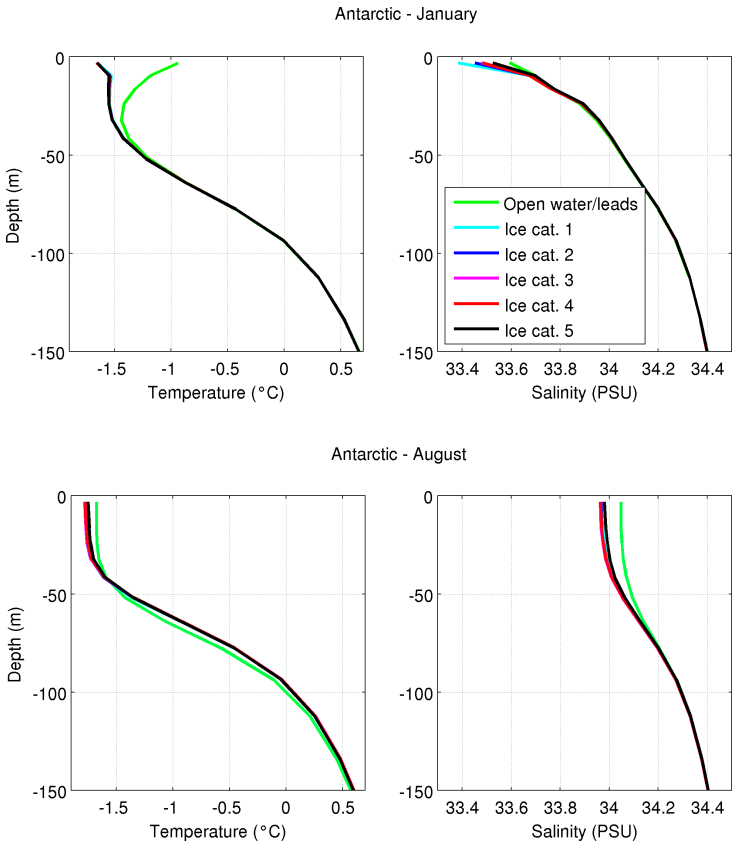

Figure 4.5: continued.

a increase (decrease) in temperature above (below) the MLD. Differences are nevertheless weak, of the order of 0.1 °C in the Antarctic and even smaller in the Arctic.

Summer profiles feature temperatures well above the freezing point in open water. The SST difference between open water and ice columns amounts on average to 1 °C in the NH and to 0.75 °C in the SH. This is caused by the absorption of around 150 W m^{-2} of solar energy in ice-free areas, only partly balanced by non-solar heat losses less than 20 W m^{-2} in the Arctic and less than 50 W m^{-2} in the Antarctic (Chapter 3). By contrast, the summer ocean-to-ice heat flux maintains the under-ice water close to the freezing point. Nevertheless, in the Arctic, the transmission of a fraction of incoming solar radiation through thin, snow-free ice leads to SST differences of up to a few tenths degrees between the thinnest and the thickest ice categories. This does not

happen in the Antarctic, because ice remains covered with snow during summer, which absorbs all solar energy in the model. Salinity profiles indicate that thin ice melts more rapidly, leading to a fresher ocean surface below the first categories. Differences are of the order of a few tenths PSU and are confined to the first few ocean levels. The highest SSSs are encountered in open water. This contrasts with the examination of SHEBA data by Holland (2003), which showed the surface of the lead to be several PSU fresher than the under-ice. Absence of explicit lateral melt and of meltwater runoff from the ice surface in LIM are responsible for this discrepancy.

An equivalent of Fig 4.4 for the summer season would show the same absence of convection in all columns. Fig. 4.5 indicates however that distinct situations occur in open water and below ice. On the one hand, melting ice has a cooling but freshening effect on the ocean surface. On the other hand, the open water undergoes little salinity changes from surface fluxes, but warms due to the absorption of solar radiation. In both cases, the water columns become stable and vertical mixing is hampered.

4.4.2.2 Effects on mean fields

In this section we determine whether MCO has an impact on the ocean mean state, beyond the subgrid-scale effects described above. MLDs could be affected in two ways. First, the application of destabilizing surface fluxes in a limited part of the grid cells, and the fact that the average of unstratified and stratified profiles is stratified, could lead to a reduction in MLDs. Besides, the deeper convection in some columns could weaken the stratification below the MLD compared to the reference experiment, which could permit a greater penetration of turbulent mixing and an increase in MLDs. As will be shown here and in agreement with previous studies (Ilıcak et al., 2014; Jin et al., 2015), the first effect is in general dominant in winter.

In the NH, the simulated MLDs are compared with the global upper ocean MIMOC climatology (Monthly Isopycnal and Mixed layer Ocean Climatology, Schmidtko et al., 2013). This product is based on individual conductivity-temperature-depth (CTD) profiles from traditional shipboard data, but also from automated ice-tethered profilers, which provide upper ocean observations of the ice-covered Arctic region in all seasons (Krishfield et al., 2008). As shown in Fig. 4.6, experiment REF reproduces relatively well the MLDs in the Arctic Ocean in winter. The main biases compared to the climatology are too deep MLDs in areas around Greenland, in Hudson Bay and in the Sea of Okhotsk, and a slight underestimation of MLDs in the Canada Basin.

On average in the Arctic area chosen for analysis (Fig. 4.2), the maximum monthly MLD in MIMOC is 34 m. The corresponding values for all simula-

Table 4.3: Monthly maximum of the average mixed layer depth in the areas depicted in Fig. 4.2 and sea ice extent and volume monthly extrema, in the reference and sensitivity experiments, in the Arctic (upper part) and in the Antarctic (lower part). The numbers in brackets indicate the differences compared to the reference experiment.

Experiment	REF	S1.1	S2.2	S2.10	S2.50	S2.250
Arctic						
Max. MLD (m)	34	34 (0)	35 (1)	35 (1)	33 (-1)	29 (-5)
Min. extent (10^6 km^2)	7.0	7.0 (0.0)	7.0 (0.0)	7.2 (0.2)	7.7 (0.7)	8.5 (1.5)
Max. extent (10^6 km^2)	16.8	16.8 (0.0)	16.8 (0.0)	16.8 (0.0)	16.9 (0.1)	17.0 (0.2)
Min. volume (10^3 km^3)	14.7	14.7 (0.0)	14.8 (0.1)	15.2 (0.5)	16.8 (2.1)	19.3 (4.6)
Max. volume (10^3 km^3)	30.8	30.8 (0.0)	30.9 (0.1)	31.1 (0.3)	32.0 (1.2)	33.3 (2.5)
Antarctic						
Max. MLD (m)	79	78 (-1)	78 (-1)	76 (-3)	73 (-6)	69 (-10)
Min. extent (10^6 km^2)	8.0	8.0 (0.0)	8.1 (0.1)	8.4 (0.4)	9.6 (1.6)	11.4 (3.4)
Max. extent (10^6 km^2)	20.9	20.9 (0.0)	20.9 (0.0)	21.0 (0.1)	21.1 (0.2)	21.2 (0.3)
Min. volume (10^3 km^3)	5.6	5.6 (0.0)	5.6 (0.0)	5.8 (0.2)	6.6 (1.0)	7.6 (2.0)
Max. volume (10^3 km^3)	16.6	16.6 (0.0)	16.6 (0.0)	16.7 (0.1)	16.8 (0.2)	16.9 (0.3)

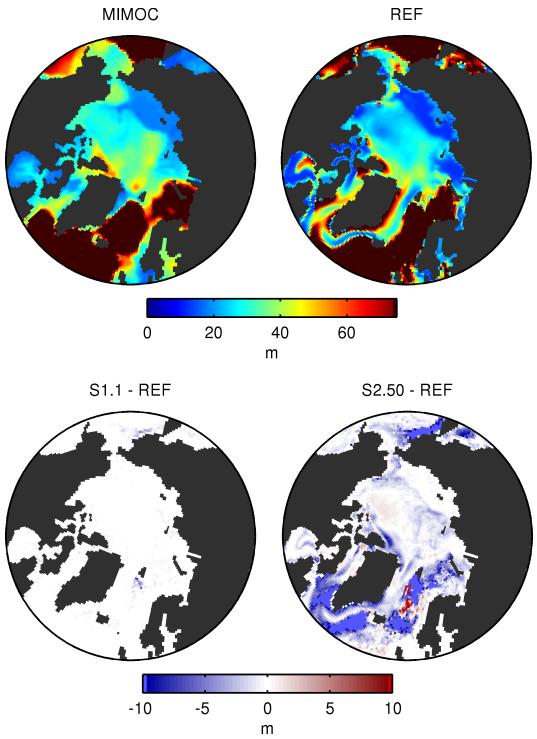

Figure 4.6: Mixed layer depths in the MIMOC climatology and in experiment REF, and differences with experiments S1.1 and S2.50, for February in the Arctic and for August in the Antarctic.

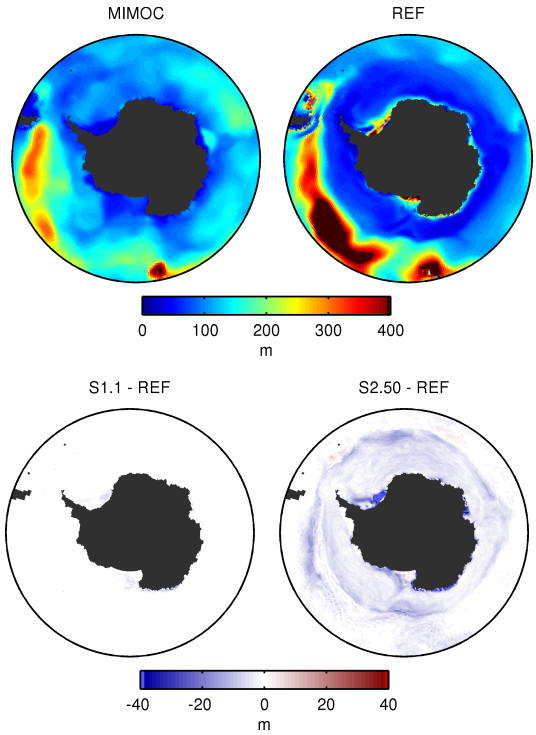

Figure 4.6: continued.

tions are listed in Table 4.3. The good agreement with REF is noticeable. The mean impact of MCO is weak, except for simulation S2.250 which exhibits a maximum MLD reduction of 5 m. The small changes in that mean value could result from the spatial averaging, but as far as experiment S1.1 is concerned, Fig. 4.6 shows that MCO#1 has indeed nearly no impact. In S2.50 on the contrary, MLDs generally decrease in the sea ice zone, up to 10 m north of Greenland, but they show a tenuous increase in the Canada Basin. However, the changes are too small to offset the initial model biases. The largest differences actually occur beyond the sea ice edge, in regions of much deeper MLDs, likely because of weak modifications in the large-scale T/S fields.

Due to the lack of under-ice winter hydrographic observations close to Antarctica, the MIMOC climatology severely underestimates MLDs on the continental shelves (Chapter 2). Besides, measurements collected between 2004 and 2011 by CTD sensors carried by seals provide an extremely valuable source of information about the hydrography of the Southern Ocean south of the Antarctic Circumpolar Current. We thus use here the MEOP-CTD dataset

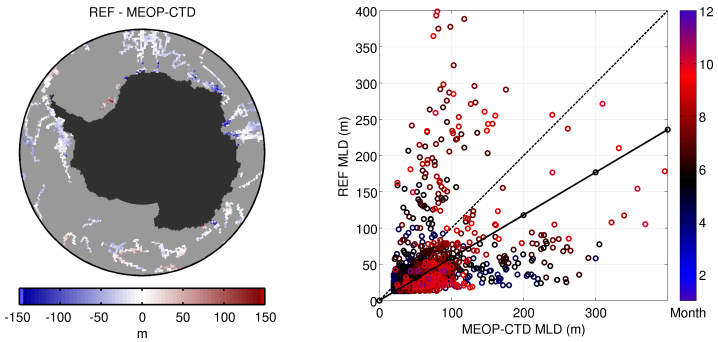

Figure 4.7: Comparison of mixed layer depths in the MEOP-CTD dataset and in experiment REF, for the period 2004-2011. Left: mixed layer depths difference in May. Right: scatter plot of simulated versus observed mixed layers depths in the Antarctic area depicted in Fig. 4.2; the solid line is a least squares linear fit and the dashed line is the diagonal.

(Marine Mammals Exploring the Oceans Pole to Pole, Roquet et al., 2011, 2013), a calibrated compilation of T/S profiles collected by hundreds of instrumented seals, to evaluate our model results. In short, climatological MLDs are obtained from the database by averaging, for each month and each ORCA1 grid point where they are available, the MLDs computed from the measured profiles in the same way as they are estimated in NEMO. More details about the model-data comparison can be found in Chapter 2. Out of the continental shelves, the MLDs from MIMOC compare quite well with the ones calculated from seal observations. Hence, the following analysis is only based on the latter.

MLDs in experiment REF are evaluated against MEOP-CTD estimates in Fig. 4.7. The map of differences is shown for the month of May, when mixed layers become deeper and when the data coverage is still relatively good. Overall, the model tends to underestimate MLDs. The issue is clearest along the coast of East Antarctica, where the bias is locally up to 150 m. The only location where significantly too deep mixed layers are modeled is the eastern Weddell Sea. The scatter plot extends the evaluation to all months and corroborates the above finding. Weddell Sea data points are clustered above the diagonal. The correlation between simulated and observed MLDs is 0.38 and the slope of the least square linear fit is 0.59, confirming the MLD underestimation by the reference experiment.

As in the NH, the introduction of MCO schemes in NEMO reduces MLDs in the Antarctic, with a larger impact for longer homogenization time scales. On average, the MLD drops from 79 m in REF to 73 m in S2.50 (Table 4.3),

whereas the changes are barely visible for S1.1 (Fig. 4.6). The decreases in MLD appear more restricted to the ice-covered areas than in the Arctic. The largest changes, of the order of 50 m in experiment S2.50, occur on the continental shelves, except in the Ross Sea. A comparison of S2.50 with the MEOP-CTD dataset yields a correlation coefficient of 0.41 and a linear fit slope of 0.54. This is consistent with a small improvement in the mean MLD representation where measurements exist in the Weddell Sea, but with an exacerbated underestimation elsewhere. The equivalent of Fig. 4.7 for this experiment looks very similar to the one displayed for REF and is thus not shown. Since the MEOP-CTD profiles are recorded during the quasi-vertical ascent of seals, it is possible that the animals oversample the lead areas. Because of the large differences in the depth of convection between the columns in MCO#2, such a non-uniform sampling could have an influence on the model-observation comparison.

The MCO effects on mean T/S fields are presented in Fig. 4.8. They are negligible in S1.1 and small in all other simulations, so that the general shape and properties of profiles remain mostly unaffected. Therefore, the differences compared to the reference experiment are plotted, for the winter season. In summer in both hemispheres, the most consistent signal is an increase in SSS (not shown) that we attribute to a reduced sea ice melt (see the next section).

In the Antarctic, the temperature and salinity increase at a depth close to the MLD, with magnitude depending of the homogenization time scale. This is consistent with a shoaling of the mixed layer, which allows the warmer and saltier water from below to get closer to the surface. The maximum warming and salinity gain are of 0.1 °C and 0.02 PSU in experiment S2.50. The temperature profiles also indicate a slight cooling at depth, which is explained by a greater penetration of cold water due to deeper convection in leads. At the surface, the presence of sea ice forces temperatures to remain at the freezing point in all simulations.

In the Arctic, even qualitatively, the results depend much on the mixing time scale. For experiments S2.2 and S2.10, only a weak cooling is present down to 150 m. A warming in the upper layer, associated to a MLD shoaling or to the entrainment of water from below, exists exclusively in S2.50 and S2.250. The temperature differences at greater depths (below 150 m) likely originates from changes in vertical mixing in remote areas, with impacts on deep water masses. By all means, the changes are minimal, being at maximum of the order of 0.02 °C in experiment S2.50. Salinity profiles show the same variety of behaviors, with a consistent increase close to the surface but with a freshening below the mixed layer only in S2.2 and S2.10.

The MCO impacts on MLDs and on mean T/S profiles may appear weak, especially in comparison to the subgrid-scale effects presented in the previous

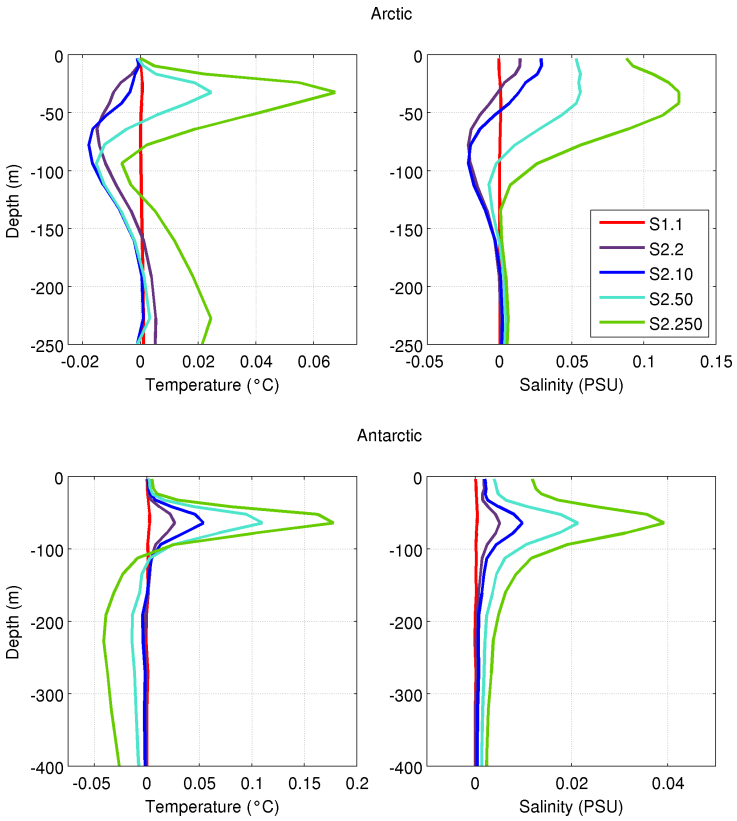

Figure 4.8: Differences in temperature and salinity profiles between the sensitivity and REF experiments, averaged in the areas depicted in Fig. 4.2, for February in the Arctic (upper panels) and for August in the Antarctic (lower panels).

section. This is because some of the subgrid-scale processes occur in columns of very small extent. The most meaningful example is winter leads, whose vertical mixing and hydrography are so peculiar. Their average concentration in the model falls to less than 0.03 % in February in the Arctic and to less than 0.5 % in August in the Antarctic. A higher and more realistic simulated open water fraction would strengthen the effects of MCO, by increasing the area of the column with the strongest buoyancy fluxes and the deepest convection. Additionally, the mean profiles considered so far mask regional changes that are larger in magnitude. Spatial distributions of temperature and salinity differences at 190 m between experiments S2.50 and REF are shown in Fig. 4.9 for August in the Antarctic. While changes close to the surface are relatively uniform (not shown), complicated patterns exist at depth due to heterogeneities

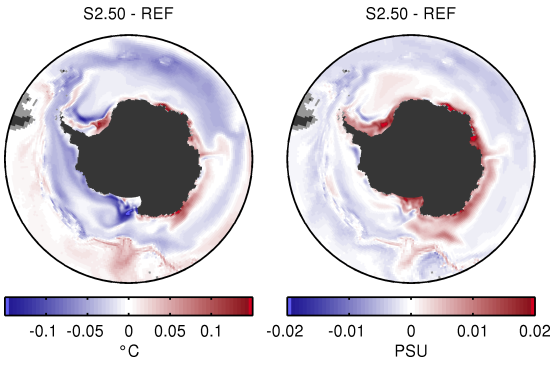

Figure 4.9: Differences in temperature (left) and salinity (right) at 190 m depth between experiments S2.50 and REF, for August in the Antarctic.

in the MLD. The mean difference plotted in Fig. 4.8 is therefore not representative of all regions.

Especially in the Ross Sea, the cooling effect of MCO below the MLD is clear, reaching up to 0.15 °C for the waters exiting the continental shelf. In the Weddell Sea, higher temperatures are found close to the ice shelf where the mixed layer is deeper than 190 m, while colder waters occupy the other areas. This is consistent with the one-dimensional effect described above based on mean profiles. In absolute values, maximum differences are of the order of 0.15 °C as well. Along the coast of East Antarctica, waters at 190 m depth are warmer in S2.50 than in REF, which cannot always be explained by deep MLDs as in the Weddell Sea. At 1° resolution, we do not expect an accurate representation of the coastal currents. Nonetheless, changes in the zonal ocean velocity (not shown) are a possible reason for the different model response in that region. The salinity presents a more uniform increase along the continent, up to 0.02 PSU in the three areas discussed above. These changes induced by MCO are non-negligible when compared to the simulated interannual variability at this depth around Antarctica, which is measured as the standard deviation and is of the order of 0.3 °C for temperature and 0.05 PSU for salinity. They are also significant when put into perspective with observed decadal variations in the temperature of bottom water masses in the Weddell Sea for example, which occur at rates close to 0.01 °C year^{-1} (e.g., Fahrbach et al., 2004; Couldrey et al., 2013).

4.4.3 Sea ice

The impacts of the MCO schemes on the sea ice cover are now investigated. Maximum and minimum monthly ice extents and volumes are given for all sensitivity experiments in Table 4.3. The overall effect of MCO is to increase the ice extent and volume, mostly at the seasonal minimum. It is weak for homogenization time scale equal or shorter than 10 h, but becomes substantial for S2.50 and S2.250. In those simulations, the minimum sea ice extent rises by around 1 10^6 km^2 in the Arctic. The increase is even larger in the SH, but given the positive summer bias in Antarctic sea ice, the model results should be treated with caution. In both hemispheres, the extent is only marginally affected at the winter maximum. The Arctic sea ice volume changes are similarly at their highest during summer, reaching for instance 2.1 10^3 km^3 for experiment S2.50, but approximately half of the signal persists during winter. In the Antarctic, differences in volume occur mainly at the sea ice minimum and amount to 1.0 10^3 km^3 for S2.50.

Maps of sea ice concentration and thickness are shown in Fig. 4.10, for experiments REF and S2.50, which is the first in which MCO has significant effects, and for the months of February and August when the differences with respect to the reference simulation are the largest. The average sea ice thickness over the whole grid cell is plotted, i.e. sea ice 1 m thick at 50 % concentration appears as 0.5 m thick in the figure. In other words, it corresponds to the sea ice volume per unit area.

Sea ice concentration increases preferentially in peripheral areas where it is low, whereas it is almost unchanged in the central Arctic basin and CAA, and in the Weddell Sea. Differences are typically of the order of 10 %, but exceed 15 % locally. The gains in ice thickness tend to be more widespread. In the Arctic, ice gets 15 cm thicker almost everywhere and the increase is up to 30 cm in the marginal ice zone. The thickening is at most 15 cm in the Antarctic. Although the magnitude of the changes varies from one sensitivity experiment to the other, the general patterns remain the same in all cases.

In order to understand the origin of the sea ice changes described so far, we examine the non-solar part of the oceanic surface heat flux in experiments REF and S2.50 (Fig. 4.11). In the ice-covered columns, this corresponds practically to the heat transferred from the ocean to the ice base. In current ocean-sea ice models, and in our reference simulation in particular, the oceanic heat flux is common to all ice categories. With MCO#2, it can vary from one category to another one, according to the specific ocean conditions underneath.

Considering first the subgrid-scale distribution in S2.50, Fig. 4.11 shows that the heat flux at the ice base tends to be larger for thinner ice. In the Antarctic, the differences are limited to the winter season and are of the or-

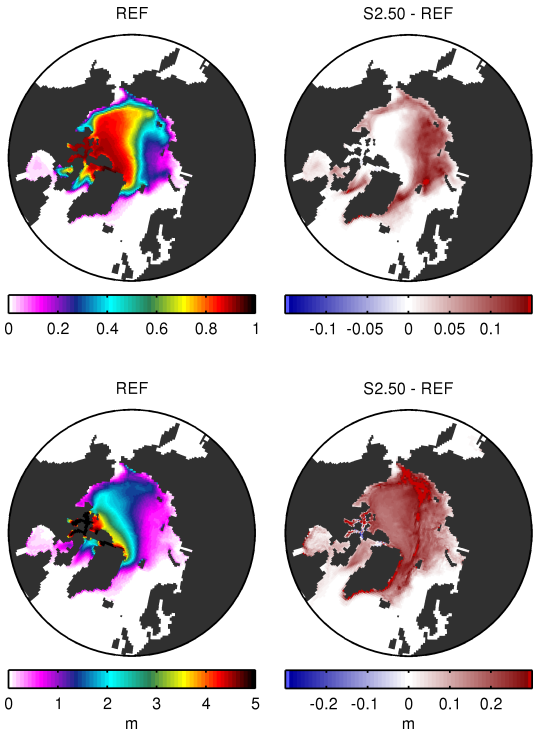

Figure 4.10: Sea ice concentration (upper panels) and mean thickness (lower panels) in experiment REF, and differences with experiment S2.50, for August in the Arctic and for February in the Antarctic.

der of 5 W m^{-2} between the first and the third and fourth categories, which is roughly 30 % in relative terms. The highest fluxes are caused by enhanced vertical mixing that brings more oceanic heat to the surface. With its large salt fluxes resulting from brine drainage, the fifth category behaves in a similar way as the first. The same processes occur in winter in the Arctic as well, where the heat flux below the thinnest ice is more than twice as high as below the thickest category. However, in contrast to the SH, the fluxes are also heterogeneous in summer. At the maximum in August, the first, the second and the other categories undergo fluxes of 27, 22 and around 20 W m^{-2}, respectively. This arises from differential penetration of solar radiation for the different ice classes. On average, a maximum difference of 15 W m^{-2} in the amount of energy reaching the ice-ocean interface indeed exists between the first two categories (Chapter 3). The lateral mixing between the columns and

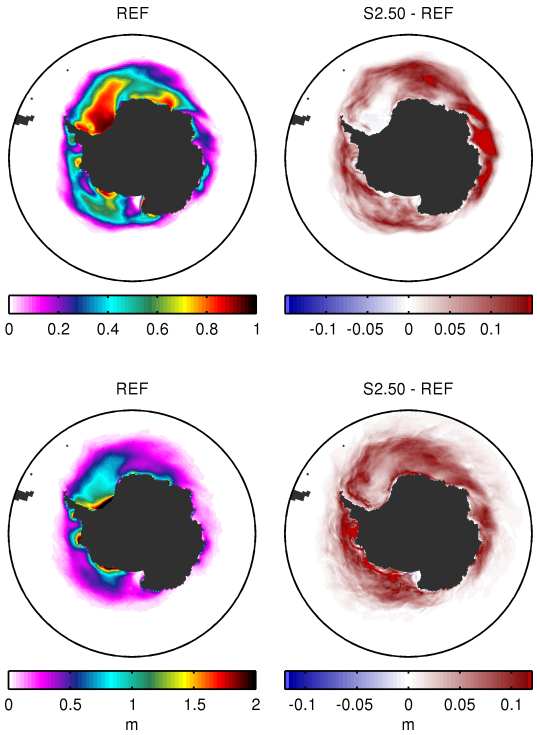

Figure 4.10: continued.

the penetration of shortwave radiation inside the ocean imply that only a third of this difference is reflected in the oceanic heat fluxes to the ice.

Comparing the oceanic heat fluxes between experiments REF and S2.50 is also of interest. During winter in both hemispheres, the REF curve tend to follow the S2.50 curve corresponding to the category in which most ice lies (third in the NH and second in the SH), suggesting modest differences between both simulations. In summer the signal is clear nonetheless: the fluxes in the MCO experiment are systematically lower than in the reference simulation. The difference is between 5 and 10 W m^{-2} in the Arctic on average, but reaches as much as 15 W m^{-2} in the Antarctic. The main source of heat to the ocean in summer is the warming by solar radiation, which is maximum in open water. Without an MCO scheme, the absorbed energy is immediately spread over the whole grid cell. When MCO#2 is activated, the warming is concentrated in the open water column. It reaches the under-ice only thanks to the column homogenization, which is controlled by the mixing parameter f_{mix}. This explains the lower ocean-to-ice heat fluxes, and consequently the reduced sea

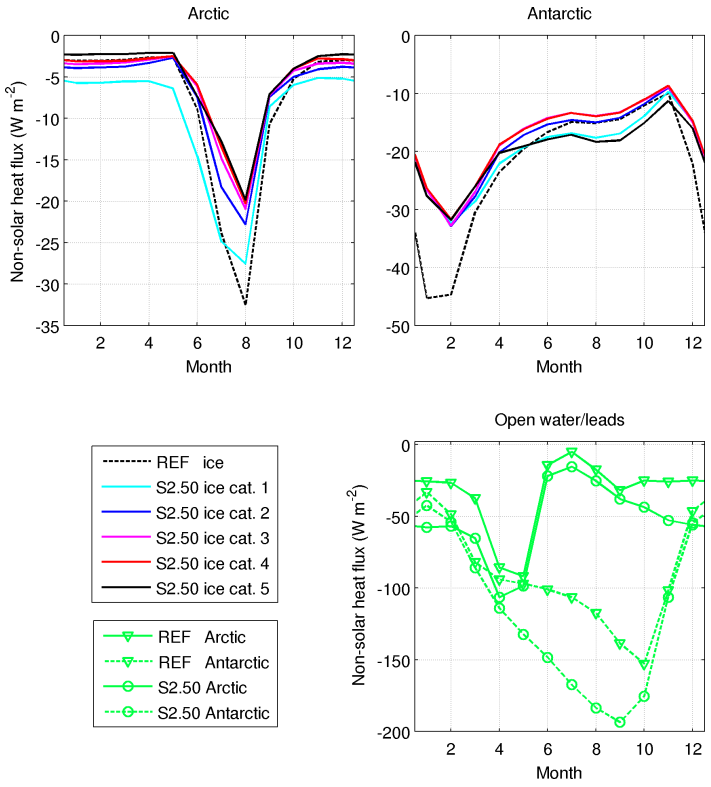

Figure 4.11: Seasonal cycles of non-solar heat flux at the ocean surface under ice (upper panels) and in open water/leads (lower panel) in experiments REF and S2.50. The spatial averages are computed in the areas depicted in Fig. 4.2 and where sea ice concentration exceeds 15 %.

ice melt. This process also explains that the differences between MCO#2 and REF are the largest where concentration is low, because it is where the amount of solar energy entering the ocean is the highest.

Also shown in Fig. 4.11 are the non-solar heat fluxes at the surface of open water/leads. When sea ice forms, this is actually not the total heat loss to the atmosphere, but rather the flux needed to maintain the ocean close to the freezing point. The additional term corresponding to the heat losses associated with the freezing of seawater has no impact on the SST. This is the reason why it is not included in this diagnostics. Focusing on the surface boundary condition for the ocean, the changes between experiments with or without MCO are substantial. The heat losses are higher in winter because deeper convection in leads brings more heat to the surface and in summer because

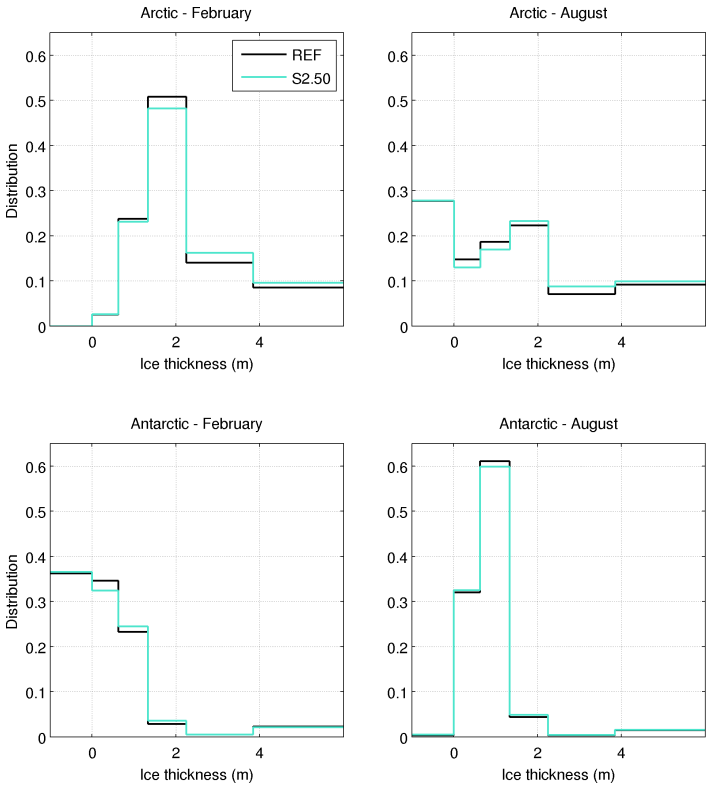

Figure 4.12: Ice thickness distribution in experiments REF and S2.50, averaged in the areas depicted in Fig. 4.2 and where sea ice concentration exceeds 15 %, for February and August in the Arctic and Antarctic. The value given for negative thicknesses represents the open water/lead fraction.

the SST is higher in open water following solar warming. The differences can reach several tens of W m^{-2} on average.

Given the high subgrid-scale variability of oceanic heat fluxes with MCO#2, one may expect changes in the simulated ITD. The average concentration in each category and the open water/lead fraction are presented in Fig. 4.12 for winter and summer months, in the areas delineated in Fig. 4.2 and for simulations REF and S2.50. The mean ice thickness in a given category differs much less between the two experiments than its concentration, and is hence not shown in the figure. Although the differences are qualitatively well explained by the heterogeneity of heat fluxes discussed above, it turns out that MCO has quantitatively little influence on the ITD. The concentration of thick categories tend to increase, at the expense of the thinner ones that undergo

higher heat fluxes, but the changes are at most a few percent. Attempts to evaluate the modeled ITD against observations have shown errors up to 20 % for some ice classes (Chapter 3), i.e. much larger than the differences between the experiments analyzed here.

4.4.4 Discussion

The analysis of model results in the previous sections has shown their high sensitivity to the homogenization time scale between the columns. In MCO#1, in which complete homogenization takes place at each time step, i.e. every hour in our configuration, some effects exist at the subgrid scale but the model mean state is practically unchanged. This indicates that the heterogeneity in surface fluxes due to the presence of sea ice is not sufficient to induce, over one hour, very different oceanic regimes among the columns. A scheme like MCO#2 is therefore required to test the model sensitivity to a possible shift between the columns that grows over a longer period, corresponding to several time steps. Another strong motivation for MCO#2 is its ability to decouple the homogenization time scale from the model time step, in case MCO principles would have to be tested in different configurations.

Among the MCO#2 sensitivity experiments, it appears that impacts are relatively weak for homogenization time scales up to 10 h in our setup, but that they become substantial for longer values. Physically, the effects on the mean fields start to occur in winter when the convection reaches depths greater than the MLD in some of the columns. This process indeed allows waters from below, whose properties differ significantly from the surface, to be entrained within the mixed layer. While no convection occurs in summer, large-scale changes in sea ice emerge when the homogenization is sufficiently slow to let the solar radiation absorbed in open water be stored in the corresponding column, thereby delaying its influence on the ice melt.

Since quantitatively the MCO impact strongly depends on how fast the columns are homogenized, a physical estimation of the mixing time scale would be highly valuable. This is however a complex problem, which is beyond the scope of the present study. The mixing between columns is very likely variable in both space and time, depending first on their spatial distribution and second on the ocean and ice dynamics.

The column distribution is related to the size of ice floes of different thicknesses and to how they are spread at the ocean surface. In a summer situation where small floes are evenly distributed among areas of open water, differences in water properties could be limited to a very thin layer close to the ice-ocean interface, while at greater depths, the large contact area between the columns would prevent distinct ocean regimes. By contrast, in a polynya

in which sea ice is blown away from the coast by winds, there may exist a clear distinction between the ice-free portion of the area and the portion where thicker ice accumulates, allowing separate ocean columns to develop. The floe size distribution has long been recognized crucial for processes such as lateral melting (e.g., Steele, 1992). Its explicit modeling is nevertheless just starting to be considered for inclusion in large-scale operational forecast or climate models (Zhang et al., 2015; Horvat and Tziperman, 2015), which is promising for the current application. In the same vein, a representation of the lead width distribution could be important, as turbulent fluxes show a dependence on the size of leads (Marcq and Weiss, 2012).

The second factor that could influence the mixing of ocean columns is the ice-ocean relative velocities. If they are large, the heterogeneous surface fluxes are not continuously applied on the same fractions of the water column. For instance, a 300 m wide ice floe drifting at 10 cm s^{-1} needs less than one hour to be moved away from the region it was initially occupying and thus to cover another portion of the ocean surface. The model results indicate that such relative velocities are often encountered inside the Antarctic ice pack, while the ice drift tends to be slower in the Arctic (not shown). Besides, the ice motion induces vertical shear and turbulent mixing in the upper layers of the ocean (Morison et al., 1992; Smith and Morison, 1993; Kantha, 1995; Skyllingstad and Denbo, 2001), that tend to homogenize the oceanic columns quickly. Low relative velocities may thus be even more critical than the distribution of ice floes in allowing large differences between the columns.

Although the discussion presented above is only qualitative, we suspect that the homogenization time scale of 50 h used in experiment S2.50 might be a high value in most conditions. The effects that we have examined in more details in that simulation must hence probably be considered as an upper limit for the impacts of a subgrid-scale representation of ice-ocean interactions. Experiment S2.250 should even more clearly be seen as an idealized test case.

A direct estimation of the homogenization time scale from observations would be extremely difficult to obtain. The needed data would include repeated and simultaneous CTD profiles performed under different types of ice and in leads in a given area, in both the freezing and melting seasons, and for different ice-ocean relative velocity regimes. This would have to be compared to idealized, detailed processes studies in a model, in order to determine the horizontal mixing rate that gives the best agreement with observations. Parameter estimation based on data assimilation could provide an alternative (e.g., Massonnet et al., 2014). Given its impact on MLDs, the homogenization time scale could be optimally estimated from the assimilation of under-ice hydrographic measurements. The obtained results could then guide the development of empirical parameterizations for use in simulations without assim-

ilation. Large eddy simulations of the sea ice-ocean system might be another method to study the processes that modulate the horizontal mixing between the oceanic columns.

Other model features play a role in our estimation of MCO effects. In addition to the uncertainty on the mixing time scale, the open water fraction and the particular concentrations of ice of different thicknesses provided by the ITD display clear biases, that have a significant influence on the quantitative impact of MCO in our experiments. A short examination of the LIM results against IceBridge datasets (Kurtz et al., 2013) has actually demonstrated errors locally up to 20 % in the areal fractions of given ice categories. Compared to passive microwave satellite products, it also appears that the model underestimates the amount of leads in winter (Chapter 3).

A further issue regarding an accurate simulation of open water in summer is the lack of explicit lateral melt in LIM, whose adequate implementation is conditioned upon a representation of the ice floe size distribution (Steele, 1992). Although it is implicitly accounted for through melt of thin ice in the ITD (Bitz et al., 2001), it does not constitute a source of freshwater at the top of the ice-free column, as it should be. The runoff from snow and surface ice melt is a problem as well. Finally, Holland (2003) note that to achieve a realistic representation of summer warming and freshening of the open water surface, the latter must be embedded within the ice cover, in order to hinder direct lateral mixing between the lead and the under-ice ocean system. This is in line with the modeling results of Skyllingstad et al. (2005). However, it raises technical difficulties in a full three-dimensional model and has not been addressed here.

4.5 Conclusions

The sensitivity study presented in this chapter intended to examine the effects of a representation of the heterogeneous nature of ocean-sea ice interactions in the global model NEMO-LIM. A multi-column ocean scheme has been developed, in which the subgrid-scale surface boundary conditions related to the ice thickness distribution present in LIM can be explicitly taken into account. While convection is always computed separately in open water and under the ice categories, whether distinct temperature and salinity profiles are allowed to be maintained over several time steps dictates if the model turbulent mixing scheme has to be called individually in each column as well. This distinction gives rise to two scheme versions that differ significantly in complexity. Nonetheless, model computations relative to ocean dynamics and lateral mixing are unmodified in both cases.

Although it requires substantial modifications in the model, the multi-column ocean scheme consists mostly in repeating several times the vertical mixing and tracer update computations that are already done in the reference code. Since the TKE and NPC schemes are time-consuming portions of the code, our developments significantly increase the model integration time. MCO#1 and MCO#2 are respectively 1.4 and 2.2 times more demanding in CPU time than the reference simulation. Optimization has not been a major concern so far, but it is clear that both versions could benefit from reducing the number of columns, possibly focusing on open water and thin and thick ice classes only. Reducing the amount of output fields in MCO#2 would be another simple source of performance improvement. Finally, the memory use is also larger with MCO#2 due to several additional three-dimensional fields that exist for all six columns (temperature, salinity, turbulent kinetic energy and turbulent mixing coefficients).

By using the actual buoyancy fluxes and column areas provided by the sea ice model, if lateral mixing occurs at each time step, there exists subgrid-scale effects in ocean convection but large-scale impacts on the model mean state are practically nonexistent. One option to artificially amplify the effect of subgrid-scale fluxes is to apply the salt rejections in a column of arbitrarily small extent as in Jin et al. (2015). We rather chose to maintain the columns over several time steps. By doing so, we obtained a number of physically plausible effects. The major ones are a reduction in mixed layer depths and an increase in sea ice extent and volume at the seasonal minimum, themselves explained by decreases in the oceanic heat flux at the ice base. Mean temperature and salinity profiles are only weakly affected. Nevertheless, in the Antarctic, changes of up to 0.15 °C and 0.02 PSU are found at a few hundreds meters depth in the Ross and Weddell Seas and along the coast of East Antarctica, which are key areas for the formation of bottom waters. The length of our model runs is however too short to evaluate the long-term effects of MCO on these water masses. In the particular configuration used in our analysis, the multi-column ocean scheme causes the model to underestimate mixed layer depths, mostly in the Antarctic, and exacerbates the positive summer ice bias. The increase in Southern Hemisphere summer sea ice would actually be beneficial with other setups and forcing formulations, in which the Antarctic minimum extent is often too low (e.g., Rousset et al., 2015).

We noted that significant effects on the ocean and sea ice start to appear when the time scale of homogenization between the columns is of the order or larger than 10 h. The large sensitivity to this time scale implies that additional work is required to estimate the lateral mixing rate from a strong physical basis, and thereby to reach a robust implementation of the multi-column ocean scheme and an precise quantitative evaluation of its impact. This is dependent

on several other model features, among which an accurate representation of the ice thickness distribution and of the open water fraction, floe size distribution, lateral melting, runoff from the ice and embedment of leads within the sea ice cover. Those are all topics which deserve additional research and developments. Studying the impacts of the multi-column ocean scheme in atmosphere-ice-ocean coupled simulations, or with models including a representation of the biogeochemistry (e.g., Long et al., 2015), would be of high interest as well.

CHAPTER 5

CONCLUSIONS

The main outcome of this thesis is a better understanding of **small-scale, heterogeneous sea ice-ocean interactions** and of how they can be **represented in large-scale models**. To this end, a series of schemes of increasing complexity have been developed, implemented and tested in the global ocean and sea ice model NEMO-LIM. In this last chapter, we review the scientific questions that were raised in the introduction of this work and sum up how we have contributed to answer them. We also address the limitations of our approach and present perspectives and future work.

5.1 Contributions of the thesis

5.1.1 Heterogeneous sea ice-ocean interactions

The first question that we aimed answering was: **"What small-scale sea ice-ocean processes are at play under an heterogeneous ice cover?"**. We briefly recall here the main processes that our analyses have revealed. They all originate from the small-scale spatial variability of sea ice properties, and from the pronounced influence ice has on the underlying ocean.

In the cold and relatively fresh polar oceans, the surface fluxes of buoyancy are largely determined by the freshwater and salt fluxes. The latter are, in turn, strongly influenced by the formation and melt of sea ice. These processes are

associated with brine rejections and inputs of nearly fresh meltwater, respectively. In winter, larger freezing rates are found for thinner ice which supports larger thermal conductive fluxes. Thin ice is also usually covered with less insulating snow, strengthening this effect. The related destabilizing salt fluxes result in more intense convective mixing in thin ice areas. Under-ice mixing determines the vertical transfer of heat from the ocean subsurface to the ice base. This heat may originate from the surface waters warmed by summer solar radiation. It can come from deeper warm water masses as well, especially in the Antarctic. We have shown that only the most intense brine rejections are able to generate convection strong enough as to penetrate below the mixed layer and to reach those water masses, thereby having a clear impact on the mixed layer heat budget. In summer, a spatial variability exists in buoyancy fluxes too, since thin ice melts faster because of its lower albedo.

In our analysis, expectedly, the largest winter differences in the vertical mixing processes described above occur between the ice-free and ice-covered areas. Compared to the under-ice, new ice growth is larger by more than one order of magnitude in leads and polynyas, where no consolidated ice cover insulates the ocean from the cold atmosphere above. Field observations and numerical studies have however shown that localized brine rejections in a slowly-moving lead result in a peculiar response of the upper ocean. Instead of leading to convective mixing and a deep homogenization of the water column, these brines form plumes of salty water that sink towards the bottom of the mixed layer, making it shallower and more stratified. The representation of this process requires a particular treatment, which is further discussed in the next sections.

The heterogeneity of the summer warming of surface waters by solar radiation also has interesting consequences. Most of the energy is provided through open waters, making them warmer than the ice-ocean interface, which is constrained to remain close to the freezing point. Besides, our results have shown that the influence of the energy absorbed in open water on the ice bottom melting depends directly on the horizontal transfer of heat from the ice-free areas to the ice-covered ones. Finally, the transfer of a fraction of the incident solar radiation through thin, snow-free ice induces a thickness dependence of the oceanic heat flux at the ice base. This occurs mostly in the Arctic and can enhance the ice-albedo feedback through a faster melt of thinner ice.

The input of mechanical energy at the ocean surface differs according to the presence or absence of sea ice. Without ice, the wind stress generates directly turbulent mixing in the upper ocean layer. With ice, this stress is replaced by the drag resulting from the relative motion between the uneven under-ice surface and the water. In our model, a constant drag coefficient is used, implying that the ice-ocean stress does not depend on the ice type. Fur-

thermore, it appears in our simulation results that the energy input does not vary as much as the thermohaline fluxes. The thick, compact Arctic sea ice tends to reduce the surface stress, while the looser, faster-moving Antarctic sea ice slightly increases it compared to the wind stress in open water. The resulting differences in turbulent mixing are likely less important than the heterogeneities in buoyancy fluxes.

5.1.2 Representation in models

The second question raised in this work was: **"How can these subgrid-scale, heterogeneous interactions be represented in large-scale sea ice-ocean models?"**. We have first tested the simple, well-established brine rejection parameterizations (BRPs). Then, we have implemented the more complex multi-column ocean (MCO) scheme to explicitly simulate heterogeneous sea ice-ocean interactions and vertical mixing processes. We summarize here our findings about these two methods.

BRPs have been developed in order to represent the effects of salt plumes caused by localized brine rejection in winter leads. To achieve this goal, the salt rejected during sea ice formation is incorporated within the mixed layer, instead of being placed at the ocean surface. When including the Nguyen et al. (2009) BRP formulation in NEMO-LIM, we noted strong decreases in mixed layer depths (MLDs) in the sea ice zone. By comparing carefully the model results with recent under-ice hydrographic products, we showed that, in general, these reductions were too strong and that the model agreement with observations was degraded. This is explained by the following three issues.

First, only a fraction of the total rejected salt occurs in leads. According to the model, this fraction is 3 % in February in the Arctic and 12 % in August in the Antarctic. Given that there is too little open waters in winter in LIM, these values might be underestimated. It is clear, however, that a significant part of the ice is formed by bottom accretion below the existing ice cover. The associated brine rejection occurs over large areas and should not be treated with the BRP. Second, the existence of salt plumes is conditioned upon small ice-ocean relative velocities. Otherwise the rejected brine is spread out at the surface and shear turbulence is dominant over convective mixing, which prevents the formation of plumes. Third, it is doubtful that salt plumes could reach the mixed layer base when the latter is several hundreds meters deep, as is the case over the Antarctic continental shelves. The poor model results in that region when the BRP is included tend to confirm that it should not be applied in that situation.

In summary, it turns out that applying the BRP in all conditions to all the salt rejected by sea ice is a serious oversimplification, which leads to a large overestimation of its effects. By using it in that way, the sole effect of brine rejections is to restratify the mixed layer, which is unrealistic. We interpret the improvements obtained in earlier studies as error compensations. Even in the case where the parameterization should be applied (i.e. for the salt rejected by a slowly-moving lead in a shallow mixed layer), it must be pointed out that the explicit upper ocean vertical mixing in the model is suppressed by the BRP, instead of being made localized. The parameterization only attempts to represent the impacts of the plumes on the salinity profiles, thereby missing the potential effects on vertical transfers of heat or biogeochemical tracers.

More explicit methods are needed to circumvent some of the limitations of the BRP. In this thesis, we developed and tested the so-called MCO scheme, in which ocean vertical mixing is computed separately in the fractions of ocean grid cells corresponding to open water and to the ice thickness categories of LIM. This approach was inspired by the one-dimensional exploratory study of Holland (2003) and can be seen as an oceanic extension of the subgrid-scale ice thickness distribution (ITD) present in many advanced sea ice models nowadays. It allows to avoid loosing the information about the heterogeneity of ocean surface fluxes provided by the ITD, to represent more accurately the heterogeneity of oceanic conditions under the different types of ice and in open waters, and thereby to simulate the processes listed in the previous section. In particular, and in contrary to BRPs, it does not suppress intense convective mixing induced by brine rejections in leads, but represents it explicitly and permits an evaluation of its effects on the upper ocean state.

Two versions of the MCO scheme have been tested. The main characteristics of MCO#1 is to homogenize the columns properties at the end of each time step. The vertical turbulent mixing cannot differ much between them, hence only the convection algorithm is called separately. The simulation results show that, when using the actual surface buoyancy flux distribution provided by the sea ice model, some subgrid-scale effects are noted but the ocean mean state is essentially unchanged. The reason is that, over one time step of one hour, even the most destabilizing surface fluxes are not able to generate convection penetrating below the mixed layer. In their study using a similar subgrid-scale mixing scheme, Jin et al. (2015) artificially amplified its effect by applying the salt rejections in a column of arbitrarily small extent. By contrast, our conclusion is that impacts of such a scheme, if any, should result from the persistence of the columns properties over periods longer than the model time step.

This leads to the second version of MCO, which is actually the central contribution of this thesis. In MCO#2, the temperature and salinity profiles of the

oceanic columns are laterally mixed with a homogenization time scale that is the scheme key parameter. This allows distinct profiles to be maintained over more than one time step, that is time spans potentially as long as several days. The need to handle separate vertical profiles at each grid point makes this version of MCO much more complex than the previous one. The implementation of such a scheme in three-dimensional simulations constitutes a technical achievement and a proof of concept. Furthermore, the possibility to decouple the homogenization time scale from the model time step is a definite advantage of MCO#2 over MCO#1.

From a physical point of view, MCO#2 requires that the model turbulent mixing scheme is called individually in each column, in addition to the convection scheme, because different stratifications may exist in the columns. In addition to allowing an explicit representation of the distinct oceanic conditions under sea ice, an important feature of MCO#2 is the ability to compute the surface fluxes using specific sea surface temperature and salinity. For instance, the atmosphere-ocean heat exchanges are calculated with the temperature of open waters. In summer, it may differ significantly from the grid cell average temperature that is normally used for the flux computations in current models. Although it has not been implemented here, the same comment is true for the lateral melt of ice floes. The ice-ocean exchanges are also derived from sea surface properties specific to each sea ice category. In this study, we have used the MCO#2 scheme in its full complexity, i.e. using all the available surface fluxes and the maximum number of columns, corresponding to the ITD in LIM. We only investigated the sensitivity of the results to changes in the homogenization time scale. Additional experiments could be conducted using this new tool in order to isolate and to study selected processes, as discussed in Section 5.2.

5.1.3 Large-scale influence

The last question asked in the introduction was (speaking of subgrid-scale ice-ocean interactions): **"Can we quantify their influence on the sea ice and underlying ocean?"**. We sum up our conclusions on this matter below. We first focus on the BRP. Then, we comment on the effects of the MCO#2 scheme, and on their dependence on the homogenization time scale and on other model features.

Previous studies and our tests demonstrate that the inclusion of the BRP results in a significant reduction of the MLDs under sea ice. But a close examination of model simulations lead us to identify clear limitations of the parameterization, described in the previous section. They indicate that the real impact of salt plumes is much smaller than suggested by the standard BRP im-

plementations. Regarding the role of the ice-ocean velocity in the existence of plumes, we have proposed a refinement of the parameterization, in which the latter is only active for low relative velocities. This modification comes at the price of new sources of uncertainty, mainly regarding the velocity threshold to use to disable the BRP, but it is an innovative way to enhance the physical realism of the brine rejection scheme. Based on the value of 5 cm s^{-1} suggested by the existing literature, the upgraded parameterization is used in limited areas in and north of the Canadian Arctic Archipelago. The fact that model results are improved in this experiment tend to show that salt plumes might indeed not be found in other regions, and specifically not under Antarctic sea ice. Considering moreover that the plumes are only associated to the salt rejected in narrow leads, the influence of this specific process is certainly much more modest than previously estimated. While the BRP is not incompatible with MCO, a combination of the two approaches does not seem particularly useful.

As mentioned above, the impacts of the MCO#1 vertical mixing scheme are practically nonexistent. With MCO#2, clear effects on the ocean and sea ice start to appear when the time scale of homogenization between the columns is of the order or longer than 10 h. The main ones include a decrease in MLDs and an increase in sea ice extent and volume at the seasonal minimum, which is explained by reductions in the oceanic heat flux at the ice base. On average in the polar regions, temperature and salinity profiles are weakly impacted. Yet, in the Antarctic, changes of larger magnitude are visible in areas known for their key role in the formation of Antarctic Bottom Water, namely the Ross and Weddell Seas and the coast of East Antarctica. This suggests possible effects of our representation of subgrid-scale mixing on the global ocean circulation, that we could however not investigate due to the short length of our model runs. In summary, the subgrid-scale sea ice-ocean interactions have potentially important impacts on the model results, but determining precisely the magnitude of the induced changes is made difficult by their high sensitivity to the homogenization time scale.

Furthermore, we might have underestimated the warming and freshening of summer leads in our analyses. On the one hand, the column corresponding to open water most certainly lacked freshwater inputs at the surface in summertime in our experiments, due to the absence of ice lateral melt and meltwater runoff from the ice in LIM. An implementation of the former is ultimately dependent on a floe size distribution. The fraction of meltwater remaining on top of the ice is not easy to estimate and is related to the existence of melt ponds, which constitute another active research area (e.g., Lecomte et al., 2015). On the other hand, in our three-dimensional simulations, we did

not attempt to embed the summer leads within the ice cover, as recommended by Holland (2003) to dampen their lateral mixing with the under-ice waters.

5.2 Limitations and perspectives

5.2.1 Parameterization of the MCO homogenization time scale

Developing a physically-based parameterization of the lateral mixing rate between the columns is the obvious follow-up that is needed in the context of MCO. It is nevertheless a complex question, given that this homogenization time scale is likely dependent on a great variety of factors. The constant value used in this work for this parameter is certainly a strong approximation. As a first example, a more intense mixing is expected when the contact areas between the columns is larger. This is related to the distribution of open water and of ice floes of different thicknesses at the sea surface. Unfortunately, the representation of the floe size distribution in models is today in its infancy. In this vein, lasting coastal polynyas, in which open waters and ice-covered areas are clearly separated, may for instance be associated to longer homogenization time scales, compared to leads within the sea ice pack. Secondly, the development of distinct ocean columns is more likely to occur for small ice-ocean relative velocities. In that case, the heterogeneous surface fluxes are indeed applied over the same portions of the water column for a certain period of time, and distinct oceanic mixing regimes may emerge. For large relative velocities, the vertical shear in the ocean and the related turbulent mixing would on the other hand result in a rapid horizontal homogenization of the upper ocean layer.

5.2.2 Ice thickness distributions

The implementation of MCO heavily relied on the ITD already present in LIM. A quantitative assessment of the effects of subgrid-scale ice-ocean interactions is conditioned upon a correct simulation of the areas of the columns, that is the open water fraction and the concentrations of the ice thickness categories. One outcome of the present study is that these variables are inaccurately represented in the current model version. Although to our knowledge no systematic study on that matter exists in the literature, this is probably the case in other models as well. ITDs are today well established in advanced sea ice models, but a more detailed examination of their results might now be needed to ensure that they are used at the best of their capabilities. Firstly, problems may arise from inadequate choices of the number and boundaries of the thickness categories. This issue is likely even more pronounced in the Antarctic, be-

cause of its thinner ice compared to the Arctic, for which the above-mentioned parameters are usually calibrated. Testing the sensitivity of the simulation results to the selected ITD would be useful, even regardless of MCO. A second source of errors lies in the modeled large-scale sea ice deformation patterns. Finally, even given properly simulated dynamics, a correct representation of the ITD and of the open water fraction depends on the thickness redistribution algorithms and on the treatment of lead opening and closing in the model.

5.2.3 Computational costs

At this stage, running NEMO-LIM with the MCO scheme activated results in a very substantial increase in required CPU time. A factor of 2.2 exists in the integration time between the reference code and the MCO#2 simulations, which are the ones of greatest interest. This is because the vertical mixing and convection algorithms are among the most demanding parts of the ocean model. Optimization has not been a concern so far, thus we are confident that there is much room for reductions of those additional costs. The first manner would be simply not to output the variables existing in all six columns, in particular the heavy three-dimensional temperature and salinity fields. Another method would be to reduce the number of columns used in the scheme. This would affect the model results, but using three columns corresponding to open water, thin and thick ice could be enough to represent the main effects at a more reasonable cost. A parameterization of the homogenization time scale could also lead to the conclusion that MCO needs to be activated only in selected regions, where this time scale is long and where the MCO effects are hence the largest. Nevertheless, because of the parallelization of the code, it is not straightforward to reduce the total integration time in that way. Finally, additional model fields existing for the six columns increase the memory usage when MCO#2 is turned on. Only a smaller number of columns would help in this case, but the use of massively parallel computers to run the current models means that high memory requirements are no longer a major issue.

5.2.4 Improvements of model results

The developments presented in this thesis, especially regarding MCO, provide an extremely valuable tool to study the interactions between sea ice and the underlying ocean in a modeling context. In addition, they enhance unquestionably the physical realism of the model. At this stage, it is not clear however that including such a vertical mixing scheme would improve the simulation results in any model configuration. In our experiments, MCO actually causes an underestimation of MLDs and strengthens the positive summer sea ice ex-

tent bias. By contrast, the increase in Antarctic summer sea ice extent would be beneficial for other setups, in which the latter is often too low. A similar comment can be made about the BRP. By design, this parameterization can only reduce MLDs. Therefore, a better observation-model agreement following the inclusion of the BRP fully depends on the initial model mean state. In the way previous studies applied the BRP, our results indicate nonetheless that the improvements were obtained for wrong reasons.

Taking into account the subgrid-scale surface fluxes is not the only way to influence the mean state of the model. The simulated MLDs are affected by a number of vertical mixing processes that are either absent or poorly-represented in NEMO. These include, for instance, surface waves, near-inertial wave breaking and Langmuir turbulence (e.g., Belcher et al., 2012; Huang et al., 2012, 2014; Fer, 2014). These mixing sources, even when parameterized in the model, require further testing and potentially some adaptations in ice-covered oceans. Additional work in that field could reduce the need for the background vertical diffusivity, which is now used to account for unresolved and unparameterized mixing processes, and which has been shown to be an important model parameter in polar regions. Additionally, increasing the model resolution is likely to have an impact on the simulated sea ice and ocean. The 1° horizontal resolution used in this study is nowadays in the low range for global oceanic circulation models. However, even in regional configurations reaching resolutions of the order of kilometers, the processes studied here cannot be explicitly represented. This means that subgrid-scale schemes like MCO will remain relevant for a wide range of applications.

5.2.5 Forcing formulation

Another factor strongly influencing the model mean state is the atmospheric forcing formulation. In the previous three chapters, NEMO-LIM has been driven by prescribed atmospheric fields, using the NCEP/NCAR reanalysis and various climatologies. Although it has not been discussed so far, those products suffer from known, and sometimes large, biases in polar regions, which introduces significant forcing uncertainties in the analyses that we have conducted. These uncertainties are particularly large in the Southern Ocean (e.g., Bromwich et al., 2007; Vancoppenolle et al., 2011), but they are also substantial in the Arctic (e.g., Jakobson et al., 2012; Chaudhuri et al., 2014; Lindsay et al., 2014). Using NEMO in a coupled framework with an interactive atmosphere would not necessarily solve the issues concerning the accuracy of the atmospheric fields provided to the ocean and sea ice models. It would, however, allow the simulation of feedbacks that were not permitted in our forced configuration. The large changes noted for the open water temperature in

summer indeed suggest that MCO might have a strong impact on air-water fluxes. More generally, the heterogeneity of atmosphere-ice interactions is a question related to the ice-ocean problem treated in this thesis, which deserves interest as well.

5.2.6 Further perspectives

As configured in this study, the sea ice module is called every six ocean model time steps, in order to save computational time. Short test experiments have shown that this coupling frequency actually has an impact on the model results. The first-order, qualitative response to the introduction of the MCO scheme is unchanged, but the feedbacks between the two components of the ice-ocean system could be affected at short time scales. Investigating the influence of the choice of this technical parameter, also in reference simulations without MCO, would be valuable in understanding the model behavior.

We have focused in this work on the oceanic heterogeneities induced by the subgrid-scale variability in sea ice. In the ocean itself, mesoscale and submesoscale turbulent activity is another source of horizontal heterogeneity in the mixed layer (e.g., Ilıcak et al., 2014; Couvelard et al., 2015). The situation at the sea ice edge would be especially interesting to study, in this respect. Very high resolutions simulations could be used to investigate the question, while stochastic parameterizations could offer a promising way to represent the effects of this subgrid-scale variability on vertical mixing processes.

The MCO tool developed in this thesis is one among several current refinements of the sea ice model LIM. Implementations of an upgraded snow scheme including a representation of melt ponds (Lecomte et al., 2013, 2015), of the new elasto-brittle rheology (Girard et al., 2011) and of a biogeochemistry component within the ice (e.g., Moreau et al., 2015) are other research directions. As is also the case for these developments, a careful choice has to be made regarding the processes that need to be included in the reference version of the code. Priority has to be given to the ones having the largest impact on both the results and the physics of the model, in order not to increase disproportionately the complexity of the latter.

APPENDIX A

ACRONYMS

AB	Arctic Basin
ACC	Antarctic Circumpolar Current
AOO	Antarctic Open Ocean
AS	Antarctic Shelves
ASPeCt	Antarctic Sea ice Processes and Climate
BRP	Brine Rejection Parameterization
CAA	Canadian Arctic Archipelago
CTD	Conductivity-Temperature-Depth
CVD	Convection Depth
ITD	Ice Thickness Distribution
ITP	Ice-Tethered Profiler
LIM	Louvain-la-Neuve sea Ice Model
MCO	Multi-Column Ocean
MEOP	Marine Mammals Exploring the Oceans Pole to Pole
MIMOC	Monthly Isopycnal and Mixed-layer Ocean Climatology
MLD	Mixed Layer Depth
NCAR	National Center for Atmospheric Research
NCEP	National Centers for Environmental Prediction
NEMO	Nucleus for European Modelling of the Ocean

NH	Northern Hemisphere
NPC	Non-Penetrative Convection
PIOMAS	Pan-Arctic Ice-Ocean Modeling and Assimilation System
PSU	Practical Salinity Unit
SBC	Surface Boundary Condition
SH	Southern Hemisphere
SHEBA	Surface Heat Budget of the Arctic Ocean
SSS	Sea Surface Salinity
SST	Sea Surface Temperature
TCD	Turbocline Depth
TKE	Turbulent Kinetic Energy
T/S	Temperature and Salinity

APPENDIX B

PUBLICATIONS AND COMMUNICATIONS RELATED TO THE THESIS

Publications

- **Barthélemy, A.**, Fichefet, T., Goosse, H., Madec, G., 2015. A multi-column vertical mixing scheme to parameterize the heterogeneity of oceanic conditions under sea ice. In preparation for Ocean Modelling. (Chapter 4)

- **Barthélemy, A.**, Fichefet, T., Goosse, H., 2015. Spatial heterogeneity of ocean surface boundary conditions under sea ice. Submitted to Ocean Modelling. (Chapter 3)

- Rousset, C., Vancoppenolle, M., Madec, G., Fichefet, T., Flavoni, S., **Barthélemy, A.**, Benshila, R., Chanut, J., Levy, C., Masson, S., Vivier, F., 2015. The Louvain-La-Neuve sea ice model LIM3.6: global and regional capabilities. Geoscientific Model Development 8, 2991 - 3005, doi: 10.5194/gmd-8-2991-2015.

- **Barthélemy, A.**, Fichefet, T., Goosse, H., Madec, G., 2015. Modeling the interplay between sea ice formation and the oceanic mixed layer: Limitations of simple brine rejection parameterizations. Ocean Modelling 86, 141 - 152, doi: 10.1016/j.ocemod.2014.12.009. (Chapter 2)

Communications

- April 2016: EGU, General Assembly 2016 (Vienna, Austria); abstract submitted for a poster presentation: A multi-column vertical mixing scheme to parameterize the heterogeneity of oceanic conditions under sea ice.
- June-July 2015: IUGG, General Assembly 2015 (Prague, Czech Republic); oral presentation: Multi-column ocean: taking advantage of the subgrid-scale distribution of sea ice to refine the ice-ocean interactions; poster presentation: Modeling the interplay between sea ice formation and the oceanic mixed layer: Limitations of simple brine rejection parameterizations.
- April 2015: EGU, General Assembly 2015 (Vienna, Austria); poster presentation: Modeling the interplay between sea ice formation and the oceanic mixed layer: Limitations of simple brine rejection parameterizations.
- December 2012: UNITER, 2nd Scientific Meeting (Brussels, Belgium); poster presentation: Refining the representation of sea ice-ocean interactions in the NEMO-LIM3 model (updated).
- May-June 2012: Les Houches Physics School, International Summer School on "Advanced Data Assimilation for Geosciences" (Les Houches, France); poster presentation: Refining the representation of sea ice-ocean interactions in the NEMO-LIM3 model.

REFERENCES

Adcroft, A., Hill, C., Marshall, J., 1997. Representation of Topography by Shaved Cells in a Height Coordinate Ocean Model. Mon. Wea. Rev. 125, 2293–2315. doi:10.1175/1520-0493(1997)125<2293:ROTBSC>2.0.CO;2.

Arndt, S., Nicolaus, M., 2014. Seasonal cycle and long-term trend of solar energy fluxes through Arctic sea ice. The Cryosphere 8, 2219–2233. doi:10.5194/tc-8-2219-2014.

Arthun, M., Nicholls, K.W., Boehme, L., 2013. Wintertime Water Mass Modification near an Antarctic Ice Front. J. Phys. Oceanogr. 43, 359–365. doi:10.1175/JPO-D-12-0186.1.

Asplin, M.G., Scharien, R., Else, B., Howell, S., Barber, D.G., Papakyriakou, T., Prinsenberg, S., 2014. Implications of fractured Arctic perennial ice cover on thermodynamic and dynamic sea ice processes. J. Geophys. Res. Oceans 119, 2327–2343. doi:10.1002/2013JC009557.

Barnhart, K.R., Overeem, I., Anderson, R.S., 2014. The effect of changing sea ice on the physical vulnerability of Arctic coasts. The Cryosphere 8, 1777–1799. doi:10.5194/tc-8-1777-2014.

Barthélemy, A., Goosse, H., Mathiot, P., Fichefet, T., 2012. Inclusion of a katabatic wind correction in a coarse-resolution global coupled climate model. Ocean Modell. 48, 45–54. doi:10.1016/j.ocemod.2012.03.002.

Behrendt, A., Dierking, W., Witte, H., 2015. Thermodynamic sea ice growth in the central Weddell Sea, observed in upward-looking sonar data. J. Geophys. Res. Oceans 120, 2270–2286. doi:10.1002/2014JC010408.

Belcher, S.E., Grant, A.L.M., Hanley, K.E., Fox-Kemper, B., Van Roekel, L., Sullivan, P.P., Large, W.G., Brown, A., Hines, A., Calvert, D., Rutgersson, A., Pettersson, H., Bidlot, J.R., Janssen, P.A.E.M., Polton, J.A., 2012. A global perspective on Langmuir turbulence in the ocean surface boundary layer. Geophys. Res. Lett. 39, L18605. doi:10.1029/2012GL052932.

Berliand, M.E., Strokina, T.G., 1980. Global distribution of the total amount of clouds (in Russian). Technical Report. Hydrometeorological Publishing House. Leningrad, Russia.

Bintanja, R., van Oldenborgh, G.J., Drijfhout, S.S., Wouters, B., Katsman, C.A., 2013. Important role for ocean warming and increased ice-shelf melt in Antarctic sea-ice expansion. Nat. Geosci. 6, 376–379. doi:10.1038/ngeo1767.

Bitz, C.M., Holland, M.M., Weaver, A.J., Eby, M., 2001. Simulating the ice-thickness distribution in a coupled climate model. J. Geophys. Res. 106, 2441–2463. doi:10.1029/1999JC000113.

Bitz, C.M., Lipscomb, W.H., 1999. An energy-conserving thermodynamic model of sea ice. J. Geophys. Res. 104, 15669–15677. doi:10.1029/1999JC900100.

Blanke, B., Delecluse, P., 1993. Variability of the Tropical Atlantic Ocean Simulated by a General Circulation Model with Two Different Mixed-Layer Physics. J. Phys. Oceanogr. 23, 1363–1388. doi:10.1175/1520-0485(1993)023<1363:VOTTAO>2.0.CO;2.

Blüthgen, J., Gerdes, R., Werner, M., 2012. Atmospheric response to the extreme Arctic sea ice conditions in 2007. Geophys. Res. Lett. 39, L02707. doi:10.1029/2011GL050486.

Bouillon, S., Fichefet, T., Legat, V., Madec, G., 2013. The elastic-viscous-plastic method revisited. Ocean Modell. 71, 2–12. doi:10.1016/j.ocemod.2013.05.013.

Bouillon, S., Morales Maqueda, M.A., Legat, V., Fichefet, T., 2009. An elastic-viscous-plastic sea ice model formulated on Arakawa B and C grids. Ocean Modell. 27, 174–184. doi:10.1016/j.ocemod.2009.01.004.

Bouillon, S., Rampal, P., 2015. Presentation of the dynamical core of neXtSIM, a new sea ice model. Ocean Modell. 91, 23–37. doi:10.1016/j.ocemod.2015.04.005.

Bourassa, M.A., Gille, S.T., Bitz, C., Carlson, D., Cerovecki, I., Clayson, C.A., Cronin, M.F., Drennan, W.M., Fairall, C.W., Hoffman, R.N., Magnusdottir, G., Pinker, R.T., Renfrew, I.A., Serreze, M., Speer, K., Talley, L.D., Wick, G.A., 2013. High-Latitude Ocean and Sea Ice Surface Fluxes: Challenges for Climate Research. Bull. Amer. Meteor. Soc. 94, 403–423. doi:10.1175/BAMS-D-11-00244.1.

Bourgain, P., Gascard, J.C., 2012. The Atlantic and summer Pacific waters variability in the Arctic Ocean from 1997 to 2008. Geophys. Res. Lett. 39, L05603. doi:10.1029/2012GL051045.

Bouttes, N., Paillard, D., Roche, D.M., 2010. Impact of brine-induced stratification on the glacial carbon cycle. Clim. Past 6, 575–589. doi:10.5194/cp-6-575-2010.

de Boyer Montégut, C., Madec, G., Fischer, A.S., Lazar, A., Iudicone, D., 2004. Mixed layer depth over the global ocean: An examination of profile data and a profile-based climatology. J. Geophys. Res. 109, C12003. doi:10.1029/2004JC002378.

Bromwich, D.H., Fogt, R.L., Hodges, K.I., Walsh, J.E., 2007. A tropospheric assessment of the ERA-40, NCEP, and JRA-25 global reanalyses in the polar regions. J. Geophys. Res. 112, D10111. doi:10.1029/2006JD007859.

Caldeira, K., Cvijanovic, I., 2014. Estimating the Contribution of Sea Ice Response to Climate Sensitivity in a Climate Model. J. Climate 27, 8597–8607. doi:10.1175/JCLI-D-14-00042.1.

Calvert, D., Siddorn, J., 2013. Revised vertical mixing parameters for the UK community standard configuration of the global NEMO ocean model. Technical Note 95. Met Office Hadley Centre. United Kingdom.

Campin, J.M., Hill, C., Jones, H., Marshall, J., 2011. Super-parameterization in ocean modeling: Application to deep convection. Ocean Modell. 36, 90–101. doi:10.1016/j.ocemod.2010.10.003.

Carmack, E., Melling, H., 2011. Warmth from the deep. Nat. Geosci. 4, 7–8. doi:10.1038/ngeo1044.

Castro-Morales, K., Kauker, F., Losch, M., Hendricks, S., Riemann-Campe, K., Gerdes, R., 2014. Sensitivity of simulated Arctic sea ice to realistic ice thickness distributions and snow parameterizations. J. Geophys. Res. Oceans 119, 559–571. doi:10.1002/2013JC009342.

Cavalieri, D.J., Parkinson, C.L., Gloersen, P., Zwally, H., 1996. Sea Ice Concentrations from Nimbus-7 SMMR and DMSP SSM/I-SSMIS Passive Microwave Data. [1979-2010]. NASA National Snow and Ice Data Center Distributed Active Archive Center. Boulder, Colorado, USA. doi:10.5067/8GQ8LZQVL0VL.

Chaudhuri, A.H., Ponte, R.M., Nguyen, A.T., 2014. A Comparison of Atmospheric Reanalysis Products for the Arctic Ocean and Implications for

Uncertainties in Air-Sea Fluxes. J. Climate 27, 5411–5421. doi:10.1175/JCLI-D-13-00424.1.

Chevallier, M., Salas y Mélia, D., Voldoire, A., Déqué, M., Garric, G., 2013. Seasonal Forecasts of the Pan-Arctic Sea Ice Extent Using a GCM-Based Seasonal Prediction System. J. Climate 26, 6092–6104. doi:10.1175/JCLI-D-12-00612.1.

Close, S.E., Goosse, H., 2013. Entrainment-driven modulation of Southern Ocean mixed layer properties and sea ice variability in CMIP5 models. J. Geophys. Res. Oceans 118, 2811–2827. doi:10.1002/jgrc.20226.

Comiso, J.C., 2000. Bootstrap Sea Ice Concentrations from Nimbus-7 SMMR and DMSP SSM/I-SSMIS. Version 2. [1979-2012]. NASA National Snow and Ice Data Center Distributed Active Archive Center. Boulder, Colorado, USA. doi:10.5067/J6JQLS9EJ5HU.

Comiso, J.C., 2011. Large Decadal Decline of the Arctic Multiyear Ice Cover. J. Climate 25, 1176–1193. doi:10.1175/JCLI-D-11-00113.1.

Conkright, M.E., Locarnini, R.A., Garcia, H.E., O'Brien, T.D., Boyer, T.P., Stephens, C., Antonov, J.I., 2002. World Ocean Atlas 2001. Digital media. National Oceanographic Data Center. Silver Spring, Maryland, USA.

Couldrey, M.P., Jullion, L., Naveira Garabato, A.C., Rye, C., Herráiz-Borreguero, L., Brown, P.J., Meredith, M.P., Speer, K.L., 2013. Remotely induced warming of Antarctic Bottom Water in the eastern Weddell gyre. Geophys. Res. Lett. 40, 2755–2760. doi:10.1002/grl.50526.

Couvelard, X., Dumas, F., Garnier, V., Ponte, A., Talandier, C., Treguier, A., 2015. Mixed layer formation and restratification in presence of mesoscale and submesoscale turbulence. Ocean Modell. 96, Part 2, 243–253. doi:10.1016/j.ocemod.2015.10.004.

Curry, J.A., Schramm, J.L., Ebert, E.E., 1995. Sea Ice-Albedo Climate Feedback Mechanism. J. Climate 8, 240–247. doi:10.1175/1520-0442(1995)008<0240:SIACFM>2.0.CO;2.

Dai, A., Trenberth, K.E., 2002. Estimates of Freshwater Discharge from Continents: Latitudinal and Seasonal Variations. J. Hydrometeor. 3, 660–687. doi:10.1175/1525-7541(2002)003<0660:EOFDFC>2.0.CO;2.

Day, J.J., Hawkins, E., Tietsche, S., 2014. Will Arctic sea ice thickness initialization improve seasonal forecast skill? Geophys. Res. Lett. 41, 7566–7575. doi:10.1002/2014GL061694.

Delille, B., Vancoppenolle, M., Geilfus, N.X., Tilbrook, B., Lannuzel, D., Schoemann, V., Becquevort, S., Carnat, G., Delille, D., Lancelot, C., Chou, L., Dieckmann, G.S., Tison, J.L., 2014. Southern Ocean CO2 sink: The contribution of the sea ice. J. Geophys. Res. Oceans 119, 6340–6355. doi:10.1002/2014JC009941.

Dong, S., Sprintall, J., Gille, S.T., Talley, L., 2008. Southern Ocean mixed-layer depth from Argo float profiles. J. Geophys. Res. 113, C06013. doi:10.1029/2006JC004051.

Downes, S.M., Farneti, R., Uotila, P., Griffies, S.M., Marsland, S.J., Bailey, D., Behrens, E., Bentsen, M., Bi, D., Biastoch, A., Böning, C., Bozec, A., Canuto, V.M., Chassignet, E., Danabasoglu, G., Danilov, S., Diansky, N., Drange, H., Fogli, P.G., Gusev, A., Howard, A., Ilicak, M., Jung, T., Kelley, M., Large, W.G., Leboissetier, A., Long, M., Lu, J., Masina, S., Mishra, A., Navarra, A., George Nurser, A., Patara, L., Samuels, B.L., Sidorenko, D., Spence, P., Tsujino, H., Wang, Q., Yeager, S.G., 2015. An assessment of Southern Ocean water masses and sea ice during 1988-2007 in a suite of interannual CORE-II simulations. Ocean Modell. 94, 67–94. doi:10.1016/j.ocemod.2015.07.022.

Duffy, P.B., Caldeira, K., 1997. Sensitivity of simulated salinity in a three-dimensional ocean model to upper ocean transport of salt from sea-ice formation. Geophys. Res. Lett. 24, 1323–1326. doi:10.1029/97GL01294.

Duffy, P.B., Eby, M., Weaver, A.J., 1999. Effects of sinking of salt rejected during formation of sea ice on results of an ocean-atmosphere-sea ice climate model. Geophys. Res. Lett. 26, 1739–1742. doi:10.1029/1999GL900286.

Eisenman, I., Meier, W.N., Norris, J.R., 2014. A spurious jump in the satellite record: has Antarctic sea ice expansion been overestimated? The Cryosphere 8, 1289–1296. doi:10.5194/tc-8-1289-2014.

Fahrbach, E., Hoppema, M., Rohardt, G., Schröder, M., Wisotzki, A., 2004. Decadal-scale variations of water mass properties in the deep Weddell Sea. Ocean Dyn. 54, 77–91. doi:10.1007/s10236-003-0082-3.

Fan, T., Deser, C., Schneider, D.P., 2014. Recent Antarctic sea ice trends in the context of Southern Ocean surface climate variations since 1950. Geophys. Res. Lett. 41, 2014GL059239. doi:10.1002/2014GL059239.

Fer, I., 2014. Near-Inertial Mixing in the Central Arctic Ocean. J. Phys. Oceanogr. 44, 2031–2049. doi:10.1175/JPO-D-13-0133.1.

Flato, G.M., Hibler, W.D., 1995. Ridging and strength in modeling the thickness distribution of Arctic sea ice. J. Geophys. Res. 100, 18611–18626. doi:10.1029/95JC02091.

Fox-Kemper, B., Danabasoglu, G., Ferrari, R., Griffies, S., Hallberg, R., Holland, M., Maltrud, M., Peacock, S., Samuels, B., 2011. Parameterization of mixed layer eddies. III: Implementation and impact in global ocean climate simulations. Ocean Modell. 39, 61–78. doi:10.1016/j.ocemod.2010.09.002.

Francis, J.A., Vavrus, S.J., 2012. Evidence linking Arctic amplification to extreme weather in mid-latitudes. Geophys. Res. Lett. 39, L06801. doi:10.1029/2012GL051000.

Gent, P.R., Mcwilliams, J.C., 1990. Isopycnal Mixing in Ocean Circulation Models. J. Phys. Oceanogr. 20, 150–155. doi:10.1175/1520-0485(1990)020<0150:IMIOCM>2.0.CO;2.

Gimbert, F., Jourdain, N.C., Marsan, D., Weiss, J., Barnier, B., 2012. Recent mechanical weakening of the Arctic sea ice cover as revealed from larger inertial oscillations. J. Geophys. Res. 117, C00J12. doi:10.1029/2011JC007633.

Girard, L., Bouillon, S., Weiss, J., Amitrano, D., Fichefet, T., Legat, V., 2011. A new modeling framework for sea-ice mechanics based on elasto-brittle rheology. Ann. Glaciol. 52, 123–132. doi:10.3189/172756411795931499.

Goosse, H., 1997. Modelling the large-scale behaviour of the coupled ocean-sea-ice system. Ph.D. thesis. Université catholique de Louvain.

Goosse, H., 2015. Climate System Dynamics and Modelling. Cambridge University Press.

Goosse, H., Fichefet, T., 1999. Importance of ice-ocean interactions for the global ocean circulation: A model study. J. Geophys. Res. 104, 23337–23355. doi:10.1029/1999JC900215.

Goosse, H., Zunz, V., 2014. Decadal trends in the Antarctic sea ice extent ultimately controlled by ice-ocean feedback. The Cryosphere 8, 453–470. doi:10.5194/tc-8-453-2014.

Gordon, A.L., Huber, B.A., 1984. Thermohaline stratification below the Southern Ocean sea ice. J. Geophys. Res. 89, 641–648. doi:10.1029/JC089iC01p00641.

Gordon, A.L., Huber, B.A., 1990. Southern ocean winter mixed layer. J. Geophys. Res. 95, 11655–11672. doi:10.1029/JC095iC07p11655.

Haid, V., Timmermann, R., 2013. Simulated heat flux and sea ice production at coastal polynyas in the southwestern Weddell Sea. J. Geophys. Res. Oceans 118, 2640–2652. doi:10.1002/jgrc.20133.

Hansen, E., Gerland, S., Granskog, M.A., Pavlova, O., Renner, A.H.H., Haapala, J., Løyning, T.B., Tschudi, M., 2013. Thinning of Arctic sea ice observed in Fram Strait: 1990-2011. J. Geophys. Res. Oceans 118, 5202–5221. doi:10.1002/jgrc.20393.

Hawkins, E., Sutton, R., 2009. The Potential to Narrow Uncertainty in Regional Climate Predictions. Bull. Amer. Meteor. Soc. 90, 1095–1107. doi:10.1175/2009BAMS2607.1.

Heuzé, C., Heywood, K.J., Stevens, D.P., Ridley, J.K., 2013. Southern Ocean bottom water characteristics in CMIP5 models. Geophys. Res. Lett. 40, 1409–1414. doi:10.1002/grl.50287.

Heuzé, C., Ridley, J.K., Calvert, D., Stevens, D.P., Heywood, K.J., 2015. Increasing vertical mixing to reduce Southern Ocean deep convection in NEMO3.4. Geosci. Model Dev. 8, 3119–3130. doi:10.5194/gmd-8-3119-2015.

Hibler, W.D., 1980. Modeling a Variable Thickness Sea Ice Cover. Mon. Wea. Rev. 108, 1943–1973. doi:10.1175/1520-0493(1980)108<1943:MAVTSI>2.0.CO;2.

Holland, M.M., 2003. An improved single-column model representation of ocean mixing associated with summertime leads: Results from a SHEBA case study. J. Geophys. Res. 108, 3107. doi:10.1029/2002JC001557.

Holland, M.M., Curry, J.A., Schramm, J.L., 1997. Modeling the thermodynamics of a sea ice thickness distribution 2. Sea ice/ocean interactions. J. Geophys. Res. 102, 23093–23107. doi:10.1029/97JC01296.

Holland, P.R., Bruneau, N., Enright, C., Losch, M., Kurtz, N.T., Kwok, R., 2014. Modeled Trends in Antarctic Sea Ice Thickness. J. Climate 27, 3784–3801. doi:10.1175/JCLI-D-13-00301.1.

Holland, P.R., Kwok, R., 2012. Wind-driven trends in Antarctic sea-ice drift. Nat. Geosci. 5, 872–875. doi:10.1038/ngeo1627.

Holte, J., Talley, L., 2009. A New Algorithm for Finding Mixed Layer Depths with Applications to Argo Data and Subantarctic Mode Water Formation. J. Atmos. Oceanic Technol. 26, 1920–1939. doi:10.1175/2009JTECHO543.1.

Horvat, C., Tziperman, E., 2015. A prognostic model of the sea-ice floe size and thickness distribution. The Cryosphere 9, 2119–2134. doi:10.5194/tc-9-2119-2015.

Huang, C.J., Qiao, F., Dai, D., 2014. Evaluating CMIP5 simulations of mixed layer depth during summer. J. Geophys. Res. Oceans 119, 2568–2582. doi:10.1002/2013JC009535.

Huang, C.J., Qiao, F., Shu, Q., Song, Z., 2012. Evaluating austral summer mixed-layer response to surface wave-induced mixing in the Southern Ocean. J. Geophys. Res. 117, C00J18. doi:10.1029/2012JC007892.

Hudson, S.R., Granskog, M.A., Sundfjord, A., Randelhoff, A., Renner, A.H.H., Divine, D.V., 2013. Energy budget of first-year Arctic sea ice in advanced stages of melt. Geophys. Res. Lett. 40, 2679–2683. doi:10.1002/grl.50517.

Hunke, E.C., 2010. Thickness sensitivities in the CICE sea ice model. Ocean Modell. 34, 137–149. doi:10.1016/j.ocemod.2010.05.004.

Hunke, E.C., 2014. Sea ice volume and age: Sensitivity to physical parameterizations and thickness resolution in the CICE sea ice model. Ocean Modell. 82, 45–59. doi:10.1016/j.ocemod.2014.08.001.

Hunke, E.C., Dukowicz, J.K., 1997. An Elastic-Viscous-Plastic Model for Sea Ice Dynamics. J. Phys. Oceanogr. 27, 1849–1867. doi:10.1175/1520-0485(1997)027<1849:AEVPMF>2.0.CO;2.

Hunke, E.C., Hebert, D.A., Lecomte, O., 2013. Level-ice melt ponds in the Los Alamos sea ice model, CICE. Ocean Modell. 71, 26–42. doi:10.1016/j.ocemod.2012.11.008.

Hunke, E.C., Lipscomb, W.H., Turner, A.K., Jeffery, N., Elliott, S., 2015. CICE: the Los Alamos Sea Ice Model Documentation and Software User's Manual Version 5.1. Technical Report LA-CC-06-012. Los Alamos National Laboratory. Los Alamos, New Mexico.

Ilıcak, M., Adcroft, A.J., Legg, S., 2014. A framework for parameterization of heterogeneous ocean convection. Ocean Modell. 82, 1–14. doi:10.1016/j.ocemod.2014.07.002.

IPCC, 2013. Climate Change 2013: The Physical Science Basis. Contribution of Working Group I to the Fifth Assessment Report of the Intergovernmental Panel on Climate Change. Cambridge University Press, Cambridge, United Kingdom and New York, NY, USA. doi:10.1017/CBO9781107415324.

Itkin, P., Losch, M., Gerdes, R., 2015. Landfast ice affects the stability of the Arctic halocline: Evidence from a numerical model. J. Geophys. Res. Oceans 120, 2622–2635. doi:10.1002/2014JC010353.

Jackson, J.M., Williams, W.J., Carmack, E.C., 2012. Winter sea-ice melt in the Canada Basin, Arctic Ocean. Geophys. Res. Lett. 39, L03603. doi:10.1029/2011GL050219.

Jacobs, S.S., Comiso, J.C., 1989. Sea ice and oceanic processes on the Ross Sea continental shelf. J. Geophys. Res. 94, 18195–18211. doi:10.1029/JC094iC12p18195.

Jakobson, E., Vihma, T., Palo, T., Jakobson, L., Keernik, H., Jaagus, J., 2012. Validation of atmospheric reanalyses over the central Arctic Ocean. Geophys. Res. Lett. 39, L10802. doi:10.1029/2012GL051591.

Jin, M., Hutchings, J., Kawaguchi, Y., 2015. Sensitivity study of subgrid scale ocean mixing under sea ice using a two-column ocean grid in climate model CESM. Front. Earth Sci. 9, 594–604. doi:10.1007/s11707-014-0489-9.

Jin, M., Hutchings, J., Kawaguchi, Y., Kikuchi, T., 2012. Ocean mixing with lead-dependent subgrid scale brine rejection parameterization in a climate model. J. Ocean Univ. China 11, 473–480. doi:10.1007/s11802-012-2094-4.

Kalnay, E., Kanamitsu, M., Kistler, R., Collins, W., Deaven, D., Gandin, L., Iredell, M., Saha, S., White, G., Woollen, J., Zhu, Y., Leetmaa, A., Reynolds, R., Chelliah, M., Ebisuzaki, W., Higgins, W., Janowiak, J., Mo, K.C., Ropelewski, C., Wang, J., Jenne, R., Joseph, D., 1996. The NCEP/NCAR 40-Year Reanalysis Project. Bull. Amer. Meteor. Soc. 77, 437–471. doi:10.1175/1520-0477(1996)077<0437:TNYRP>2.0.CO;2.

Kantha, L.H., 1995. A numerical model of Arctic leads. J. Geophys. Res. 100, 4653–4672. doi:10.1029/94JC02348.

Katlein, C., Arndt, S., Nicolaus, M., Perovich, D.K., Jakuba, M.V., Suman, S., Elliott, S., Whitcomb, L.L., McFarland, C.J., Gerdes, R., Boetius, A., German, C.R., 2015. Influence of ice thickness and surface properties on light transmission through Arctic sea ice. J. Geophys. Res. Oceans 120, 5932–5944. doi:10.1002/2015JC010914.

Kim, S.J., Stössel, A., 2001. Impact of Subgrid-Scale Convection on Global Thermohaline Properties and Circulation. J. Phys. Oceanogr. 31, 656–674. doi:10.1175/1520-0485(2001)031<0656:IOSSCO>2.0.CO;2.

Kjellsson, J., Holland, P.R., Marshall, G.J., Mathiot, P., Aksenov, Y., Coward, A.C., Bacon, S., Megann, A.P., Ridley, J., 2015. Model sensitivity of the Weddell and Ross seas, Antarctica, to vertical mixing and freshwater forcing. Ocean Modell. 94, 141–152. doi:10.1016/j.ocemod.2015.08.003.

Komuro, Y., 2014. The Impact of Surface Mixing on the Arctic River Water Distribution and Stratification in a Global Ice-Ocean Model. J. Climate 27, 4359–4370. doi:10.1175/JCLI-D-13-00090.1.

Komuro, Y., Suzuki, T., 2013. Impact of subgrid-scale ice thickness distribution on heat flux on and through sea ice. Ocean Modell. 71, 13–25. doi:10.1016/j.ocemod.2012.08.004.

Krishfield, R., Toole, J., Proshutinsky, A., Timmermans, M.L., 2008. Automated Ice-Tethered Profilers for Seawater Observations under Pack Ice in All Seasons. J. Atmos. Oceanic Technol. 25, 2091–2105. doi:10.1175/2008JTECHO587.1.

Krishfield, R.A., Perovich, D.K., 2005. Spatial and temporal variability of oceanic heat flux to the Arctic ice pack. J. Geophys. Res. 110, C07021. doi:10.1029/2004JC002293.

Krishfield, R.A., Proshutinsky, A., Tateyama, K., Williams, W.J., Carmack, E.C., McLaughlin, F.A., Timmermans, M.L., 2014. Deterioration of perennial sea ice in the Beaufort Gyre from 2003 to 2012 and its impact on the oceanic freshwater cycle. J. Geophys. Res. Oceans 119, 1271–1305. doi:10.1002/2013JC008999.

Kurtz, N., Studinger, M.S., Harbeck, J., Onana, V., Farrell, S., 2012. IceBridge Sea Ice Freeboard, Snow Depth, and Thickness. [2009-2010]. NASA National Snow and Ice Data Center Distributed Active Archive Center. Boulder, Colorado, USA. doi:10.5067/7XJ9HRV50O57.

Kurtz, N., Studinger, M.S., Harbeck, J., Onana, V., Yi, D., 2015. IceBridge L4 Sea Ice Freeboard, Snow Depth, and Thickness. [2009-2013]. NASA National Snow and Ice Data Center Distributed Active Archive Center. Boulder, Colorado, USA. doi:10.5067/G519SHCKWQV6.

Kurtz, N.T., Farrell, S.L., Studinger, M., Galin, N., Harbeck, J.P., Lindsay, R., Onana, V.D., Panzer, B., Sonntag, J.G., 2013. Sea ice thickness, freeboard, and snow depth products from Operation IceBridge airborne data. The Cryosphere 7, 1035–1056. doi:10.5194/tc-7-1035-2013.

Kurtz, N.T., Markus, T., 2012. Satellite observations of Antarctic sea ice thickness and volume. J. Geophys. Res. 117, C08025. doi:10.1029/2012JC008141.

Kwok, R., Cunningham, G.F., Manizade, S.S., Krabill, W.B., 2012. Arctic sea ice freeboard from IceBridge acquisitions in 2009: Estimates and comparisons with ICESat. J. Geophys. Res. 117, C02018. doi:10.1029/2011JC007654.

Kwok, R., Spreen, G., Pang, S., 2013. Arctic sea ice circulation and drift speed: Decadal trends and ocean currents. J. Geophys. Res. Oceans 118, 2408–2425. doi:10.1002/jgrc.20191.

Lane-Serff, G.F., Stansfield, K.L., 2013. Observations of mixed layer deepening during an Antarctic gale. J. Geophys. Res. Oceans 118, 1396–1404. doi:10.1002/jgrc.20140.

Large, W.G., Yeager, S.G., 2004. Diurnal to decadal global forcing for ocean and sea-ice models: The data sets and flux climatologies. Technical Report. National Center for Atmospheric Research. Boulder, Colorado, USA.

Laxon, S.W., Giles, K.A., Ridout, A.L., Wingham, D.J., Willatt, R., Cullen, R., Kwok, R., Schweiger, A., Zhang, J., Haas, C., Hendricks, S., Krishfield, R., Kurtz, N., Farrell, S., Davidson, M., 2013. CryoSat-2 estimates of Arctic sea ice thickness and volume. Geophys. Res. Lett. 40, 732–737. doi:10.1002/grl.50193.

Lecomte, O., Fichefet, T., Flocco, D., Schroeder, D., Vancoppenolle, M., 2015. Interactions between wind-blown snow redistribution and melt ponds in a coupled ocean-sea ice model. Ocean Modell. 87, 67–80. doi:10.1016/j.ocemod.2014.12.003.

Lecomte, O., Fichefet, T., Vancoppenolle, M., Domine, F., Massonnet, F., Mathiot, P., Morin, S., Barriat, P., 2013. On the formulation of snow thermal conductivity in large-scale sea ice models. J. Adv. Model. Earth Syst. 5, 542–557. doi:10.1002/jame.20039.

Lei, R., Li, N., Heil, P., Cheng, B., Zhang, Z., Sun, B., 2014. Multiyear sea ice thermal regimes and oceanic heat flux derived from an ice mass balance buoy in the Arctic Ocean. J. Geophys. Res. Oceans 119, 537–547. doi:10.1002/2012JC008731.

Lemieux, J.F., Tremblay, L.B., Dupont, F., Plante, M., Smith, G.C., Dumont, D., 2015. A basal stress parameterization for modeling landfast ice. J. Geophys. Res. Oceans 120, 3157–3173. doi:10.1002/2014JC010678.

Linders, J., Björk, G., 2013. The melt-freeze cycle of the Arctic Ocean ice cover and its dependence on ocean stratification. J. Geophys. Res. Oceans 118, 5963–5976. doi:10.1002/jgrc.20409.

Lindsay, R., Schweiger, A., 2015. Arctic sea ice thickness loss determined using subsurface, aircraft, and satellite observations. The Cryosphere 9, 269–283. doi:10.5194/tc-9-269-2015.

Lindsay, R., Wensnahan, M., Schweiger, A., Zhang, J., 2014. Evaluation of Seven Different Atmospheric Reanalysis Products in the Arctic. J. Climate 27, 2588–2606. doi:10.1175/JCLI-D-13-00014.1.

Lique, C., Guthrie, J.D., Steele, M., Proshutinsky, A., Morison, J.H., Krishfield, R., 2014. Diffusive vertical heat flux in the Canada Basin of the Arctic Ocean inferred from moored instruments. J. Geophys. Res. Oceans 119, 496–508. doi:10.1002/2013JC009346.

Long, M.C., Lindsay, K., Holland, M.M., 2015. Modeling photosynthesis in sea ice-covered waters. J. Adv. Model. Earth Syst. 7, 1189–1206. doi:10.1002/2015MS000436.

Losch, M., Herlufsen, S., Timmermann, R., 2006. Effects of heterogeneous surface boundary conditions on parameterized oceanic deep convection. Ocean Modell. 13, 156–165. doi:10.1016/j.ocemod.2005.12.003.

Lu, P., Li, Z., Cheng, B., Leppäranta, M., 2011. A parameterization of the ice-ocean drag coefficient. J. Geophys. Res. 116, C07019. doi:10.1029/2010JC006878.

Lüpkes, C., Gryanik, V.M., Hartmann, J., Andreas, E.L., 2012. A parametrization, based on sea ice morphology, of the neutral atmospheric drag coefficients for weather prediction and climate models. J. Geophys. Res. 117, D13112. doi:10.1029/2012JD017630.

Lüpkes, C., Gryanik, V.M., Rösel, A., Birnbaum, G., Kaleschke, L., 2013. Effect of sea ice morphology during Arctic summer on atmospheric drag coefficients used in climate models. Geophys. Res. Lett. 40, 446–451. doi:10.1002/grl.50081.

Madec, G., 2008. NEMO ocean engine. Note du Pôle de modélisation 27. Institut Pierre-Simon Laplace. France. ISSN No 1288-1619.

Madec, G., Delecluse, P., Crepon, M., Chartier, M., 1991. A Three-Dimensional Numerical Study of Deep-Water Formation in the Northwestern Mediterranean Sea. J. Phys. Oceanogr. 21, 1349–1371. doi:10.1175/1520-0485(1991)021<1349:ATDNSO>2.0.CO;2.

Madec, G., Imbard, M., 1996. A global ocean mesh to overcome the North Pole singularity. Clim. Dynam. 12, 381–388. doi:10.1007/BF00211684.

Marcq, S., Weiss, J., 2012. Influence of sea ice lead-width distribution on turbulent heat transfer between the ocean and the atmosphere. The Cryosphere 6, 143–156. doi:10.5194/tc-6-143-2012.

Marshall, J., Plumb, R.A., 2007. Atmosphere, Ocean and Climate Dynamics, An Introductory Text. volume 93 of *International Geophysics Series*. Academic Press.

Martinson, D.G., 1990. Evolution of the southern ocean winter mixed layer and sea ice: Open ocean deepwater formation and ventilation. J. Geophys. Res. 95, 11641–11654. doi:10.1029/JC095iC07p11641.

Massonnet, F., Fichefet, T., Goosse, H., 2015. Prospects for improved seasonal Arctic sea ice predictions from multivariate data assimilation. Ocean Modell. 88, 16–25. doi:10.1016/j.ocemod.2014.12.013.

Massonnet, F., Fichefet, T., Goosse, H., Vancoppenolle, M., Mathiot, P., König Beatty, C., 2011. On the influence of model physics on simulations of Arctic and Antarctic sea ice. The Cryosphere 5, 687–699. doi:10.5194/tc-5-687-2011.

Massonnet, F., Goosse, H., Fichefet, T., Counillon, F., 2014. Calibration of sea ice dynamic parameters in an ocean-sea ice model using an ensemble Kalman filter. J. Geophys. Res. Oceans 119, 4168–4184. doi:10.1002/2013JC009705.

Massonnet, F., Mathiot, P., Fichefet, T., Goosse, H., König Beatty, C., Vancoppenolle, M., Lavergne, T., 2013. A model reconstruction of the Antarctic sea ice thickness and volume changes over 1980-2008 using data assimilation. Ocean Modell. 64, 67–75. doi:10.1016/j.ocemod.2013.01.003.

Matsumura, Y., Hasumi, H., 2008. Brine-Driven Eddies under Sea Ice Leads and Their Impact on the Arctic Ocean Mixed Layer. J. Phys. Oceanogr. 38, 146–163. doi:10.1175/2007JPO3620.1.

Maykut, G.A., 1978. Energy exchange over young sea ice in the central Arctic. J. Geophys. Res. 83, 3646–3658. doi:10.1029/JC083iC07p03646.

Maykut, G.A., 1982. Large-scale heat exchange and ice production in the central Arctic. J. Geophys. Res. 87, 7971–7984. doi:10.1029/JC087iC10p07971.

Maykut, G.A., McPhee, M.G., 1995. Solar heating of the Arctic mixed layer. J. Geophys. Res. 100, 24691–24703. doi:10.1029/95JC02554.

Maykut, G.A., Perovich, D.K., 1987. The role of shortwave radiation in the summer decay of a sea ice cover. J. Geophys. Res. 92, 7032–7044. doi:10.1029/JC092iC07p07032.

McPhee, M.G., 1992. Turbulent Heat Flux in the Upper Ocean Under Sea Ice. J. Geophys. Res. 97, 5365–5379. doi:10.1029/92JC00239.

McPhee, M.G., 2012. Advances in understanding ice-ocean stress during and since AIDJEX. Cold Reg. Sci. Technol. 76-77, 24–36. doi:10.1016/j.coldregions.2011.05.001.

McPhee, M.G., Kikuchi, T., Morison, J.H., Stanton, T.P., 2003. Ocean-to-ice heat flux at the North Pole environmental observatory. Geophys. Res. Lett. 30, 2274. doi:10.1029/2003GL018580.

McPhee, M.G., Kottmeier, C., Morison, J.H., 1999. Ocean Heat Flux in the Central Weddell Sea during Winter. J. Phys. Oceanogr. 29, 1166–1179. doi:10.1175/1520-0485(1999)029<1166:OHFITC>2.0.CO;2.

Meier, W.N., Gallaher, D., Campbell, G.G., 2013. New estimates of Arctic and Antarctic sea ice extent during September 1964 from recovered Nimbus I satellite imagery. The Cryosphere 7, 699–705. doi:10.5194/tc-7-699-2013.

Moreau, S., Vancoppenolle, M., Delille, B., Tison, J.L., Zhou, J., Kotovitch, M., Thomas, D.N., Geilfus, N.X., Goosse, H., 2015. Drivers of inorganic carbon dynamics in first-year sea ice: A model study. J. Geophys. Res. Oceans 120, 471–495. doi:10.1002/2014JC010388.

Morison, J.H., McPhee, M.G., 1998. Lead convection measured with an autonomous underwater vehicle. J. Geophys. Res. 103, 3257–3281. doi:10.1029/97JC02264.

Morison, J.H., McPhee, M.G., Curtin, T.B., Paulson, C.A., 1992. The oceanography of winter leads. J. Geophys. Res. 97, 11199–11218. doi:10.1029/92JC00684.

Msadek, R., Vecchi, G.A., Winton, M., Gudgel, R.G., 2014. Importance of initial conditions in seasonal predictions of Arctic sea ice extent. Geophys. Res. Lett. 41, 5208–5215. doi:10.1002/2014GL060799.

Muench, R.D., Smith, D.C., Paulson, C.A., 1995. Convection beneath freezing leads: New observations compared with numerical model results. J. Geophys. Res. 100, 4681–4692. doi:10.1029/94JC02503.

Nguyen, A.T., Menemenlis, D., Kwok, R., 2009. Improved modeling of the Arctic halocline with a subgrid-scale brine rejection parameterization. J. Geophys. Res. 114, C11014. doi:10.1029/2008JC005121.

Nicolaus, M., Katlein, C., Maslanik, J., Hendricks, S., 2012. Changes in Arctic sea ice result in increasing light transmittance and absorption. Geophys. Res. Lett. 39, L24501. doi:10.1029/2012GL053738.

Nicolaus, M., Petrich, C., Hudson, S.R., Granskog, M.A., 2013. Variability of light transmission through Arctic land-fast sea ice during spring. The Cryosphere 7, 977–986. doi:10.5194/tc-7-977-2013.

Nihashi, S., Ohshima, K.I., 2015. Circumpolar Mapping of Antarctic Coastal Polynyas and Landfast Sea Ice: Relationship and Variability. J. Climate 28, 3650–3670. doi:10.1175/JCLI-D-14-00369.1.

Notz, D., 2012. Challenges in simulating sea ice in Earth System Models. WIREs Clim. Change 3, 509–526. doi:10.1002/wcc.189.

Notz, D., Marotzke, J., 2012. Observations reveal external driver for Arctic sea-ice retreat. Geophys. Res. Lett. 39, L08502. doi:10.1029/2012GL051094.

Ohshima, K.I., Nihashi, S., 2005. A Simplified Ice-Ocean Coupled Model for the Antarctic Ice Melt Season. J. Phys. Oceanogr. 35, 188–201. doi:10.1175/JPO-2675.1.

Overland, J., Francis, J.A., Hall, R., Hanna, E., Kim, S.J., Vihma, T., 2015. The Melting Arctic and Midlatitude Weather Patterns: Are They Connected? J. Climate 28, 7917–7932. doi:10.1175/JCLI-D-14-00822.1.

Overland, J.E., Francis, J.A., Hanna, E., Wang, M., 2012. The recent shift in early summer Arctic atmospheric circulation. Geophys. Res. Lett. 39, L19804. doi:10.1029/2012GL053268.

Paluszkiewicz, T., Romea, R., 1997. A one-dimensional model for the parameterization of deep convection in the ocean. Dyn. Atmos. Oceans 26, 95–130. doi:10.1016/S0377-0265(96)00482-4.

Parkinson, C.L., 2014a. Global Sea Ice Coverage from Satellite Data: Annual Cycle and 35-Yr Trends. J. Climate 27, 9377–9382. doi:10.1175/JCLI-D-14-00605.1.

Parkinson, C.L., 2014b. Spatially mapped reductions in the length of the Arctic sea ice season. Geophys. Res. Lett. 41, 2014GL060434. doi:10.1002/2014GL060434.

Parmentier, F.J.W., Zhang, W., Mi, Y., Zhu, X., van Huissteden, J., Hayes, D.J., Zhuang, Q., Christensen, T.R., McGuire, A.D., 2015. Rising methane emissions from northern wetlands associated with sea ice decline. Geophys. Res. Lett. 42, 7214–7222. doi:10.1002/2015GL065013.

Perovich, D.K., Elder, B., 2002. Estimates of ocean heat flux at SHEBA. Geophys. Res. Lett. 29, 1344. doi:10.1029/2001GL014171.

Perovich, D.K., Polashenski, C., 2012. Albedo evolution of seasonal Arctic sea ice. Geophys. Res. Lett. 39, L08501. doi:10.1029/2012GL051432.

Petty, A.A., Holland, P.R., Feltham, D.L., 2014. Sea ice and the ocean mixed layer over the Antarctic shelf seas. The Cryosphere 8, 761–783. doi:10.5194/tc-8-761-2014.

Polvani, L.M., Smith, K.L., 2013. Can natural variability explain observed Antarctic sea ice trends? New modeling evidence from CMIP5. Geophys. Res. Lett. 40, 3195–3199. doi:10.1002/grl.50578.

Polyakov, I.V., Alexeev, V.A., Ashik, I.M., Bacon, S., Beszczynska-Möller, A., Carmack, E.C., Dmitrenko, I.A., Fortier, L., Gascard, J.C., Hansen, E., Hölemann, J., Ivanov, V.V., Kikuchi, T., Kirillov, S., Lenn, Y.D., McLaughlin, F.A., Piechura, J., Repina, I., Timokhov, L.A., Walczowski, W., Woodgate, R., 2011. Fate of Early 2000s Arctic Warm Water Pulse. Bull. Amer. Meteor. Soc. 92, 561–566. doi:10.1175/2010BAMS2921.1.

Polyakov, I.V., Pnyushkov, A.V., Rember, R., Padman, L., Carmack, E.C., Jackson, J.M., 2013. Winter Convection Transports Atlantic Water Heat to the Surface Layer in the Eastern Arctic Ocean. J. Phys. Oceanogr. 43, 2142–2155. doi:10.1175/JPO-D-12-0169.1.

Polyakov, I.V., Pnyushkov, A.V., Timokhov, L.A., 2012. Warming of the Intermediate Atlantic Water of the Arctic Ocean in the 2000s. J. Climate 25, 8362–8370. doi:10.1175/JCLI-D-12-00266.1.

Polyakov, I.V., Timokhov, L.A., Alexeev, V.A., Bacon, S., Dmitrenko, I.A., Fortier, L., Frolov, I.E., Gascard, J.C., Hansen, E., Ivanov, V.V., Laxon, S., Mauritzen, C., Perovich, D., Shimada, K., Simmons, H.L., Sokolov, V.T., Steele, M., Toole, J., 2010. Arctic Ocean Warming Contributes to Reduced Polar Ice Cap. J. Phys. Oceanogr. 40, 2743–2756. doi:10.1175/2010JPO4339.1.

Prather, M.J., 1986. Numerical advection by conservation of second-order moments. J. Geophys. Res. 91, 6671–6681. doi:10.1029/JD091iD06p06671.

Pringle, D.J., Eicken, H., Trodahl, H.J., Backstrom, L.G.E., 2007. Thermal conductivity of landfast Antarctic and Arctic sea ice. J. Geophys. Res. 112, C04017. doi:10.1029/2006JC003641.

Rampal, P., Weiss, J., Dubois, C., Campin, J.M., 2011. IPCC climate models do not capture Arctic sea ice drift acceleration: Consequences in terms of projected sea ice thinning and decline. J. Geophys. Res. 116, C00D07. doi:10.1029/2011JC007110.

Ren, L., Speer, K., Chassignet, E.P., 2011. The mixed layer salinity budget and sea ice in the Southern Ocean. J. Geophys. Res. 116, C08031. doi:10.1029/2010JC006634.

Richter-Menge, J.A., Farrell, S.L., 2013. Arctic sea ice conditions in spring 2009-2013 prior to melt. Geophys. Res. Lett. 40, 2013GL058011. doi:10.1002/2013GL058011.

Rintoul, S., et al., 2014. Seeing below the ice: A strategy for observing the ocean beneath Antarctic sea ice and ice shelves. Technical Report. Southern Ocean Observing System.

Rodgers, K.B., Aumont, O., Mikaloff Fletcher, S.E., Plancherel, Y., Bopp, L., de Boyer Montégut, C., Iudicone, D., Keeling, R.F., Madec, G., Wanninkhof, R., 2014. Strong sensitivity of Southern Ocean carbon uptake and nutrient cycling to wind stirring. Biogeosciences 11, 4077–4098. doi:10.5194/bg-11-4077-2014.

Rogers, T.S., Walsh, J.E., Rupp, T.S., Brigham, L.W., Sfraga, M., 2013. Future Arctic marine access: analysis and evaluation of observations, models, and projections of sea ice. The Cryosphere 7, 321–332. doi:10.5194/tc-7-321-2013.

Roquet, F., Charrassin, J.B., Marchand, S., Boehme, L., Fedak, M., Reverdin, G., Guinet, C., 2011. Delayed-Mode Calibration of Hydrographic Data Obtained from Animal-Borne Satellite Relay Data Loggers. J. Atmos. Oceanic Technol. 28, 787–801. doi:10.1175/2010JTECHO801.1.

Roquet, F., Wunsch, C., Forget, G., Heimbach, P., Guinet, C., Reverdin, G., Charrassin, J.B., Bailleul, F., Costa, D.P., Huckstadt, L.A., Goetz, K.T., Kovacs, K.M., Lydersen, C., Biuw, M., Nøst, O.A., Bornemann, H., Ploetz, J., Bester, M.N., McIntyre, T., Muelbert, M.C., Hindell, M.A., McMahon, C.R., Williams, G., Harcourt, R., Field, I.C., Chafik, L., Nicholls, K.W., Boehme, L., Fedak, M.A., 2013. Estimates of the Southern Ocean general circulation improved by animal-borne instruments. Geophys. Res. Lett. 40, 2013GL058304. doi:10.1002/2013GL058304.

Rothrock, D.A., Zhang, J., 2005. Arctic Ocean sea ice volume: What explains its recent depletion? J. Geophys. Res. 110, C01002. doi:10.1029/2004JC002282.

Roullet, G., Madec, G., 2000. Salt conservation, free surface, and varying levels: A new formulation for ocean general circulation models. J. Geophys. Res. 105, 23927–23942. doi:10.1029/2000JC900089.

Rousset, C., Vancoppenolle, M., Madec, G., Fichefet, T., Flavoni, S., Barthélemy, A., Benshila, R., Chanut, J., Levy, C., Masson, S., Vivier, F., 2015. The Louvain-La-Neuve sea ice model LIM3.6: global and regional capabilities. Geosci. Model Dev. 8, 2991–3005. doi:10.5194/gmd-8-2991-2015.

Sallée, J.B., Speer, K.G., Rintoul, S.R., 2010. Zonally asymmetric response of the Southern Ocean mixed-layer depth to the Southern Annular Mode. Nat. Geosci. 3, 273–279. doi:10.1038/ngeo812.

Schmidt, G.A., Bitz, C.M., Mikolajewicz, U., Tremblay, L.B., 2004. Ice-ocean boundary conditions for coupled models. Ocean Modell. 7, 59–74. doi:10.1016/S1463-5003(03)00030-1.

Schmidtko, S., Johnson, G.C., Lyman, J.M., 2013. MIMOC: A global monthly isopycnal upper-ocean climatology with mixed layers. J. Geophys. Res. Oceans 118, 1658–1672. doi:10.1002/jgrc.20122.

Schweiger, A., Lindsay, R., Zhang, J., Steele, M., Stern, H., Kwok, R., 2011. Uncertainty in modeled Arctic sea ice volume. J. Geophys. Res. 116, C00D06. doi:10.1029/2011JC007084.

Screen, J.A., Simmonds, I., Deser, C., Tomas, R., 2012. The Atmospheric Response to Three Decades of Observed Arctic Sea Ice Loss. J. Climate 26, 1230–1248. doi:10.1175/JCLI-D-12-00063.1.

Sedlacek, J., Knutti, R., Martius, O., Beyerle, U., 2011. Impact of a Reduced Arctic Sea Ice Cover on Ocean and Atmospheric Properties. J. Climate 25, 307–319. doi:10.1175/2011JCLI3904.1.

Shaw, W.J., Stanton, T.P., 2014. Vertical diffusivity of the Western Arctic Ocean halocline. J. Geophys. Res. Oceans 119, 5017–5038. doi:10.1002/2013JC009598.

Shu, Q., Song, Z., Qiao, F., 2015. Assessment of sea ice simulations in the CMIP5 models. The Cryosphere 9, 399–409. doi:10.5194/tc-9-399-2015.

Sirevaag, A., McPhee, M.G., Morison, J.H., Shaw, W.J., Stanton, T.P., 2010. Wintertime mixed layer measurements at Maud Rise, Weddell Sea. J. Geophys. Res. 115, C02009. doi:10.1029/2008JC005141.

Skyllingstad, E.D., Denbo, D.W., 2001. Turbulence beneath sea ice and leads: A coupled sea ice/large-eddy simulation study. J. Geophys. Res. 106, 2477–2497. doi:10.1029/1999JC000091.

Skyllingstad, E.D., Paulson, C.A., Pegau, W.S., 2005. Simulation of turbulent exchange processes in summertime leads. J. Geophys. Res. 110, C05021. doi:10.1029/2004JC002502.

Smith, D.C., Morison, J.H., 1993. A numerical study of haline convection beneath leads in sea ice. J. Geophys. Res. 98, 10069–10083. doi:10.1029/93JC00137.

Smith, D.C., Morison, J.H., 1998. Nonhydrostatic haline convection under leads in sea ice. J. Geophys. Res. 103, 3233–3247. doi:10.1029/97JC02262.

Smith, W.O., Dinniman, M.S., Hofmann, E.E., Klinck, J.M., 2014. The effects of changing winds and temperatures on the oceanography of the Ross Sea in the 21st century. Geophys. Res. Lett. 41, 1624–1631. doi:10.1002/2014GL059311.

Spreen, G., Kwok, R., Menemenlis, D., 2011. Trends in Arctic sea ice drift and role of wind forcing: 1992-2009. Geophys. Res. Lett. 38, L19501. doi:10.1029/2011GL048970.

Stanton, T.P., Shaw, W.J., Hutchings, J.K., 2012. Observational study of relationships between incoming radiation, open water fraction, and ocean-to-ice heat flux in the Transpolar Drift: 2002-2010. J. Geophys. Res. 117, n/a–n/a. doi:10.1029/2011JC007871.

Steele, M., 1992. Sea ice melting and floe geometry in a simple ice-ocean model. J. Geophys. Res. 97, 17729–17738. doi:10.1029/92JC01755.

Steele, M., Ermold, W., Zhang, J., 2011. Modeling the formation and fate of the near-surface temperature maximum in the Canadian Basin of the Arctic Ocean. J. Geophys. Res. 116, C11015. doi:10.1029/2010JC006803.

Steele, M., Morley, R., Ermold, W., 2001. PHC: A Global Ocean Hydrography with a High-Quality Arctic Ocean. J. Climate 14, 2079–2087. doi:10.1175/1520-0442(2001)014<2079:PAGOHW>2.0.CO;2.

Stroeve, J., Barrett, A., Serreze, M., Schweiger, A., 2014. Using records from submarine, aircraft and satellites to evaluate climate model simulations of Arctic sea ice thickness. The Cryosphere 8, 1839–1854. doi:10.5194/tc-8-1839-2014.

Stroeve, J.C., Kattsov, V., Barrett, A., Serreze, M., Pavlova, T., Holland, M., Meier, W.N., 2012. Trends in Arctic sea ice extent from CMIP5, CMIP3 and observations. Geophys. Res. Lett. 39, L16502. doi:10.1029/2012GL052676.

Stössel, A., Notz, D., Haumann, F.A., Haak, H., Jungclaus, J., Mikolajewicz, U., 2015. Controlling high-latitude Southern Ocean convection in climate models. Ocean Modell. 86, 58–75. doi:10.1016/j.ocemod.2014.11.008.

Stössel, A., Yang, K., Kim, S.J., 2002. On the Role of Sea Ice and Convection in a Global Ocean Model. J. Phys. Oceanogr. 32, 1194–1208. doi:10.1175/1520-0485(2002)032<1194:OTROSI>2.0.CO;2.

Swart, N.C., Fyfe, J.C., 2013. The influence of recent Antarctic ice sheet retreat on simulated sea ice area trends. Geophys. Res. Lett. 40, 4328–4332. doi:10.1002/grl.50820.

Swart, N.C., Fyfe, J.C., Hawkins, E., Kay, J.E., Jahn, A., 2015. Influence of internal variability on Arctic sea-ice trends. Nature Clim. Change 5, 86–89. doi:10.1038/nclimate2483.

Thomson, J., Rogers, W.E., 2014. Swell and sea in the emerging Arctic Ocean. Geophys. Res. Lett. 41, 3136–3140. doi:10.1002/2014GL059983.

Thorndike, A.S., Rothrock, D.A., Maykut, G.A., Colony, R., 1975. The Thickness Distribution of Sea Ice. J. Geophys. Res. 80, 4501–4513. doi:10.1029/JC080i033p04501.

Timmermans, M.L., 2015. The impact of stored solar heat on Arctic sea ice growth. Geophys. Res. Lett. 42, 6399–6406. doi:10.1002/2015GL064541.

Toole, J.M., Timmermans, M.L., Perovich, D.K., Krishfield, R.A., Proshutinsky, A., Richter-Menge, J.A., 2010. Influences of the ocean surface mixed layer and thermohaline stratification on Arctic Sea ice in the central Canada Basin. J. Geophys. Res. 115, C10018. doi:10.1029/2009JC005660.

Trenberth, K.E., Large, W.G., Olson, J.G., 1989. Global Ocean Wind Stress, climatology and monthly, by Trenberth et al. Digital media. National Center for Atmospheric Research. Boulder, Colorado, USA.

Tsamados, M., Feltham, D.L., Schroeder, D., Flocco, D., Farrell, S.L., Kurtz, N., Laxon, S.W., Bacon, S., 2014. Impact of Variable Atmospheric and Oceanic Form Drag on Simulations of Arctic Sea Ice. J. Phys. Oceanogr. 44, 1329–1353. doi:10.1175/JPO-D-13-0215.1.

Tsamados, M., Feltham, D.L., Wilchinsky, A.V., 2013. Impact of a new anisotropic rheology on simulations of Arctic sea ice. J. Geophys. Res. Oceans 118, 91–107. doi:10.1029/2012JC007990.

Turner, J., Bracegirdle, T.J., Phillips, T., Marshall, G.J., Hosking, J.S., 2012. An Initial Assessment of Antarctic Sea Ice Extent in the CMIP5 Models. J. Climate 26, 1473–1484. doi:10.1175/JCLI-D-12-00068.1.

Vancoppenolle, M., Fichefet, T., Goosse, H., 2009a. Simulating the mass balance and salinity of Arctic and Antarctic sea ice. 2. Importance of sea ice salinity variations. Ocean Modell. 27, 54–69. doi:10.1016/j.ocemod.2008.11.003.

Vancoppenolle, M., Fichefet, T., Goosse, H., Bouillon, S., Madec, G., Morales Maqueda, M.A., 2009b. Simulating the mass balance and salinity of Arctic and Antarctic sea ice. 1. Model description and validation. Ocean Modell. 27, 33–53. doi:10.1016/j.ocemod.2008.10.005.

Vancoppenolle, M., Meiners, K.M., Michel, C., Bopp, L., Brabant, F., Carnat, G., Delille, B., Lannuzel, D., Madec, G., Moreau, S., Tison, J.L., van der Merwe, P., 2013. Role of sea ice in global biogeochemical cycles: emerging views and challenges. Quaternary Sci. Rev. 79, 207–230. doi:10.1016/j.quascirev.2013.04.011.

Vancoppenolle, M., Timmermann, R., Ackley, S.F., Fichefet, T., Goosse, H., Heil, P., Leonard, K.C., Lieser, J., Nicolaus, M., Papakyriakou, T., Tison, J.L., 2011. Assessment of radiation forcing data sets for large-scale sea ice models in the Southern Ocean. Deep-Sea Res. Pt II 58, 1237–1249. doi:10.1016/j.dsr2.2010.10.039.

Venables, H.J., Meredith, M.P., 2014. Feedbacks between ice cover, ocean stratification, and heat content in Ryder Bay, western Antarctic Peninsula. J. Geophys. Res. Oceans 119, 5323–5336. doi:10.1002/2013JC009669.

Vihma, T., Tisler, P., Uotila, P., 2012. Atmospheric forcing on the drift of Arctic sea ice in 1989-2009. Geophys. Res. Lett. 39, L02501. doi:10.1029/2011GL050118.

Wadhams, P., Hughes, N., Rodrigues, J., 2011. Arctic sea ice thickness characteristics in winter 2004 and 2007 from submarine sonar transects. J. Geophys. Res. 116, C00E02. doi:10.1029/2011JC006982.

Wang, L., Derksen, C., Brown, R., Markus, T., 2013. Recent changes in pan-Arctic melt onset from satellite passive microwave measurements. Geophys. Res. Lett. 40, 522–528. doi:10.1002/grl.50098.

Wang, X.L., Feng, Y., Swail, V.R., Cox, A., 2015. Historical Changes in the Beaufort-Chukchi-Bering Seas Surface Winds and Waves, 1971-2013. J. Climate 28, 7457–7469. doi:10.1175/JCLI-D-15-0190.1.

Wilchinsky, A.V., Heorton, H.D.B.S., Feltham, D.L., Holland, P.R., 2015. Study of the Impact of Ice Formation in Leads upon the Sea Ice Pack Mass Balance Using a New Frazil and Grease Ice Parameterization. J. Phys. Oceanogr. 45, 2025–2047. doi:10.1175/JPO-D-14-0184.1.

Winton, M., 1999. Polar Water Column Stability. J. Phys. Oceanogr. 29, 1368–1371. doi:10.1175/1520-0485(1999)029<1368:PWCS>2.0.CO;2.

WMO, 1970. WMO sea-ice nomenclature. Technical Report 259. World Meteorological Organization. Geneva.

Wong, A.P.S., Riser, S.C., 2011. Profiling Float Observations of the Upper Ocean under Sea Ice off the Wilkes Land Coast of Antarctica. J. Phys. Oceanogr. 41, 1102–1115. doi:10.1175/2011JPO4516.1.

Worby, A.P., Geiger, C.A., Paget, M.J., Van Woert, M.L., Ackley, S.F., DeLiberty, T.L., 2008. Thickness distribution of Antarctic sea ice. J. Geophys. Res. 113, C05S92. doi:10.1029/2007JC004254.

Zhang, J., 2007. Increasing Antarctic Sea Ice under Warming Atmospheric and Oceanic Conditions. J. Climate 20, 2515–2529. doi:10.1175/JCLI4136.1.

Zhang, J., Lindsay, R., Schweiger, A., Rigor, I., 2012. Recent changes in the dynamic properties of declining Arctic sea ice: A model study. Geophys. Res. Lett. 39, L20503. doi:10.1029/2012GL053545.

Zhang, J., Lindsay, R., Schweiger, A., Steele, M., 2013. The impact of an intense summer cyclone on 2012 Arctic sea ice retreat. Geophys. Res. Lett. 40, 720–726. doi:10.1002/grl.50190.

Zhang, J., Rothrock, D.A., 2003. Modeling Global Sea Ice with a Thickness and Enthalpy Distribution Model in Generalized Curvilinear Coordinates. Mon. Wea. Rev. 131, 845–861. doi:10.1175/1520-0493(2003)131<0845:MGSIWA>2.0.CO;2.

Zhang, J., Schweiger, A., Steele, M., Stern, H., 2015. Sea ice floe size distribution in the marginal ice zone: Theory and numerical experiments. J. Geophys. Res. Oceans 120, 3484–3498. doi:dx.doi.org/10.1002/2015JC010770.

Zhang, J., Steele, M., 2007. Effect of vertical mixing on the Atlantic Water layer circulation in the Arctic Ocean. J. Geophys. Res. 112, C04S04. doi:10.1029/2006JC003732.

Zunz, V., Goosse, H., Massonnet, F., 2013. How does internal variability influence the ability of CMIP5 models to reproduce the recent trend in Southern Ocean sea ice extent? The Cryosphere 7, 451–468. doi:10.5194/tc-7-451-2013.

Zygmuntowska, M., Rampal, P., Ivanova, N., Smedsrud, L.H., 2014. Uncertainties in Arctic sea ice thickness and volume: new estimates and implications for trends. The Cryosphere 8, 705–720. doi:10.5194/tc-8-705-2014.